The Structure of the Ionic Liquid / Electrode Interface and its Possible Influence on Electrochemical Materials Synthesis: an *in situ* STM and AFM Study

Habilitationsschrift

zur Erlangung der *venia legendi*
für das Fachgebiet
Physikalische Chemie

vorgelegt von
Dr. rer. nat. Natalia Borisenko

aus Sluzk/Weißrussland

Fakultät für Natur- und Materialwissenschaften
der Technische Universität Clausthal
2022

Abstract

Ionic liquids (ILs) have become one of the most popular material classes over the past twenty years. They have been considered as alternative materials to molecular solvents and molten salts in various applications (e.g. batteries, capacitors, lubricants, solvents for electrodeposition purposes). A detailed understanding of the IL/solid interfacial nanostructure and of the spatial distribution of the electroactive species at the interface is important for the development of various technical processes using ILs.

In the present work the structure of the electrified IL/solid interface was investigated using *in situ* scanning tunnelling microscopy (STM) and atomic force microscopy (AFM). Various ILs, namely $[Py_{1,4}]$TFSA, $[Py_{1,4}]$FAP, $[Py_{1,4}]$FSA, $[Py_{1,4}]$TfO, [EMIm]TFSA, [OMIm]TFSA, [EMIm]FAP, [EMIm]TfO and [HMIm]FAP were applied for this study. *In situ* AFM reveals that multiple interfacial layers are present at the IL/electrode interface. Furthermore, the applied potential determines whether cations or anions are preferably adsorbed to the substrate with stronger near surface layering detected at higher positive or negative surface potentials. Both the cation and the anion of the IL have a strong influence on the structure and composition of the interface. *In situ* STM shows that the appearance of the Au(111) and H-terminated p-Si(111) surfaces is different in various ILs, due to specific ion/surface and ion/ion interactions, which are dependent on the type of the functional groups (pyrrolidinium or imidazolium ring and the length of the alkyl chains), resulting in a different interfacial structure for various cations. With the same anion, the Au(111) surface undergoes the $(22 \times \sqrt{3})$ reconstruction with $[Py_{1,4}]^+$ during cathodic polarization, but with $[EMIm]^+$, $[HMIm]^+$ and $[OMIm]^+$ the herringbone superstructure has not been obtained. Furthermore, different [OMIm]TFSA superstructures with the lateral size between 1.2 and 1.7 nm are probed with *in situ* STM on highly ordered pyrolytic graphite (HOPG) at high negative electrode potentials, as a result of several cation and/or anion layers probed at the same time by the STM tip. AFM measurements show that the imidazolium cation is adsorbed at the H-Si(111)/[EMIm]TFSA interface leading to an ordered clustered facet structure of ~3.8 nm in size. In comparison, the Si(111)/$[Py_{1,4}]$TFSA interface appears the same as the native surface under argon.

The interfacial structure is sensitive to metal and semiconductor salts dissolved in the IL. In general the ion layering at the IL/solid interface is markedly different in the presence of dissolved solutes than for the pure IL systems, as the presence of salt ions alters both the IL-surface and IL-IL interactions at the interface. For instance, AFM measurements reveal that interfacial layering is markedly weaker in the presence of LiCl and $SiCl_4$ in $[Py_{1,4}]$FAP. The presence of Li^+ and Si(IV) affects interactions between $[Py_{1,4}]^+$ and the gold surface hindering the $(22 \times \sqrt{3})$ Au(111) reconstruction.

Marked changes in the IL/Si(111) interfacial structure are obtained on addition of LiTFSA in $[Py_{1,4}]$TFSA and [EMIm]TFSA. The concentration of the solute has also a significant effect on the structure of the IL/electrode interface. Thus, considerable changes are obtained on addition of high concentrations of NaFSA and LiTFSA in $[Py_{1,4}]$FSA and $[Py_{1,4}]$TFSA, respectively. For the [EMIm]TfO/Au(111) interface the structure of the innermost layer also depends on the amount of added water. A transition from a multilayered structure to a classical double layer structure occurs at -1.0 V vs. Pt on changing the water concentration from 30 to 50 vol%. The formation of a double layer structure at the IL/Au(111) interface is also obtained on increasing the concentration of $SiCl_4$ in $[Py_{1,4}]$FAP. *In situ* AFM force-separation measurements confirm that the dissolved solute is present within the innermost (Stern) layer. The altered interfacial structures represent the best compromise between the IL ion and solute surface affinities, packing constraints, and charge localisations. Thus, the IL EDL is highly complex both in the pure ILs and in the presence of solutes and often leads to an unpredictable electrochemical behaviour. This in turn should affect the reactions that occur at the IL/electrode interface (e.g. metal deposition). Thus, in $[Py_{1,4}]$TFSA, TaF_5 can be reduced to elemental Ta, while in $[Py_{1,4}]$FAP the electroreduction processes are practically inhibited. The difference for Si deposition from $SiCl_4$ in $[Py_{1,4}]$TFSA and $[Py_{1,4}]$FAP is roughly 1 V. The crystal sizes of the electrodeposited Ga varies upon changing the ILs. The deposit made from $[Py_{1,4}]$TFSA consists of spherical structures of 60-260 nm in diameter, while the crystal sizes of a Ga deposit obtained from $[Py_{1,4}]$TfO are between 15 and 110 nm. In the case of $[Py_{1,4}]$FSA a nanocrystalline Ga deposit with a crystal size of less than 50 nm is obtained. Furthermore, GaSb obtained in [EMIm]TFSA and $[Py_{1,4}]$TFSA exhibits a band gap of about 1.2 eV and 0.9 eV, respectively.

The present work shows that the electrodeposition of metals and semiconductors in ILs is complicated. On the one hand, the (chemical) structure of the IL has an influence on the EDL structure of the Au(111)/IL interface. On the other hand, the addition of precursors, which are required for the deposition processes, can also affect the structure of the electrode/IL interface. Furthermore, the nanostructure of interfacial layers can vary if the concentration of the precursor is increased, which might facilitate the deposition processes. Such interfacial effects have to be considered for all applications that involve reactions at the IL/solid interface.

Content

1 Motivation

Ionic liquids (ILs) – organic salts with melting points usually less than 100 °C – have become one of the most popular material classes over the past twenty years. Many of the most interesting systems are liquid at room temperature and have melting points even below 0 °C. ILs consist entirely of charged species (bulky organic cation and an organic or inorganic anion) and behave very differently to common molecular liquids. ILs are currently the focus of intense research activities due to their remarkable physical properties, which often include wide electrochemical windows, good thermal stability and high conductivity. ILs generally exhibit good solvent properties and often facilitate and influence chemical reactions without being consumed or altered in the process. They are usually non-volatile, and hence, can be used in high-vacuum systems. Since ILs are, in most cases, non-flammable with low toxicity, they are often classified as “green solvents”. ILs can -in principle- replace volatile organic solutions in organic synthesis, as many ILs remain thermally stable at temperatures higher than conventional organic solvents. Furthermore, ILs are liquid over a wider temperature range than molecular solvents. An interesting feature is that all of these properties can be modified (tuned) by varying the chemical structure of cations and anions. Therefore, ILs are often considered as tuneable “designer solvents”. A fascinating aspect of ILs is their variety as there is a wide range of possible cation and anion combinations resulting in almost infinite number of possible ILs. Currently, about 800 ionic liquids exist and around 10^{18} different liquids and mixtures have been predicted. The growing academic and industrial interest in ILs is represented by a yearly increase in the number of publications with the key word “ionic liquid” (fig. 1): starting from a few in 1996 to almost 9000 in 2020.

The motivation of the present thesis was to investigate the structure of the IL/solid interface and its role in electrochemical processes. IL applications encompass many areas including analytics, catalysis, chemical synthesis, separation technologies, electrochemistry, capacitors, batteries, fuel cells, solar cells, and lubrication. Many of these applications involve reactions at the IL/solid interface and a detailed understanding of the structure of this interface is important for a wider integration of ILs. Ionic liquids exhibit an interesting interfacial chemistry (Chapter 4). ILs have been shown to form a layered structure at the electrode/electrolyte interface, which depending on the substrate can extend up to 10 nm from the surface into the solution. The adsorption of ILs is stronger than that of organic and aqueous solvents and the strength of the interactions between the innermost layer and the substrate is

dependent on the cation/anion type. Furthermore, the addition of salts can alter the structure of the IL/solid interface that, in turn, influences the electrochemical processes. While the surface chemistry of aqueous systems has been a subject of extensive studies, the investigation of the IL/solid interface is much less advanced. Therefore, studies of the IL/solid interface both in the pure ILs and in the presence of solutes can be helpful for understanding of the IL's complicated surface chemistry.

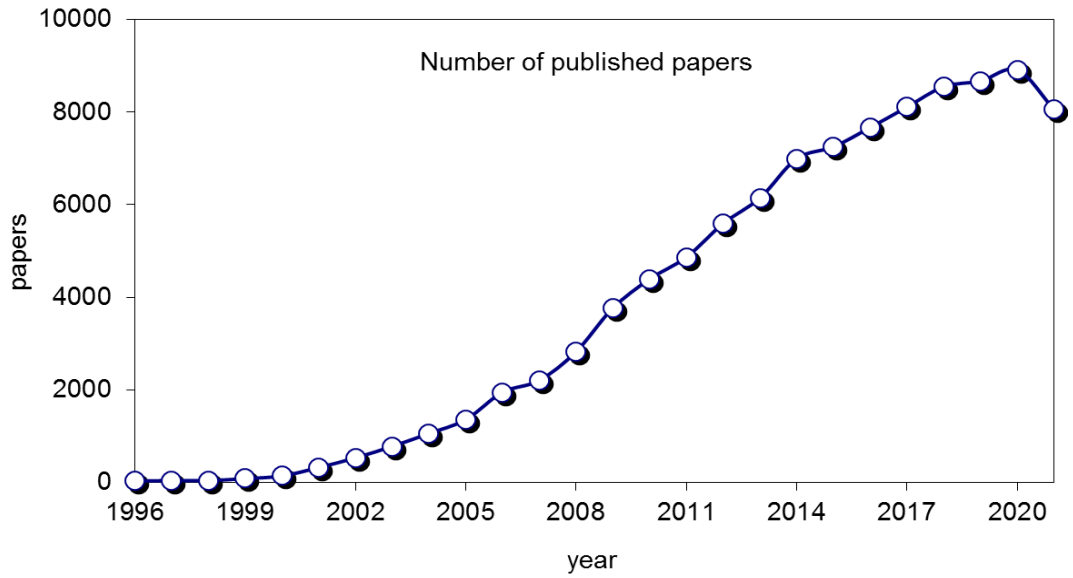

Fig. 1.1 *The rise in publications concerning ionic liquid between 1996 and 2021 (determined using "Web of Science").*

In the present thesis *in situ* scanning tunneling microscopy (STM) and atomic force microscopy (AFM) were employed to elucidate the interfacial nanostructure of ILs near Au(111), H-terminated p-Si(111) and highly ordered pyrolytic graphite (HOPG) electrode surfaces both in the pure ILs and in the presence of solutes. It is shown that the IL/solid interface is highly complex (Chapter 5) and sensitive to metal and semiconductor salts dissolved in the IL (Chapter 6). Thus, even a very low concentration of the dissolved salt can alter the herringbone reconstruction of the gold surface. On increasing the concentration of dissolved salt, instead of a multi-layered interfacial structure typical for IL, rather a classical double layer structure is observed prior to electrodeposition, which in turn can facilitate the deposition process (Chapter 7). Furthermore, the structure and the composition of the interfacial layer can be tuned by both varying the surface potential and the IL ion structure. These results open new possibilities for the design of IL structures at metal electrode interfaces, which will impact a diverse range of electrochemical applications, including electrodeposition, batteries, capacitors, and dye-sensitized solar cells.

2 Introduction in Ionic Liquids

The content of this section, partly published in the PhD thesis of the author [1], was supplemented and adopted for the present thesis.

Ionic Liquids (ILs) are materials that are solely composed of ions with melting points usually below 100-150 °C [2-4]. There are many synonyms used for ILs in the literature. ILs are also known as molten salts, fused salts, neoteric solvents, non-aqueous ILs, room temperature molten salt, liquid organic salt, designer solvents, etc., from which the term “molten salts” is the most common one. In a wider sense, the term “ionic liquid” includes all molten salts with melting points from -50 °C (for modern synthetic ionic liquids) to more than 1000 °C (for classical inorganic halides). Molten salts exhibit high ionic conductivities and good chemical, electrochemical and thermal stabilities. As many chemical substances can be dissolved in them, molten salts are widely used as important industrial electrolytes for the electrodeposition of metals and semiconductors [5]. Although the term “molten salt” has been broadly applied for ionic liquids, the practical difference is significant. In general, the classical high temperature molten salts (e.g. NaCl, KCl, etc.) are systems with melting points above 200 °C, while ILs are usually liquid around room temperature. To differentiate ILs from classically well-known molten salts the boiling point of water was selected as a point of reference. Although there is no agreement upon definition, currently the “official” term “ionic liquid” is used for molten salts, which have melting points or glass-transition temperatures below 100 °C [6]. In particular, ILs, which are liquids at or around room temperature, are often called room temperature ionic liquids (RTILs). Aqueous solutions of salts (e.g. NaCl aqueous solution) cannot be classified as ionic liquids as they are not composed entirely of ions.

ILs can be composed of a large number of cations and anions. Most common ILs are composed of large unsymmetrically substituted and weakly coordinated nitrogen or phosphorus containing cations (e.g. pyrrolidinium, pyrridinium, imidazolium, thiazolium, etc.) and organic or inorganic anions (halides (Cl^-, Br^-), hexafluorophosphate $(PF_6)^-$, bis(trifluoromethylsulfonyl)amide ($TFSA^-$), etc.). The simplest ionic liquids consist of a single cation and a single anion, whereas more complex systems are formed by combining of cations and/or anions, or complex anions, obtained in equilibrium processes (some common examples of ILs are presented in fig. 2.1).

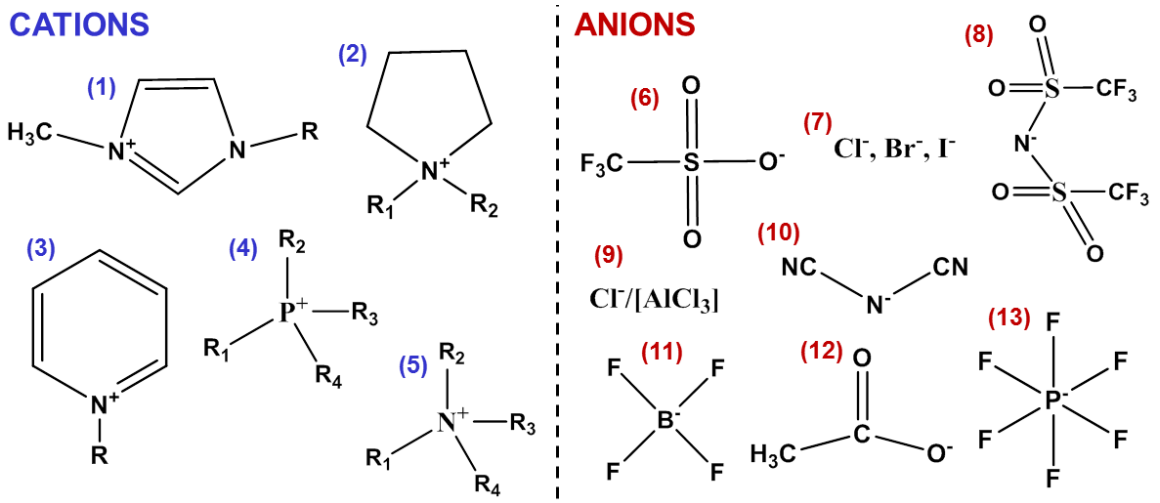

Fig. 2.1 *Examples of cations and anions, which are used in the formation of ionic liquids (R_1-R_4 are alkyl groups). Cations: (1) 1-alkyl-3-methylimidazolium, (2) 1,1-dialkylpyrrolidinium, (3) 1-alkylpyridinium, (4) tetraalkylphosphonium, (5) tetraalkylammonium. Anions: (6) triflate, (7) halide, (8) bis(trifluoromethylsulfonyl)amide, (9) chloroaluminate, (10) dicyanamide, (11) tetrafluoroborate, (12) acetate, (13) hexa-fluorophosphate.*

The physical, chemical and biological properties of ILs are dependent on cation and anion structure and composition, therefore a liquid with adjusted properties can be obtained by varying the type of cation and/or anion.

2.1 Brief History

Ionic liquids have been known for more than a century. In 1914, Walden described the physical properties of a new organic salt, ethylammonium nitrate, ($[C_2H_5NH_3]NO_3$, melting point of 12 °C), synthesized by the reaction of ethylamine with concentrated nitric acid [7]. The obtained material was described as “water-free salt, which melts at low temperatures (up to 100 °C)”. Furthermore, it was found that the physicochemical properties of this organic salt correspond to the properties of inorganic molten salts, which melt at much higher temperatures (between 300 and 600 °C). Moreover, it was suggested that the properties of the salt are dependent on the “nature” of the cation and anion [7]. This salt is commonly regarded as a first RTIL. However, ethanolammonium nitrate with a melting point of 52-55 °C was reported by Gabriel and Weiner in 1888 [8]. Therefore, the discovery date of the first IL and the names of the discoverers might be disputed [4, 9]. Nevertheless, Walden’s discovery did not prompt the great interest at that time and the majority of work on molten salts involved their use as high temperature media for electrochemical and other studies. In 1934, organic salts like e.g. 1-ethylpyridinium chloride and 1-benzylpyridinium chloride were mixed with cellulose at temperatures above 100 °C [10]. In 1948, Hurley and Wier developed

a new room temperature molten salt for applications in aluminium electroplating by mixing and heating alkylpyridinium halides with aluminium chloride [11-13]. The liquid, however, was extremely hygroscopic and the high costs of inert gas systems made this discovery almost forgotten for about 25 years. In the 1960s, Yoke et al. [14] reported that mixtures of alkylammonium chlorides with copper(I) chloride are liquids at room temperature.

In the 1970s and 1980s, the groups of Osteryoung [15, 16] and Hussey [17-20] performed systematic studies on $AlCl_3$ based ILs with 1-butylpyridinium chloride (BPCl) and 1-ethyl-3-methylimidazolium chloride ([EMIm]Cl). Still today the $AlCl_3$ based systems belong to the best understood ones [21]. The Lewis acidity of these liquids can be adjusted by variation of the relative amounts of organic salt and $AlCl_3$ as the molar fraction of the various known chloroaluminate complexes depends on the molar ratio of $AlCl_3$ in the mixture [22]. With a molar excess of $AlCl_3$ they are Lewis acidic and with an excess of organic salt they are Lewis basic. Neutral systems contain a 50/50 mol-% mixture of both the organic salt and $AlCl_3$. In Lewis basic systems only chloride and tetrachloroaluminate are present, whereas in the Lewis acid liquids polynuclear chloroaluminate complexes exist. However, as small variations in the solvent composition (for example, during metal deposition or dissolution) may shift the system towards basic or acidic compositions, the neutral systems have to be buffered by NaCl or $CaCl_2$ [23]. Subsequently, various halometallate ionic liquids based on organic salt (e.g. [BPy]Cl, [EMIm]Cl, [BMIm]Cl, [EMIm]Br, etc.) and metal halide (e.g. $AlCl_3$, $AlBr_3$, $GaCl_3$, $InCl_3$, $ZnCl_2$, etc.) were synthesized. The halometallate room temperature ionic liquids are considered as a first generation of ionic liquids. Due to variable and tuneable acidity the chlorometallate room temperature ionic liquids are well suited to electrochemical (e.g. electrodeposition) applications, transition metal coordination chemistry and in applications as Lewis acid catalysts in organic synthesis. However, the main disadvantage of these salts is their extreme deliquescence. Any trace of moisture decomposes these ILs. This is a major drawback for industrial applications, as these liquids have to be prepared and stored in inert gas atmosphere. Furthermore, such electrolytes require considerable safety issues as they are in part extremely aggressive. Therefore, the discovery of water- and air- stable systems was a major breakthrough in the field of ILs.

In 1992, Wilkes and Zaworotko reported the synthesis of the first air and water stable ionic liquids with the 1-ethyl-3-methylimidazolium cation and either tetrafluoroborate ($[BF_4]^-$), or hexafluorophosphate ($[PF_6]^-$) as anion [24]. 1-butyl-3-methylimidazolium

hexafluorophosphate ([BMIm]PF_6) was synthesized in 1996 [25]. These systems can be regarded to the second generation of ionic liquids. The employed organic cations are weak acids, whereas the anions are weak bases; therefore, the liquids are nearly Lewis neutral. The main disadvantage is that $[BF_4]^-$ and $[PF_6]^-$ react exothermically with strong Lewis acids; for example, if $AlCl_3$ is dissolved in the $[PF_6]^-$ containing liquid, fluoro-chloro-aluminates are formed. In principle, the liquids are water insensitive and could be prepared and handled outside of an inert atmosphere. However, they still need to be handled in dry atmosphere, as in the presence of moisture their physicochemical properties slightly change due to a slow hydrolysis of $[BF_4]^-$ and $[PF_6]^-$ liberating HF. Therefore, systems with more hydrophobic anions, such as trifluoromethanesulfonate (triflate, $[TfO]^-$), bis(trifluoromethylsulfonyl)amide ($[TFSA]^-$) or tris(trifluoromethylsulfonyl)methanide were developed [26, 27]. These RTILs can be regarded as the third generation of ionic liquids. They are water insensitive and can be well dried to water contents below 1 ppm under vacuum at elevated temperatures. Large electrochemical windows (up to 6 V), good thermal stability and ionic conductivity, good solvent property and non-volatility make this class of ILs quite interesting for fundamental science, followed by an exponential growth of interest in ionic liquids and an increasing number of publications (fig. 1.1).

Over the years, the chemical variety of ILs has grown, as new classes of cations and anions were developed. Recently, ILs have been further divided into several types, (e.g. RTILs, task-specific ILs (TSILs), polyionic liquids (PILs), etc.). Detailed information on synthesis, physicochemical properties and applications of ILs in polymerization, catalysis, organic and inorganic synthesis, separation, extraction and electrochemistry can be found in many review articles and books [2, 6, 21, 28-36].

2.2 Some Key Properties

Ionic liquids possess a set of brilliant properties, which make them quite attractive for various applications (e.g. chemical synthesis, separation technology, catalysis, batteries, etc.). ILs are good solvents for a variety of both organic and inorganic materials, they are immiscible with a variety of organic solvents, in part immiscible with water, they are non-volatile (in most cases), and hence, can be used in high-vacuum systems. Due to their wide electrochemical windows and good thermal stability, these liquids can be used as solvents for electrodeposition of metals, their alloys and semiconductors, which could formerly only be obtained from high temperature molten salts. Furthermore, ILs are also known as “designer solvents”, as their physicochemical

properties can be tuned by varying the cation and/or anion chemical structure to satisfy application requirements.

2.2.1 Melting Point and Thermal Stability

Ionic liquids have a much wider liquidus range than common molecular solvents. The solid-liquid transition temperature of these salts is, by definition, below 100 °C. Most of the liquids are molten at room temperature with melting temperature as low as -50 °C. However, in some liquids having long aliphatic side chains in the cation, a glass transition is observed instead of a melting point. Consisting solely of ions with relatively weak ion-ion pairing, these systems have an extremely low vapour pressure. The upper temperature limit is usually determined by thermal decomposition. The thermal stability of ILs is limited by the strength of their heteroatom–carbon and heteroatom–hydrogen bonds [37]. Some ILs are stable up to 350 °C – 450 °C, at least on a short time scale. Both the cation and anion have an influence on the melting point of the IL that depends on the size, charge and distribution of charge on the ions of the salts. The melting point usually decreases with increasing of the anion and/or cation size and asymmetric substitution due to the weaker coulombic interactions in the crystal lattice [38, 39].

2.2.2 Vapour Pressure

Negligible vapour pressure is one of the extraordinary properties of ILs. ILs do not evaporate significantly at room temperature even under ultrahigh vacuum (UHV) conditions, which opens a possibility to apply them in UHV systems. Initially it was supposed that most ILs decompose by increasing the temperature without evaporation. However, distillable ILs can be prepared by neutralization of volatile bases with volatile acids [40]. Furthermore, in 2006 Earle et al. [41] reported that some aprotic ILs (e.g. 1-ethyl-3-methylimidazolium bis(trifluoromethylsulfonyl)amide ([EMIm]TFSA)) can be vaporized at 200-300 °C under low pressure (< 0.1 mbar) without decomposition and then recondensed at low temperature.

2.2.3 Viscosity and Density

Ionic liquids are usually much more viscous than common molecular solvents due to strong intermolecular interactions: electrostatic interactions, hydrogen bonding and van der Waals forces [42-44]. The viscosity of ILs ranges from about 10 mPa·s to 500 mPa·s at room temperature. Since stronger van der Waals forces cause the increase in energy required for molecular motion, longer alkyl chains in the cation lead

to an increase in viscosity [26]. For example, at room temperature viscosities have been reported as 312 mPa·s for [BMIm]PF_6 [45], 154 mPa·s for [BMIm]BF_4 [46] and 52 mPa·s for 1-butyl-3-methylimidazolium bis(trifluoromethylsulfonyl)amide ([BMIm]TFSA) [26]. ILs with fluorinated anions such as $[BF_4]^-$ and $[PF_6]^-$ have rather high viscosities due to hydrogen bonds. The viscosity temperature dependence in ILs is more complicated than in molecular solvents, as most of ILs do not show Arrhenius behaviour [47]. However, with increasing temperature the viscosity significantly decreases. The high viscosity of ILs is their major disadvantage as it negatively affects mass transfer in ILs. The viscosity of the IL plays an important role for *in situ* STM and AFM measurements, as the tip damping should not be too strong to obtain STM/AFM images with high resolution.

Ionic liquids are usually denser than water and their densities range from 1 to 2.3 $g \cdot cm^{-3}$. The density is affected both by cation and anion and almost linearly decreases with increasing the length of alkyl chain in the cation [48].

2.2.4 Ionic Conductivity

The ionic conductivity of electrolytes generally depends on available charge carriers and their mobility and is inversely linked to their viscosity. Since ILs are composed solely of ions, it would be expected that ILs have high conductivities. However, the ion mobility in ILs is usually low at room temperature due to the large size of ions, ion pair formation and/or ion aggregation. Therefore, at room temperature ILs have rather low conductivities in the range of 0.1 - 30 $mS \cdot cm^{-1}$ [6, 44]. The highest conductivity (up to 110 $mS \cdot cm^{-1}$ at 298 K) has been reported so far for 1,3-dialkylimidazolium fluorohydrogenate ionic liquids [49]. With increasing temperature the conductivity of ILs rises.

2.2.5 Solvation Ability

Ionic liquids are good solvents for a variety of organic and inorganic compounds [28]. It was found that the solvent properties can be determined by the ability of the salt to act as a hydrogen bond donor and/or acceptor and the degree of localization of the charges on the anions [2]. The solvation in ILs arises through various solute-solvent interactions, such as ion-ion and dipole-dipole interactions, hydrogen bonding, halogen bonding, van der Waals forces, etc. Therefore, the structure of the cation and/or anion of IL plays an important role in the dissolution process of solutes [50].

2.2.6 Electrochemical Window

The electrochemical stability of a solvent is one of the most important properties for electrochemical applications. The electrochemical stability is usually determined by the electrochemical window, the electrochemical potential range in which the electrolyte is neither reduced nor oxidized at an electrode (i.e. the solvent is not affected). The thermodynamic electrochemical window of water is only about 1.2 V at 298 K. Therefore, the electrodeposition of many metals and semiconductors is restricted. One important advantage of ILs over aqueous electrolytes is their wide electrochemical window (up to 6 V) that depends on the thermodynamic stability of cation and anion to reduction and oxidation, respectively. This allows the electrodeposition of various metals and semiconductors, which cannot be obtained from aqueous solutions (e.g. Ta, Nb, Al, Si, Ge, GaSb, ZnS, etc.) [29]. Fig. 2.2 gives a summary on the electrochemical windows of ILs and on some elements/compounds, which can be made electrochemically in them [1].

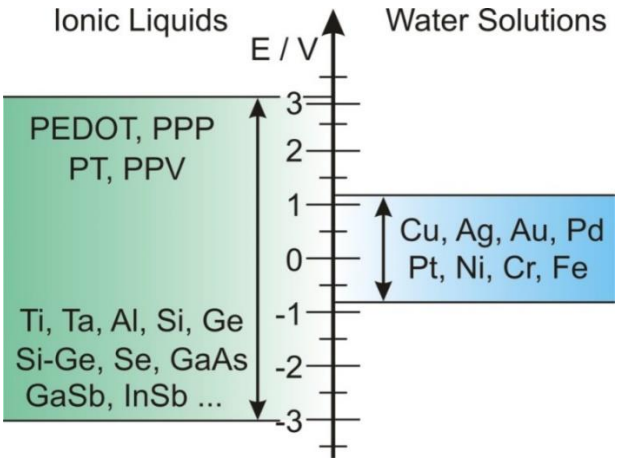

Fig. 2.2 *Sketch on the electrochemical windows of ionic liquids and on the elements/compounds, which can be made electrochemically in them. Reproduced from ref. [1]*

Cyclic voltammetry (CV) and linear sweep voltammetry (LSW) are typically used to determine the electrochemical window of ILs. It shows the cathodic and anodic potential limits of the electrolyte toward a certain reference electrode [51]. However, the presence of impurities can alter the electrochemical stability of ILs leading to a significant narrowing of the electrochemical window.

3 Scanning Probe Microscopy

Scanning Probe Microscopy (SPM) has become an essential tool in nanoscience [52, 53]. It is a powerful technique that allows studying surfaces and interfaces at the nanoscale and even on atomic levels, which is usually beyond the resolution of optical and electron microscopes. Conventional microscopes involve light waves (optical microscopes) or beams of electrons (electron microscopes) to obtain an image of the surface. In contrast, SPM produces the images of the surface by scanning an atomically sharp probe (“tip”) over a surface of the sample at a distance of a few nanometers (or even angstroms) inducing the interactions between the probe and the surface, which provides a three-dimensional (3D) topographic image of the surface. Using SPM, solid surfaces can be imaged with atomic resolution revealing, for example, a distribution of structural defects in the crystalline structure or arrangement of adsorbates at the surface. There are several different types of scanning probe microscopes, which are based on various tip-surface interactions. The most popular types are scanning tunneling microscope (STM) and atomic force microscope (AFM). In STM, the electric (tunneling) current, flowing between a metallic tip and conducting substrate, which are brought in a very close proximity but not in direct contact, is recorded. In contrast to STM, AFM measures the electrostatic forces between the tip and the surface; therefore, the sample should ideally not be conducting.

Beyond topographic imaging, SPM can also be applied to study the surface properties at the atomic level [52]. Thus, an electronic structure of the surface can be investigated with STM using spectroscopy modes (e.g. current vs. voltage curves). Furthermore, the differences in work function between tip and sample can be evaluated using force vs. voltage curves recorded by AFM. Tunneling current or force can also be measured as a function of distance between the tip and the surface of the sample, which may provide information about tip-sample interactions. Force vs. distance curves recorded by AFM can provide information about the structure of the IL/solid interface [54]. The controlled manipulation of the surfaces is another important application of SPM. For example, various nanostructures can be created in a fundamental approach with STM or AFM by moving single atoms of the surface or adsorbates [55-57].

3.1 Scanning Tunneling Microscopy (STM)

The content of this section, partly published in the PhD thesis of the author [1], was supplemented and adopted for the present thesis.

3.1.1 Introduction to STM

The era of SPM begins in 1981 with invention of the scanning tunneling microscope (STM). The first STM was built at the IBM Research Lab in Zurich by Gerd Binning and Heinrich Rohrer [58]. In 1986, the scientists were awarded with the Nobel Prize in Physics for this invention [59]. Nowadays, STM is widely used in both industrial and fundamental research to obtain 3D atomic-scale images of metal and semiconductor surfaces in real space.

The STM applies the principles of quantum mechanics. When the atomically sharp probe (the tip) is brought into close proximity with the surface of the sample (below 1 nm) and a voltage is applied between the tip and the sample (bias voltage), the electrons start to “tunnel” (quantum-mechanical effect) from the tip to the surface (or vice-versa depending on the polarity), resulting in a weak electronic current in the range of pA to nA (the tunneling current). The tunneling of an electron is a quantum-mechanical effect, which originates from wave properties of an electron. In classical physics, a particle with energy $E_{particle}$ cannot surpass a barrier with $E_{bar} > E_{particle}$ (fig. 3.1.1). The region inside the barrier is classically forbidden.

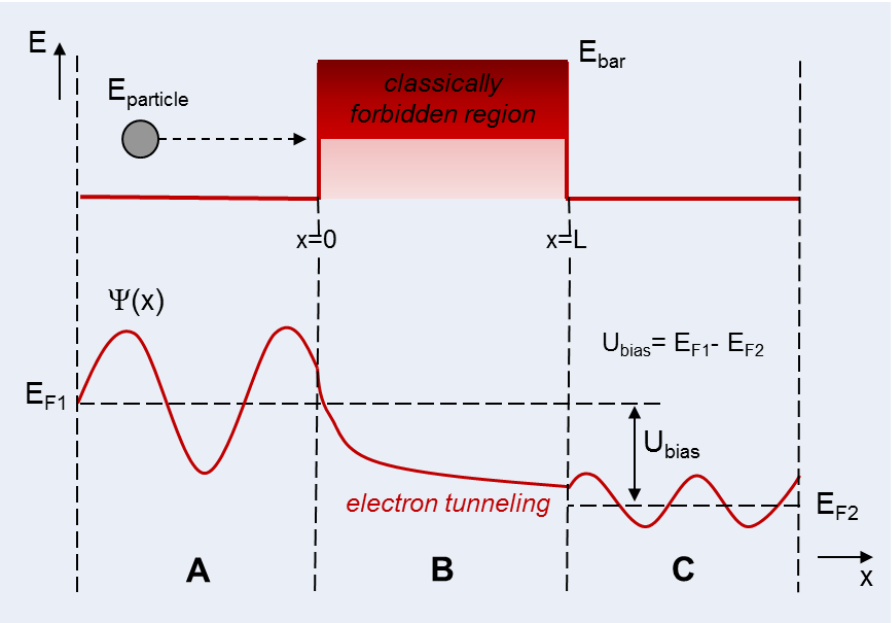

Fig. 3.1.1 *Schematic view of the one-dimensional electron tunneling.*

In quantum mechanics, an electron is described as an oscillating wave function (region A in fig. 3.1.1). By applying a bias voltage (U_{bias}), the Fermi levels on the left (E_{F1} in region A) can be shifted leading to electron passing through the barrier. There is no oscillation inside of the barrier and the wave function exponentially decreases (region B in fig. 3.1.1). If the barrier is not too wide, the wave function does not decay to zero and the oscillation begins again at the opposite side of the barrier (region C in fig. 3.1.1). Such a transport through classically forbidden zones is called tunneling [60, 61].

The probability of a particle tunneling through a barrier can be calculated with the help of the Schrödinger equation [61]. The particle of mass *m* with energy *E* approaching a barrier is described by a wave function $\Psi(x)$ that must satisfy the time-independent Schrödinger equation in the form:

$$-\frac{\hbar^2 d^2\psi(x)}{2mdx^2} = (E - U(x))\psi(x), \tag{3.1}$$

where *U(x)* is the potential energy at the point *x*, $\hbar = \frac{h}{2\pi} = 1.05457 \times 10^{-34}\, Js$.

On the left of the barrier (region A, x<0) the potential energy is zero (*U(x) = 0*) and the Schrödinger equation has the solution:

$$\psi_A = Ae^{ikx} + Be^{-ikx}, \qquad k\hbar = (2mE)^{1/2} \tag{3.2}$$

where *A* and *B* are constants.

The wave function decays exponentially inside of the barrier (region B, $0 \le x \le L$) and the potential energy is the constant *U(x)=U*:

$$-\frac{\hbar^2 d^2\psi}{2mdx^2} + U\psi = E\psi \tag{3.3}$$

Since (*U-E)* is positive, the general solutions of (3.3) are

$$\psi_B = Ce^{kx} + De^{-kx}, \qquad k\hbar = \left\{2m(U-E)\right\}^{1/2} \tag{3.4}$$

For the right of the barrier (region C, $x > L$), where *U(x)=0*:

$$\psi_C = A'e^{ikx} + B'e^{-ikx}, \qquad k\hbar = (2mE)^{1/2} \tag{3.5}$$

The complete wave function consists of an incident wave, a wave reflected from the barrier, the exponential decay inside of the barrier, and a transmitted wave after

tunneling through the barrier. As the complete wave function and its first derivative must be continuous at the edges of the barrier (x=0 and x=L), a system of four equations with six unknown coefficients is obtained [61]:

$$A + B = C + D \qquad Ce^{kL} + De^{-kL} = A'e^{ikL} + B'e^{-ikL} \tag{3.6}$$

$$ikA - ikB = kC - kD \qquad kCe^{kL} - kDe^{-kL} = ikA'e^{ikL} - ikB'e^{-ikL} \tag{3.7}$$

where L is the width of the barrier and $B' = 0$ as the particle is traveling from the left of the barrier and there are no particles, which are traveling from the right to the left of the barrier. However, $B \neq 0$ as the particle can reflect back from the barrier.

According to Born's statistical interpretation, the probability of finding the particle with the wave function ψ in the particular point of space is proportional to the square of its wave function $\psi \cdot \psi = |\psi|^2$ [61]. Therefore, the probabilities of finding the particle in the regions A, B and C are $|\psi_A|^2$, $|\psi_B|^2$, $|\psi_C|^2$, respectively. The probabilities of a particle moving towards positive x in the regions A and C are proportional to $|A|^2$ and $|A'|^2$, respectively. The ratio of these two probabilities is called transmission probability (T), which determines the probability of a particle to pass through the barrier. After some algebra the transmission coefficient can be defined as [61]:

$$T = \left\{1 + \frac{(e^{kL} - e^{-kL})^2}{16\varepsilon(1-\varepsilon)}\right\}^{-1}, \qquad \varepsilon = \frac{E}{U} \tag{3.8}$$

When the barrier is high and wide ($kL >> 1$) the transmission probability can be found as:

$$T = 16\varepsilon(1-\varepsilon)e^{-2kL}, \qquad k = \frac{(2mE)^{1/2}}{\hbar} \tag{3.9}$$

In STM, the work function of electrons in the metals determines the barrier, as the barrier is given by the gap between tip and sample. In this case, the transmission coefficient exponentially decreases with the distance between the tip and the surface of the sample and exponentially decays with the square root of the work function. Unfortunately, this model cannot be directly applied to STM, as it is valid for one-dimensional electron tunneling. In the case of STM, a three-dimensional geometry should be considered.

There are several theoretical models of STM [62]. The standard theoretical model for STM was developed in 1985 by Tersoff and Hamann [63, 64]. The model is based on the Bardeen's perturbation theory [65]. The tunneling current in perturbation theory is ascribed by Fermi's golden rule:

$$I_t = \frac{2\pi e}{\hbar}\sum_{st}(f(E_t)[1-f(E_s+eV)][M_{ts}]^2\delta(E_t-E_s)) \tag{3.10}$$

$$f(E) = \frac{1}{1+e^{(E-E_F)/k_BT}}$$

Where *f(E)* is the Fermi function; E_F is the Fermi level; *V* is the applied voltage (bias voltage); M_{ts} is the tunneling matrix element; k_B is the Boltzmann constant; E_t and E_s are the energy of the states ψ_t and ψ_s, respectively, in the absence of tunneling. Bardeen [65] showed that the tunneling matrix element is

$$M_{ts} = \frac{\hbar}{2m} = \int_{surface}^{tip}(\psi_s^*\frac{\partial\psi_t}{\partial z} - \psi_s\frac{\partial\psi_t^*}{\partial z})dS \tag{3.11}$$

where ψ_s and ψ_t are the wave functions of the sample and the tip. The integral is calculated between the surface of the sample and the tip.

This means that the tip probes the profile of the Fermi surface, if the tunnel current is constant during the STM experiment. The tunneling voltage should be low to get a reliable image of the investigated surface. Therefore, for low voltages (~ 10 mV) and low temperatures (room temperature and below) the formula (3.11) is simplified to:

$$I_t = \frac{2\pi e^2 V}{\hbar}\sum_{ts}|M_{ts}|^2\,\delta(E_t-E_F)\delta(E_s-E_F) \tag{3.12}$$

The microscopic geometry of the tip depends on the tip preparation and therefore is different for each case. Tersoff and Hamann have assumed that the tip wave function can be approximated by a spherical s-wave function [63, 64]. In this case, the tunneling current (I_t) at the distance *z* is proportional to the local density of states (LDOS) of the sample at the Fermi level (E_F) at the center of the curvature of the tip:

$$I_t = \frac{32\pi^3 e^2 V\phi^2 R^2 e^{2kR}}{\hbar k^4} D_t(E_F)\,p(\vec{r_0};E_F) \tag{3.13}$$

Where ϕ is the work function of the tip, which is assumed equal to the work function of the sample, for simplicity; *R* is the radius of the curvature of the tip; *k* is the inverse

matrix of the wave function in vacuum; $D_t(E_F)$ is the LDOS of the tip at the Fermi level; and $p(\vec{r_0}; E_F)$ is the LDOS of the sample at the Fermi level under the center of the curvature of the tip.

Based on the Wentzel-Kramers-Brillouin (WKB) approximation the tunneling current for the low bias voltages (few hundred mV) is more straightforward [66, 67]:

$$I_t = \int_0^{eV} p_s(\vec{r_0}, E)\, p_t(\vec{r_0}, E - eV) T(E, eV, z) dE \tag{3.14}$$

$$T(E, eV) = \exp\left(\frac{-z\sqrt{8m}}{\hbar}\sqrt{\frac{\phi_s + \phi_t}{2} + \frac{eV}{2} - E}\right) \tag{3.15}$$

where $p_s(\vec{r_0}, E)$ and $p_t(\vec{r_0}, E - eV)$ are the LDOS of the sample and of the tip at the position $\vec{r_0}$; E is the energy related to the individual Fermi level; z is the distance between the tip and the sample; $T(E, eV, z)$ is the transmission probability, ϕ_s and ϕ_t are the work functions of the sample and of the tip, respectively.

If the distance between the tip and the sample is kept constant ($z = const$), and if it is assumed that the LDOS of the tip and of the sample have constant values, the equation for the tunneling current is simplified to:

$$I_t = const \int_0^V \exp(-\sqrt{\phi - V}) dV \tag{3.16}$$

Then for the constant bias voltage ($V = const$):

$$I_t = const \exp(-z\sqrt{\phi}) \tag{3.17}$$

where ϕ is the arithmetic mean of the work functions of the sample and of the tip.

There are two main characteristics: i) the tunneling current decays exponentially with increasing the distance between the tip and the surface of the sample and ii) the tunneling current decreases exponentially with the square root of the work function. Very small changes in the tip-sample separation induce large changes in the tunneling current, which can be measured very precisely. As the tunneling current depends on the electronic structure of the surface, surfaces with different chemical composition may show different contrasts in STM. The information on the electronic structure of the surface can be obtained by applying scanning tunneling spectroscopy (STS). The barrier height or the LDOS of a sample's surface can be determined from STS data by

varying one of the tunneling parameters (I_t, U_{bias}, or z) [52, 60]. Co-analysis of the surface morphology and tunneling spectra provides information about the distribution of different phases on the surface of the composite. Furthermore, the effective work function can be determined from (3.17) by fitting an exponential function to the measured tunneling current.

Modern STM can be operated in various environments, e.g. ultrahigh vacuum, at atmospheric pressures and in liquids. However, the tunneling mechanism in liquids and in vacuum should be different. Similar to vacuum, the tunneling current in liquids is exponentially proportional to the tip-surface separation but depends on the applied electrolyte [68-71].

3.1.2 STM Instrumentation

Commercial STM heads are based on a common design [66]. In this study, STM experiments were performed with in house designed STM heads and scanners. The design of the STM head and scanner and the main instrumentation principles were discussed in detail in ref. [1]. In this section the main design principles of the STM head and scanner applied in this work are summarized.

As described in the previous section (Chapter 3.1.1), in STM the tunneling current flows between the surface of interest and an atomically sharp metal tip located over the sample surface at a typical distance of $z < 1$ nm. This is one key requirement of STM for nanoscale imaging of the surface. The tunneling current and the tip-surface separation are control parameters in STM experiments. Therefore, the mechanics should do three things: i) bring the tip into tunneling distance (approaching), ii) keep the tip stable at the tunneling distance and iii) scan the tip over the sample. Scanning of the surface is done by a linear movement of the tip over the surface. In the most STM heads, the coarse approach of the tip is performed by precision micrometer screws driven by step motors, while a piezoelectric tube (inside of a piezoelectric scanner) ensures a precise adjusting of the tip position, in order to obtain 3D-images of the sample surface.

A schematic illustration of the STM operation is presented in fig. 3.1.2. An atomically-sharp metallic tip is brought into a close proximity with the sample. The tunneling current flowing between the tip and the surface by applying a bias voltage is measured with a preamplifier and depends exponentially on the distance between the tip and the surface. This signal is fed into a feedback loop to keep tunneling current or tip position (height) constant during lateral (x,y)-scanning. In order to obtain 3D images, the tip is

connected to a piezoelectric tube (located inside of a piezoelectric scanner) with one electrode inside and four electrodes outside of the tube. If a voltage is variably applied between inner and outer electrodes of the piezo, the piezo undergoes bending, which leads to a two-dimensional (x,y) movement of the tip over the surface. Applying a voltage between all four outside electrodes and the inner one causes the expanding or contraction of the piezo, which in turn, leads to a vertical (z) movement of the tip via the inverse piezoelectric effect.

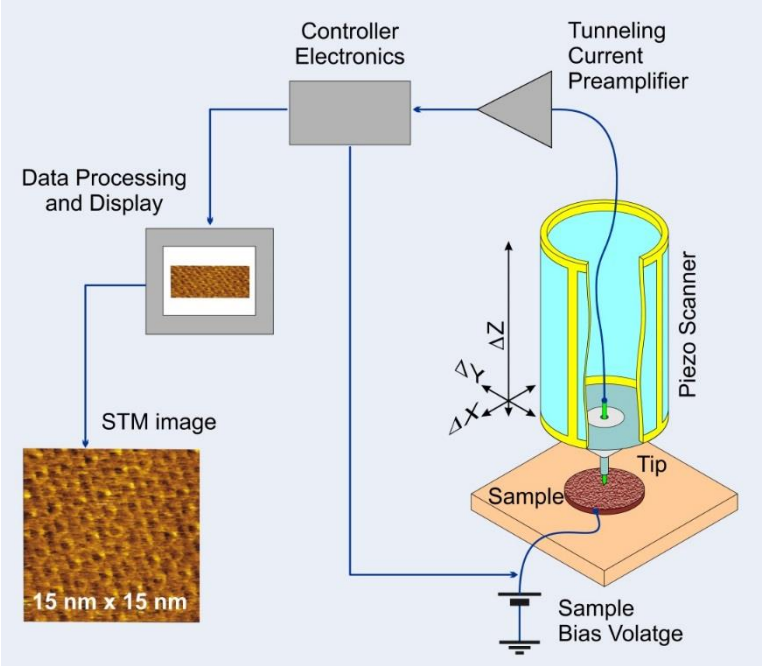

Fig. 3.1.2 *Sketch of the STM. A sharp tip is connected to a piezoelectric scanner, which moves the tip over the sample surface. The tunneling current is measured by a preamplifier. The signal is proceed in feedback loop, which is recorded by a computer as a function of the (x,y)-position that corresponds to the topography of the sample surface.*

The feedback signal (the tunneling current and thus the position of the tip) is recorded by a computer as a function of the (x,y)-position, which usually corresponds to the topography of the sample surface. Typical voltages applied to a piezo tube are in the range of ± 300 V. As common piezo tubes cannot move the tip for more than ~ ± 1 μm in z-axis, the coarse approach is done (in the home-built STM head at the institute) by three micrometer screw gears driven by a step motor each (fig. 3.1.8).

The tunneling current is originated by the bias voltage (which is usually 5 ~ 500 mV in electrochemical experiments) and measured by a current-to-voltage converter based on an operation amplifier (OPA) (fig. 3.1.3). The output of the OPA is connected to its inverting input (via resistor R), which sets up a negative feedback loop. As a result,

both inputs of the OPA are at the same potential. It means that the tip has always a potential given by the bias voltage.

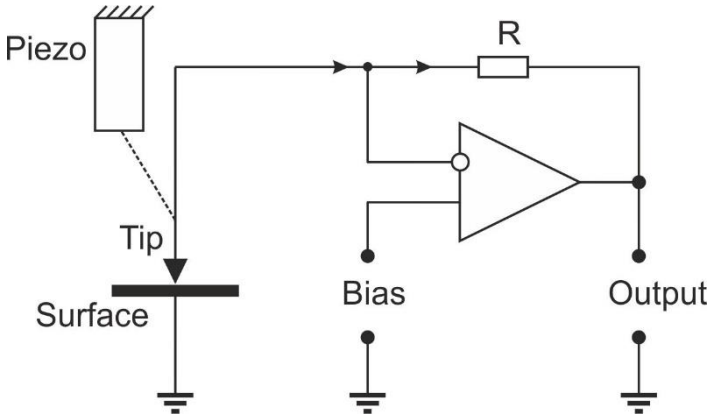

Fig. 3.1.3 *The circuit of the preamplifier for the STM tip. The operation amplifier (OPA) provides the bias voltage on the tip. Adapted from ref. [1]*

In the shown configuration the output voltage U_{out} is proportional to the tunneling current i_{tun}:

$$U_{out} \sim i_{tun} R \tag{3.18}$$

As a consequence, the output voltage U_{out} contains information on the tunneling current and can be further processed for external feedback loop.

In practice, the STM can be operated in two modes: in the *constant current mode* or in the *constant height mode*, as two limiting cases. In the case of the *constant height mode* the tip has a fixed z-position and is moved in the (x,y)-plane over the surface. The advantage of this mode is that high scanning rates can be achieved that can be used, for example, to observe dynamical processes. The measurement is faster than in the case of the *constant current mode*, however, there is an increased risk of crashing the tip. Therefore, the *constant height mode* is usually applied when the surface under investigation is atomically flat and not tilted.

If the investigated surface is rough, the STM experiment is operated in the *constant current mode*. In this case, the feedback loop is used to keep the tunneling current constant by adjusting the height of the scanner at each measurement point (fig. 3.1.4). For example, when the system detects an increase in tunneling current, it adjusts the voltage applied to the piezoelectric scanner to increase the distance between the tip and the sample. As the elongation of the piezo is (to a considerable degree) linearly depending on the applied voltage, this operating voltage is used for the profile measurement. In the *constant current mode* irregular surfaces can be measured with

high precision but -in comparison to the *constant height mode*- the measurement takes more time.

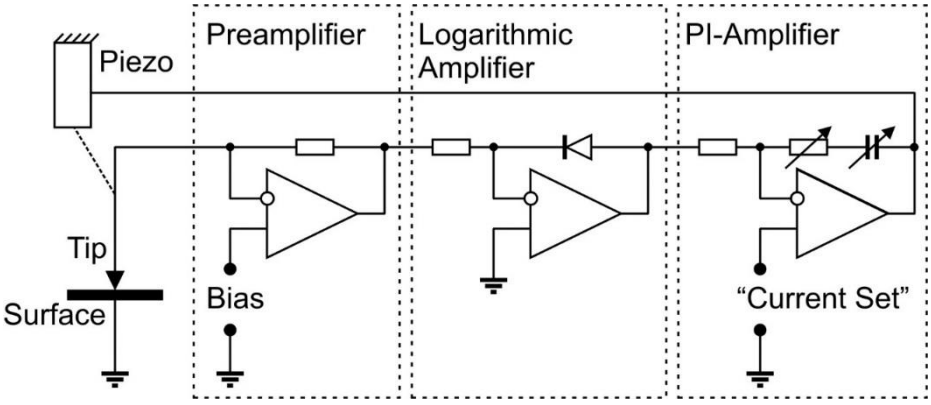

Fig. 3.1.4 *The feedback loop for controlling the z-position of the tip in the constant current mode. The tunneling current passes over the preamplifier, a cascade subtracting the bias voltage from the output signal of the preamplifier (not shown), and the logarithmic amplifier. Then, the signal is compared with the preset value in the PI amplifier, and the necessary corrections of the z-position of the tip are adjusted by the piezo. Reproduced from ref. [1]*

Historically, the first STM experiments were carried out in UHV, followed by experiments under ambient conditions and even in liquids. Furthermore, it is possible to perform electrochemical (*in situ*) STM measurements in electrochemical (charged solid/electrolyte) systems under galvanostatic or potentiostatic control. Recently, *in situ* STM has become a powerful tool for probing of various electrochemical processes in real space with atomic-scale resolution [72, 73]. However, it is important to note that the tunneling mechanism in ionic liquids is not yet fully understood.

In the *in situ* STM the tunneling current flows between a metallic tip and a solid conductive sample, which are both immersed into the liquid solution (electrolyte). During the measurement the sample also serves as a working electrode in a standard three electrode electrochemical cell containing a reference electrode and a counter electrode to complete the cell. In principle, it is easy to combine the STM with a potentiostat to make electrochemical experiments possible (fig 3.1.5).

The circuit shows that the STM tip unavoidably acts as an electrode in the electrochemical cell. As soon as a voltage is applied to the tip, an electrochemical current can flow. Such Faradaic currents (e.g. the deposition of metal, hydrogen or oxygen evolution) can easily reach some hundreds of nanoamperes. Macroscopically this is negligible but as the tunneling currents are only some nanoamperes, the tip has to be isolated by paint or by glass with the exception of its very end. Thus, the faradaic

currents can be reduced down to the picoampere regime making stable tunneling conditions under electrochemical conditions possible.

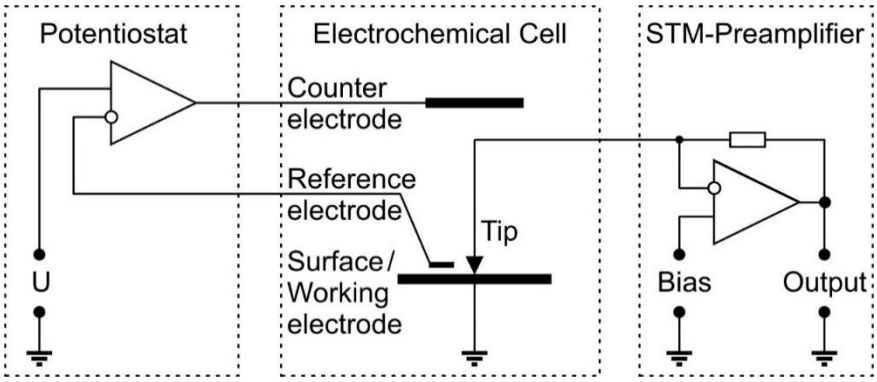

Fig. 3.1.5 *In situ STM: connection of the electrochemical cell with the potentiostat and the STM controller. As all the parts have a common ground connection, the electrochemical and STM experiments can be performed independently. Reproduced from ref. [1]*

A good tunneling tip is an important requirement to obtain high resolution STM images. The preparation of tunneling tips is not a trivial subject and there are still many unknown parameters. Both the material and the shape of the tip play an important role in the tunneling process (equation (3.14)). STM tips are usually made from metal wires of tungsten, platinum-iridium or gold. They are sharpened by mechanical grinding, cutting with a wire cutter, field emission/evaporation, ion milling, electrochemical etching, etc. [60]. However, an oxide layer may exist on the surface of the tip that makes acquiring of STM images difficult. Platinum is inert to oxidation and the addition of iridium adds stiffness, while the Pt/Ir alloy is formed. Therefore, Pt/Ir (90:10) wires of 0.25 mm in diameter are used as a material for the tip preparation in the experiments presented here. The STM tips are prepared by electrochemical etching in 4M NaCN solution followed by electrophoretic coating with an electropaint (e.g. from BASF (ZQ 84-3225 0201)) and then by annealing at 100 °C for 1 hour and subsequently at 200 °C for 10 min. The tips, prepared in such a way, are usually completely insulated except of very end (atomically sharp in an ideal case) and deliver a good quality of STM images.

In the present study *in situ* STM experiments were performed with in house designed STM head, scanner and electrochemical cell under inert gas conditions with a Molecular Imaging PicoScan 2500 STM controller in feedback mode. The sketch of the STM head used in this study is presented in fig. 3.1.6. The STM head is based on a stainless steel ground plate (1). Three stepping motors (2) are mounted on the ground plate (1) at an angle distance of 120 °. Three precision micrometer screws (3) are

driven by the motors via worm-gears (4). A stainless steel plate (5) holding the electrochemical cell (6) is guided by three stainless steel rods (7) and supported by springs (8) at the end of these rods. The springs fix the cell holder to the hemispherical heads (9) of the micrometer screws, which move the holder up and down during the experiment.

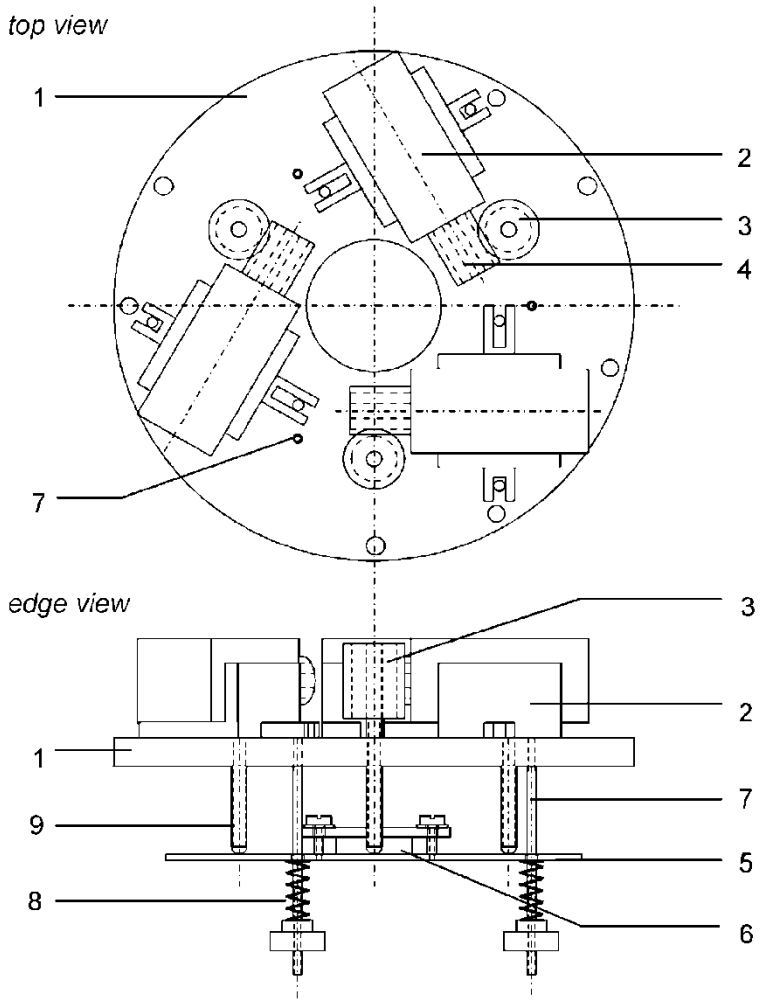

Fig. 3.1.6 *Drawing of the home-built STM head (not in scale): 1 - base plate, 2 - step motor, 3 - micrometer screw, 4 - worm gear, 5 - cell holder, 6 - electrochemical cell, 7 - guiding rod, 8 - spring, 9 - hemispherical head of the micrometer screw. Reproduced from ref. [1]*

A principle design of the scanner is presented in fig. 3.1.7. The scanner housing is made from a stainless steel hollow cylinder (1). The piezo-tube (2) is glued to a socket (3) made from Corning MACOR that is screwed via a stainless steel ring (4) into the scanner housing (1). At the other end of the piezo-tube a ring made from MACOR (5) is glued onto a stainless steel socket (6). The tip holder is made from three parts: the stainless steel capillary (7) as the tip holder is mechanically pressed into a polytetrafluoroethylene (PTFE) rod (8) for insulation purposes, which then is pressed into a stainless steel flange (9). This flange is screwed into a socket (6), which is

connected with a piezo. The flange below (10) is screwed to the flange (9) with a graphite powder. The stainless steel cover (11) is connected with the scanner housing the same way. As many connections are made by screws, in case of damage any part of the scanner can be exchanged easily.

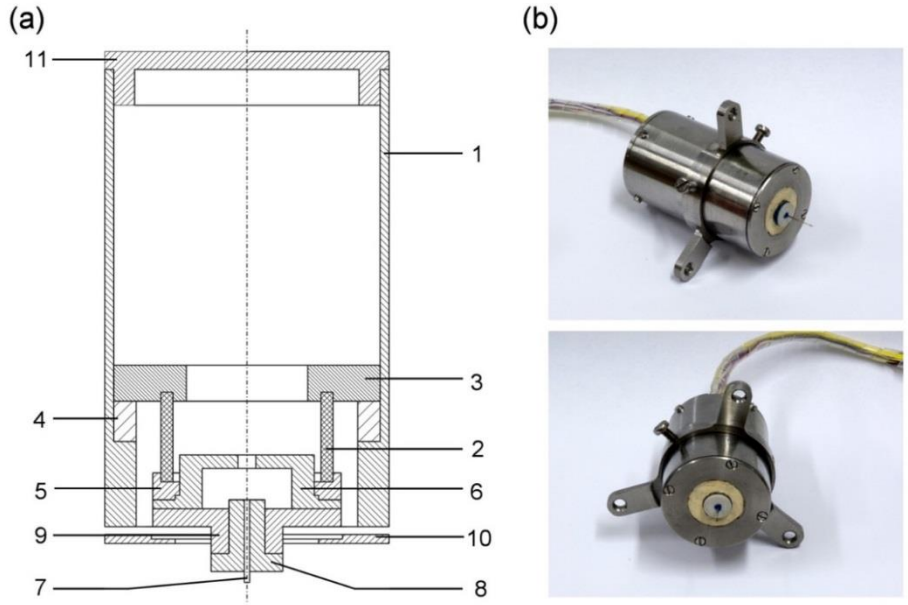

Fig. 3.1.7 *(a) Drawing of the STM scanner (not in scale): 1 - scanner housing, 2 - piezo tube, 3 - socket made from MACOR, 4 - stainless steel ring, 5 - MACOR ring, 6 - stainless steel socket, 7 - tip holder, 8 - PTFE rod, 9 - stainless steel flange, 10 - flange of the below, 11 - stainless steel cover. (b) Photographs of the STM scanner. Reproduced from ref. [1]*

Assembling of the STM head and filling of the electrochemical cell were performed in an argon-filled glove box with water and oxygen contents below 2 ppm (OMNI-LAB from Vacuum-Atmospheres). As represented in fig. 3.1.8, the scanner housing (10) is mounted in a central boring of the base plate (1) and fixed by three screws. The STM head was placed subsequently inside an argon-filled stainless steel cylinder, thus ensuring inert gas during STM experiment, transferred to the air-conditioned laboratory with a constant temperature of 23 ± 1 °C and placed onto a vibration damped table from IDE (Germany). Temperature plays an important role in STM experiments. As can be seen from the equation (3.14), the Fermi functions of tip and sample are temperature dependent. Thermal fluctuations and thermal drift reduce the quality of STM images. In order to reduce thermal drift and hysteresis of the piezo to a minimum, the retracted STM scanner was kept scanning overnight with maximum scan range, thus reducing thermal drift as well as possible. In all experiments the STM pictures were obtained by scanning from the bottom to the top of a picture with a scan rate 2 Hz and a resolution of 512 pixels per line. For the current-voltage tunneling spectroscopy the tip was positioned on the site of interest and the tip voltage was varied between an

upper and a lower limit. During this measurement the feedback is automatically switched off by the software.

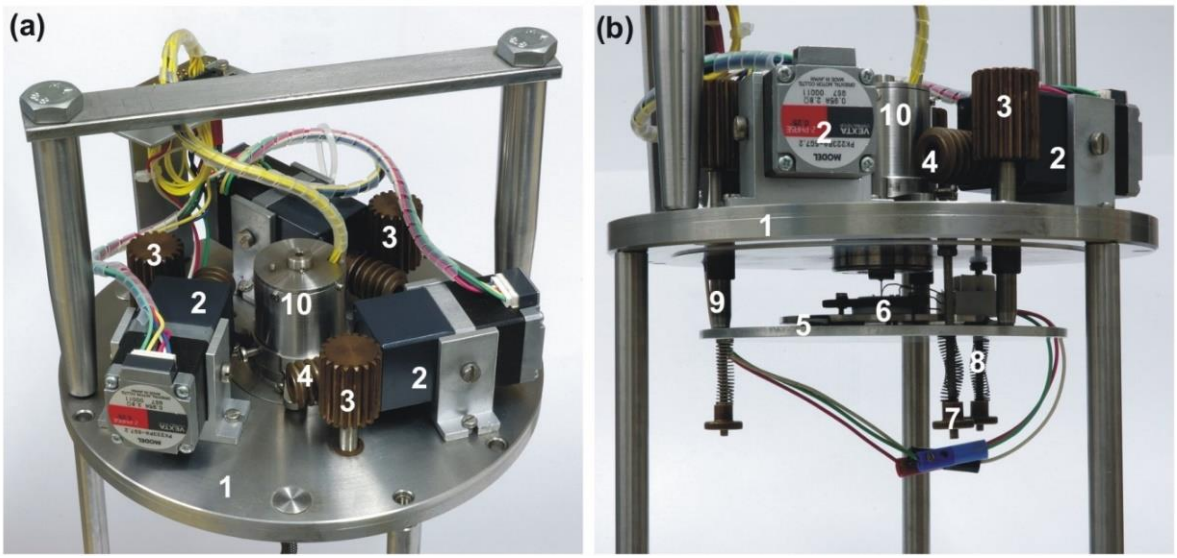

Fig. 3.1.8 *Photographs of the home-built STM scanner and head: 1 - base plate, 2 - step motor, 3 - micrometer screw, 4 - worm gear, 5 - cell holder, 6 - electrochemical cell, 7 - guiding rod, 8 - spring, 9 - hemispherical head of the micrometer screw, 10 - scanner. Reproduced from ref. [1]*

The electrochemical cell was made of Polytetrafluoroethylene (PTFE) and clamped over a PTFE covered Viton O-ring onto the substrate, thus yielding a geometric surface area of the working electrode of 0.3 cm^2 (fig. 3.1.9).

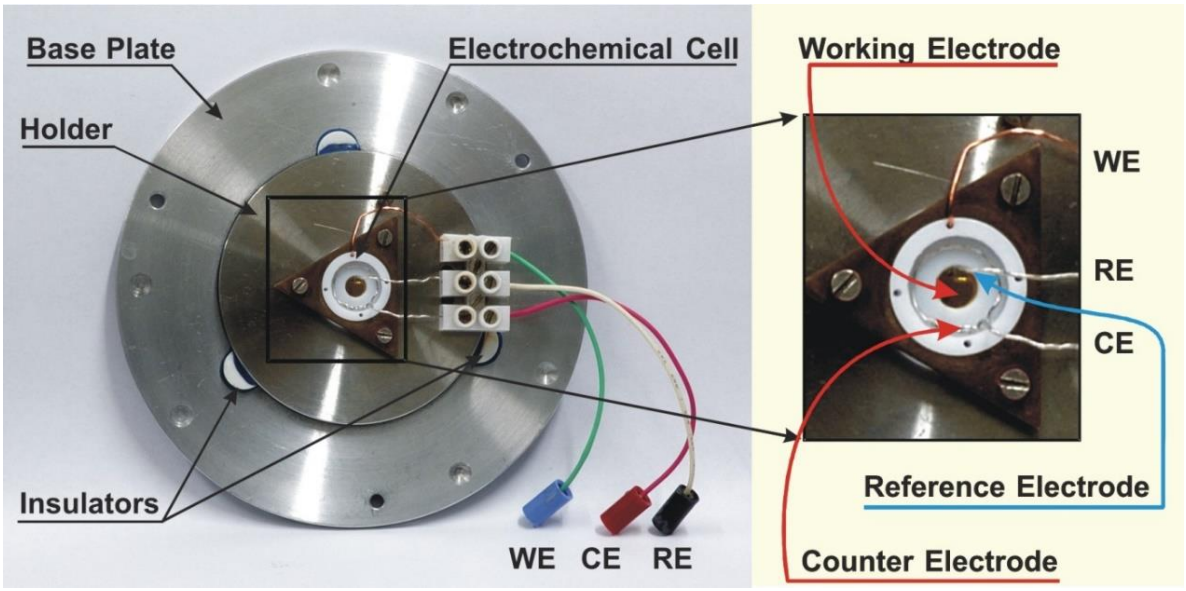

Fig. 3.1.9 *Photograph of the electrochemical cell. A cylindrical PTFE cell is pressed over a PTFE-covered Viton o-ring onto the working electrode (WE). A triangular flange fixes the cell by three screws onto a stainless steel holder, which is connected via insulators to a stainless steel base plate. A Pt-ring and a Pt-wire immersed in the cell serve as counter (CE) and reference (RE) electrodes, respectively. Reproduced from ref. [1]*

In the present study, the polarized IL/solid interfaces were investigated both in the pure ILs and in the presence of various solutes. The substrates of interest were Au(111), highly ordered pyrolytic graphite (HOPG) and H-terminated p-doped Si(111), which were connected as working electrodes (WE) in different experiments. Au(111) (a 300 nm thick film on mica), HOPG and p-Si(111) substrates were purchased from Molecular Imaging, Plano GmbH and CrysTec GmbH, respectively. Prior to use, the Au(111) substrates were carefully heated in a hydrogen flame and HOPG was freshly cleaved to minimize possible surface contaminations as well as possible.

For making the H-terminated silicon, a three-step procedure was applied [74]. The Si(111) was first sonicated in ultrapure acetone (99.9 %, sigma Aldrich). Then the substrate was dipped into a hot solution (100 °C) of 1:4 H_2O_2/H_2SO_4 for 10 minutes followed by washing in demineralized, UV treated and filtered (0.055 $\mu S\ cm^{-2}$) water and drying in a nitrogen flow. The substrate was then introduced into a 1% HF solution for 30 seconds at 22 °C followed by washing in distilled water and drying with nitrogen. Finally, for hydrogen termination, the Si(111) substrate is introduced into a 40 % aqueous NH_4F solution at 22 °C for 15 minutes. The Si(111) is then washed again in distilled water and dried under nitrogen. All the above mentioned acid solutions are extremely hazardous and utmost care must be taken in handling them.

A Pt-wire was used as a quasi-reference electrode (RE). As commonly known, the Pt-quasi reference electrode is not perfect as its electrode potential is easily affected even by slight changes in electrolyte composition. However, if an ultrapure ionic liquid under inert gas conditions is employed, as done in these experiments, the Pt-quasi reference is stable enough, allowing to determine its electrode potential vs. for example a well-known redox couple like ferrocene/ferrocinium. Only upon a massive electrolysis, the Pt-quasi reference electrode gets unstable, according to the experience at the institute. An advantage, which justifies the use of the Pt-quasi reference, is that a contamination by species from the reference electrode compartment e.g. from Ag/Ag^+ is avoided. It is still a challenge to construct perfect reference electrodes for STM experiments in ionic liquids. A Pt-ring electrode was used as the counter electrode (CE). There is no dissolution of platinum in the employed ILs. The Pt-electrodes were cleaned in a hydrogen flame before use to remove organic impurities.

In general, the tunneling voltage (bias) should be small (few hundred mV) to get a reliable STM image of the investigated surface, but in practice the applying of a low tunneling voltage leads to a tip crash due to the short distance between the tip and the

sample. Furthermore, if the STM experiment is performed under electrochemical conditions, the tip can be altered strongly due to strong metal deposition. Therefore, the tunneling voltage should be chosen in the range of potentials where no electrochemical reaction is observed.

During the last decade *in situ* STM has been extensively used to probe the IL structure at the IL/solid interface. Combined *in situ* STM and *in situ* AFM experiments reveal that ILs are strongly adsorbed to solid surfaces and several layers are present adjacent to surface [75]. Since the typical distance between the STM tip and the surface is less than 1 nm, the ions of an electrolyte adsorbed to the surface must be involved in the tunneling process. The STM tip must move through these adsorbed layers during the scanning (fig. 3.1.10a). In this case the STM tip either images the layers, which are strongly adsorbed (fig. 3.1.10b), or ruptures them.

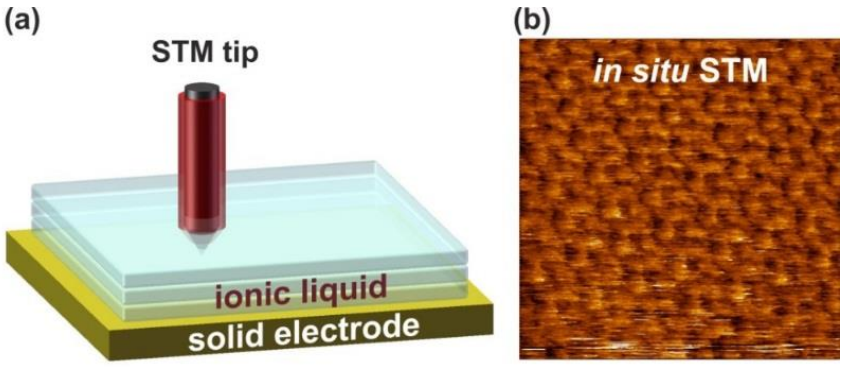

Fig. 3.1.10 *Shematic view of a STM tip probing the solid surface immersed within an IL and the real STM-image of an adsorbate recorded. Reproduced from ref. [76]*

3.2 Atomic Force Microscopy (AFM)

3.2.1 Introduction to AFM

The main disadvantage of STM is that both the tip and the sample must be conductive or semiconductive, as an electrical current has to flow between the tip and the surface. Therefore, non-conductive materials cannot be probed with STM. This limitation was overcome in 1986 by invention of the atomic force microscope (AFM), which can be used to study both conductive and insulating samples [77]. Interestingly, in the first AFM the STM-tip was mounted onto the end of a flexible cantilever and the AFM was operated only in contact mode. In contact mode, the deflection of the cantilever due to the tip-surface interactions (the short-range repulsive forces) reveals the sample surface. However, it was still challenging to probe biological samples, which are usually soft and therefore can be destroyed during AFM measurements in contact mode. The first non-contact AFM was developed by Martin et al. [78] in 1987. In non-contact mode, the cantilever oscillates close to its resonance frequency at short distances (< 10 nm) above the sample surface. The tip-surface separation remains constant during scanning. However, the amplitude, frequency and phase of the cantilever vary due to the long-range attractive forces between the tip and the surface, which reveal the surface of the sample. These forces are much lower than that one in contact mode, therefore, even very soft samples can be analysed without damage. In 1993, the first tapping mode AFM was developed [79]. In tapping mode, the oscillating cantilever taps the surface of the sample during measurement.

Similar to STM, AFM uses a sharp tip to probe the surface of the sample. However, instead of the tunneling current, in AFM the force between the tip and the sample is finally monitored. Therefore, in analogy to STM, AFM is alternatively called as scanning force microscopy (SFM). In AFM, a sharp cantilever tip interacts with the surface via local forces between the molecules of the tip and the surface. The potential energy of interaction between two non-bonding atoms or molecules can be described by the Lennard-Jones potential [61]. In the Lennard-Jones model, the intermolecular potential is due to the difference between attractive forces and repulsive forces as a function of the separation between the centers of two particles. This model is a simplified representation of the potential energy with two main approximations (hard-sphere potential and Mie potential). The hard-sphere potential can be described as follows: the potential energy (V) rises abruptly to infinity as soon as the particles come within separation d ($V = \infty$ for $r \leq d$ and $V = 0$ for $r > d$). Thus, if the particles are at an infinite

distance, the interaction between them is minimal (V=0). However, the interaction increases by decreasing the distance between the particles (fig. 3.2.1, dotted line). At some separation the particles become bound and their potential energy decreases from zero to a negative quantity until the minimum of potential energy is reached (attraction). When the particles are further squeezed together, the distance decreases and the potential energy sharply increases. The particles are getting so close that their electrons can occupy the orbitals of each other and the repulsion begins to occur as each particle attempts to retain its orbital.

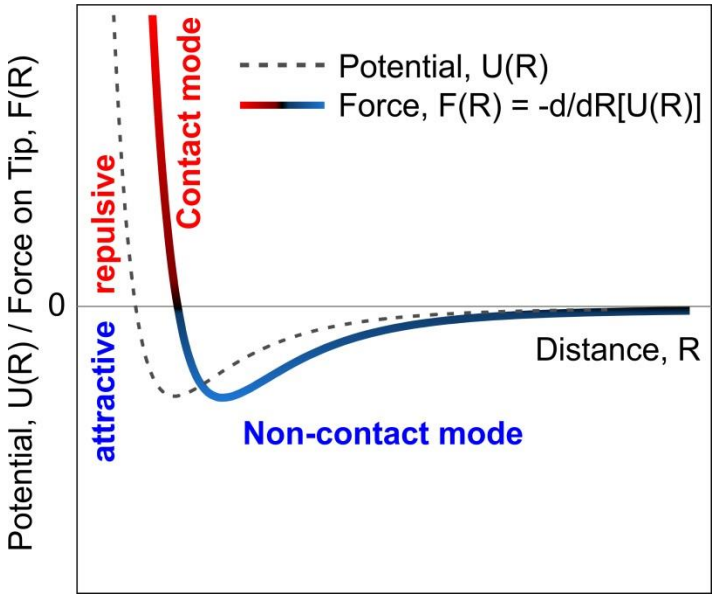

Fig. 3.2.1 *The schematic view of the Lennard-Jones potential (dotted line) and force between the tip and the sample (solid line) as a function of the tip-sample separation.*

The potential energy (*V*) can be calculated by applying the second approximation (Mie potential) [61]:

$$V = -\frac{B}{r^m} + \frac{A}{r^n}\ , \qquad \text{with n > m} \qquad (3.19)$$

where r is the distance between the centers of two particles, A and B are coefficients. The first term of (3.19) describes the attractions and the second term repulsions.

The Lennard-Jones potential is the special case of Mie potential, which fixes the exponents to m=6 and n=12:

$$V = -\frac{B}{r^6} + \frac{A}{r^{12}} \qquad (3.20)$$

The equation (3.20) is often written in the form [61]:

$$V = 4\varepsilon\left\{\left(\frac{r_0}{r}\right)^{12} - \left(\frac{r_0}{r}\right)^{6}\right\} \tag{3.21}$$

where r_0 is the separation at which V=0, ε is well depth (potential energy at its minimum).

In (3.21), $(r_0 / r)^{12}$ represents the repulsive forces, while $(r_0 / r)^{6}$ describes attraction.

In AFM, the very sharp (ideally atomically sharp) tip interacts with the atoms of the surface at the distances of less than 10 nm and the interaction force is measured. The force (*F*) between the tip and the surface is the negative slope of intermolecular potential. In the case of Lennard-Jones potential, the equation for the force takes a form:

$$F = -\frac{dV}{dr} = \frac{24\varepsilon}{r_0}\left\{2\left(\frac{r_0}{r}\right)^{13} - \left(\frac{r_0}{r}\right)^{7}\right\} \tag{3.22}$$

Figure 3.2.1 (solid line) shows the force interaction as the AFM tip approaches the sample surface. If the tip is far away from the surface, the force between the tip and the surface is negligible. When the tip moves towards the surface, first the weak attractive force occurs (fig. 3.2.1 blue line), as tip and sample atoms weakly attract each other. This zone of interaction is known as a non-contact regime. If the tip moves further, the repulsive van der Waals force predominates (intermittent contact). At very small distances (few angstroms) the total force becomes repulsive, which is known as contact regime (fig. 3.2.1, red line). Various AFM techniques operate within these three zones. However, it is important to mention that the tip-surface interaction is often complicated by additional forces, e.g. adhesive forces, capillary forces (in air), solvation forces (in liquids), which participate in the scanning process and may alter the quality and the exactness of the obtained images.

Nowadays, modern AFMs can be operated in various modes and in different environments (e.g. in UHV, at ambient pressure and in liquids) [52]. The operation modes are usually divided into static and dynamic modes. Static modes measure the static bending (deflection) of the cantilever on which the tip is mounted, while in dynamic modes the dynamic properties are obtained. Furthermore, the AFM operating modes are divided into contact and non-contact modes depending on whether the tip is in contact with the surface or not. This makes AFM a powerful technique.

3.2.2 AFM Instrumentation

Since its invention, AFM instrumentation has been essentially improved. In a static mode of operation, the force between the tip and the sample can be measured via deflection of the cantilever. For this purpose, the sharp tip is mounted at the end of micro-fabricated cantilever with a low spring constant. The cantilever acts as a spring, whose deflection is directly proportional to the force between the tip and the surface (Hooke's law):

$$F = -kx \tag{3.23}$$

where *k* is the spring constant and *x* is the change in length (i.e. the distance on which the cantilever spring bent from its equilibrium position).

The spring constant of the cantilever is dependent not only on the material from which it is made of, but also on the length and shape of the cantilever itself. The properties and dimensions of both tip and cantilever play a significant role in probing the sample surface with high quality. Nowadays, different types of cantilevers are available for AFM. The commercially available Si and Si_3N_4 cantilevers are produced with integrated tips [52]. Silicon cantilevers are usually made from a single crystalline material with pyramidal tip covered by SiO_2. Si_3N_4 cantilevers have triangular shape and the chip can contain several Si_3N_4 cantilevers with different spring constants. The cantilevers are usually coated with gold or aluminium to increase the reflectivity (e.g. for beam deflection). In general, the cantilevers should be soft enough to be deflected even by very small forces and the radius of the tip curvature should be comparable with the dimensions of the measured features.

There are different techniques to detect the bending of the cantilever (beam deflection, electron tunneling, interferometry, piezoresistance, piezoelectricity, capacitance, etc.) [52]. The beam-deflection (optical level) method is the most used technique to detect a cantilever deflection. Schematic illustration of the beam-deflection AFM is presented in fig. 3.2.2. A laser beam coming from a laser diode is focused on the back of the cantilever and reflected from the cantilever onto a position-sensitive photodiode detector. If the cantilever bends, the position of the laser spot changes. The optical level method is sensitive even for very small cantilever deflections of 0.1 nm. The AFM-cantilever is connected to a piezoelectric scanner (scanned tip AFM), which moves the tip over the sample surface. Similar to STM, the piezoelectric scanner is made of a piezoelectric tube with four outer electrodes and one inner electrode, which can bend

or expand/contract if a voltage is applied between the electrodes. This allows the precise adjusting of the tip position and to obtain 3D-images of the sample surface.

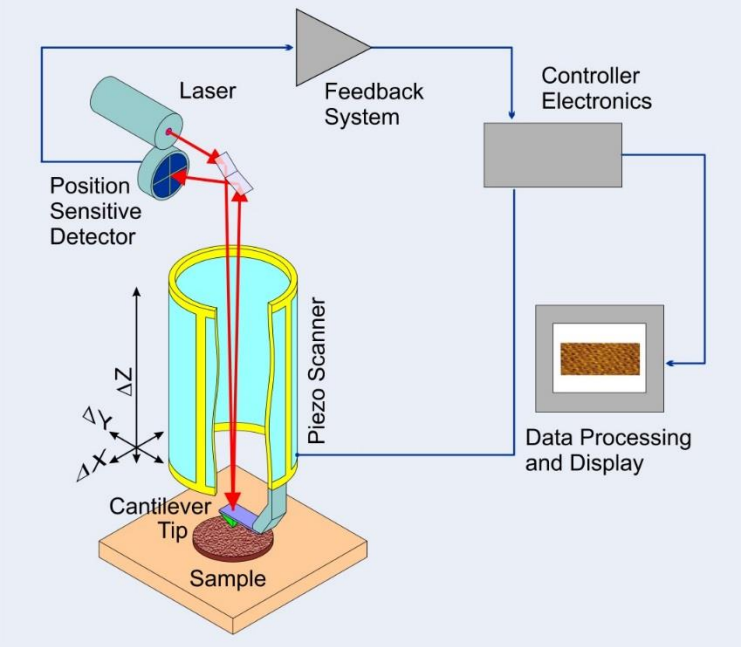

Fig. 3.2.2 *Schematic diagram of the beam-deflection scanned tip AFM. A flexible cantilever with the tip is connected to a piezoelectric scanner, which moves the cantilever over the sample surface. The deflection of the cantilever is measured with the optical level, which consists of a laser diode beam focused on the back of the cantilever and reflected onto a photodetector.*

The piezoelectric scanner can also be connected with the sample stage (scanned sample AFM, fig. 3.2.3). In this case, the sample is moved under the tip. A feedback loop allows to monitor the scanner movement by keeping the force (or tip-surface distance) constant during the measurement. The feedback signal (the force or position of the tip) is recorded by a computer as a function of the tip position, which usually corresponds to the topography of the sample surface. The beam-deflection AFM can be combined with an optical microscope (or video-camera) to improve the focusing of the laser beam on the back of the cantilever.

In analogy to STM, the AFM can be operated in two principle modes: in the *constant force mode* and in the *constant height mode*. In the case of the *constant height mode* the tip has a fixed z-position and is moved in the xy-plane over the surface. This is advantageous for the imaging of very flat samples at high resolution, as the tip can easily be damaged if the sample surface is rough. In the case of *constant force mode*, the feedback loop keeps the force constant by adjusting the height of the scanner at each measurement point.

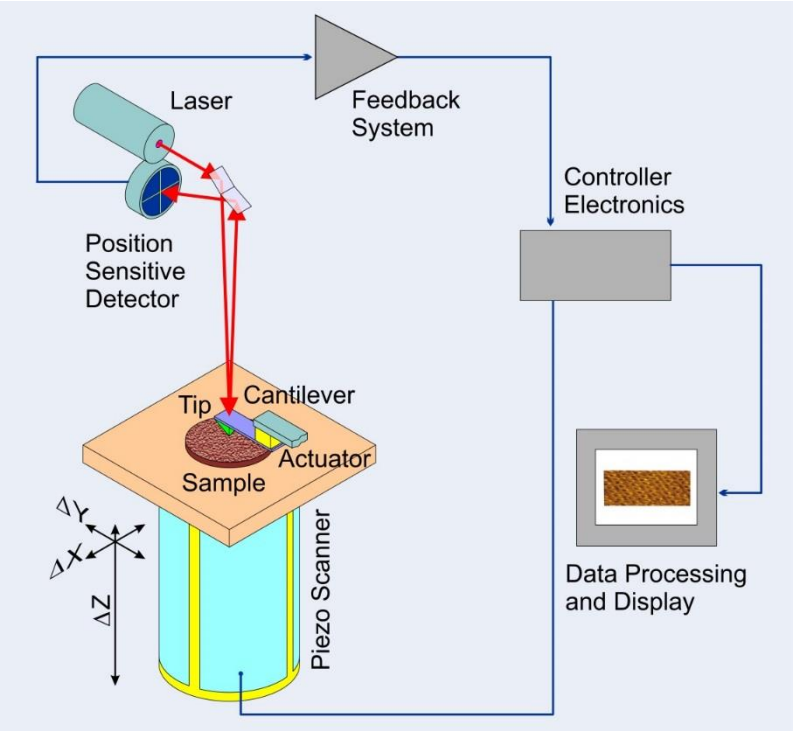

Fig. 3.2.3 *Schematic diagram of the beam-deflection scanned sample AFM. A sample stage is connected to a piezoelectric scanner. The deflection of the cantilever is measured with the optical level, which consists of a laser diode beam focused on the back of the cantilever and reflected to a photodetector.*

The AFM can be operated in a dynamic mode with oscillating cantilever [52]. In this case, the cantilever oscillates at a frequency close to its resonance frequency (non-contact mode). When the tip moves towards the surface, the vibrational properties (frequency, oscillation amplitude and phase) of the cantilever change due to the tip-surface interaction, which can be further used as a signal for monitoring tip-surface interactions. The non-contact AFM is applied for probing of soft samples, which otherwise would be destroyed by a strong tip-surface interaction.

In this study *in situ* AFM experiments were performed with beam-reflection contact 5500 AFM system including AFM-head (N9411A), multi-purpose scanner (N9520, A or B type), and an electrochemical cell purchased from Keysight Technologies. The photographs of the AFM head and scanner are presented in fig. 3.2.4. Three stepping motors (2) are mounted on the base plate (1). The coarse approach is done with three precision micrometer screws (3) driven by the motors via worm-gears (4). The electrochemical cell is mounted on the temperature sample plate (5). The temperature sample plate allows to perform the measurements in a variety of temperature ranges from an ambient temperature to 250 °C. The temperature plate with the electrochemical cell is fixed with thee magnetic posts to the hemispherical heads of the micrometer screws (3), which move the plate up and down during the experiment.

Micrometer adjustment screws (6) enable a manual (x/y)-positioning of the sample plate. The photodiode detector (7) is placed in the scanner (8), when the scanner is on the microscope. The AFM head and scanner are placed on the microscope stand (9) for better stability. This AFM can be combined with video system located above the scanner. The video system allows to pinpoint the regions of interest during measurement and to align the laser on the cantilever tip through a small glass window (10) on the top of the scanner (8).

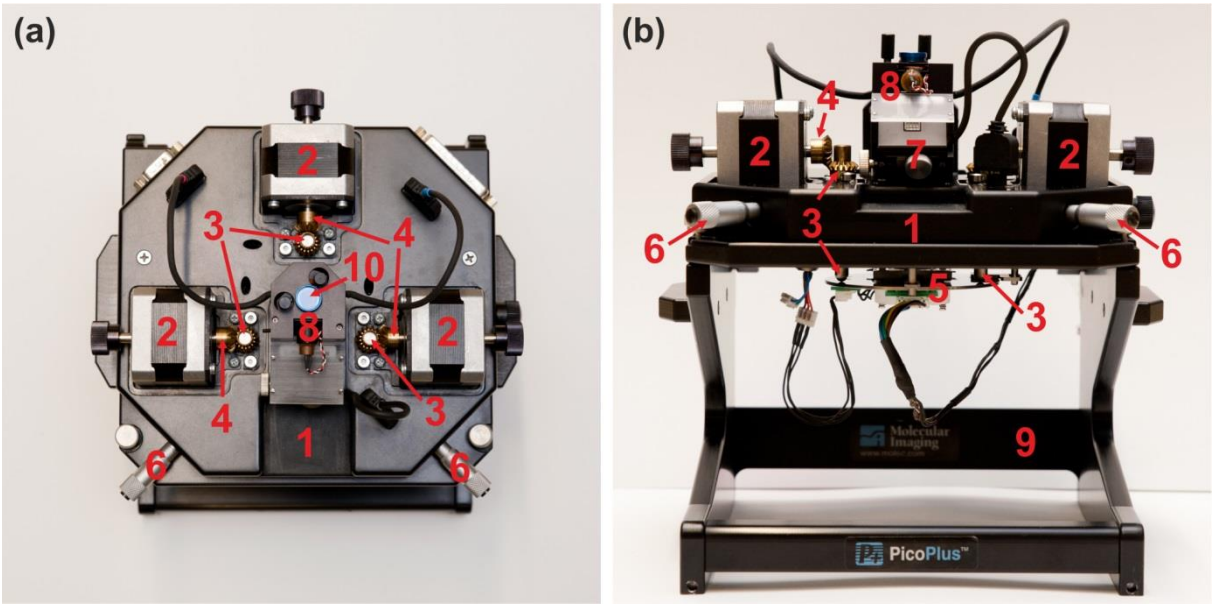

Fig. 3.2.4 *Photographs of the 5500 AFM (Keysight Technologies) head and scanner in (a) top view and (b) front view. 1 - base plate, 2 - step motor, 3 - micrometer screw, 4 - worm gear, 5 - temperature plate with electrochemical cell, 6 - (x/y) adjustment screw, 7 - photodetector, 8 - scanner, 9 - microscope stand.*

The AFM-scanner contains the piezo elements (inside of the scanner, not shown here), removable chemical resistant (polyether ether ketone (PEEK) material) nose cone (1) fixed in the socket of the scanner, mounting (2) for the photodetector (3) and connection cables (fig. 3.2.5). Before the measurement, the cantilever (4) is fixed with a spring clip (5) onto the scanner nose cone (1), which holds the probe at nine degrees from horizontal. The scanner is multi-purpose, as various noses can be installed into the scanner for different imaging modes or environments. The four quadrants photodiode detector (3) has two thumbwheels (6) that allows alignment of the laser spot in both directions.

The AFM experiments were performed inside an argon-filled glove box with water and oxygen contents below 2 ppm (OMNI-LAB from Vacuum-Atmospheres) in an air-conditioned laboratory with a constant temperature of 21 ± 1 °C. The measurements were carried out by using head electronics box (HEB) and controller (N9610A) (from

Keysight Technologies) controlled by PicoView software including CameraView and PicoImage softwares for video output and images manipulation, respectively. Gold-coated silicon SPM-probes from Nano World or Asylum Research with various spring constants were employed for the AFM-measurements. The spring constant was measured for each probe with Cypher S AFM (purchased from Oxford Instruments) using thermal noise method and automatically calculated by IgorPro prior to use. In the case of electroless deposition of GaSb, Cypher S AFM was used to observe the galvanic displacement process in real-time. Furthermore, the appearance of the p-Si(111) surface in ILs was investigated with Cypher S AFM.

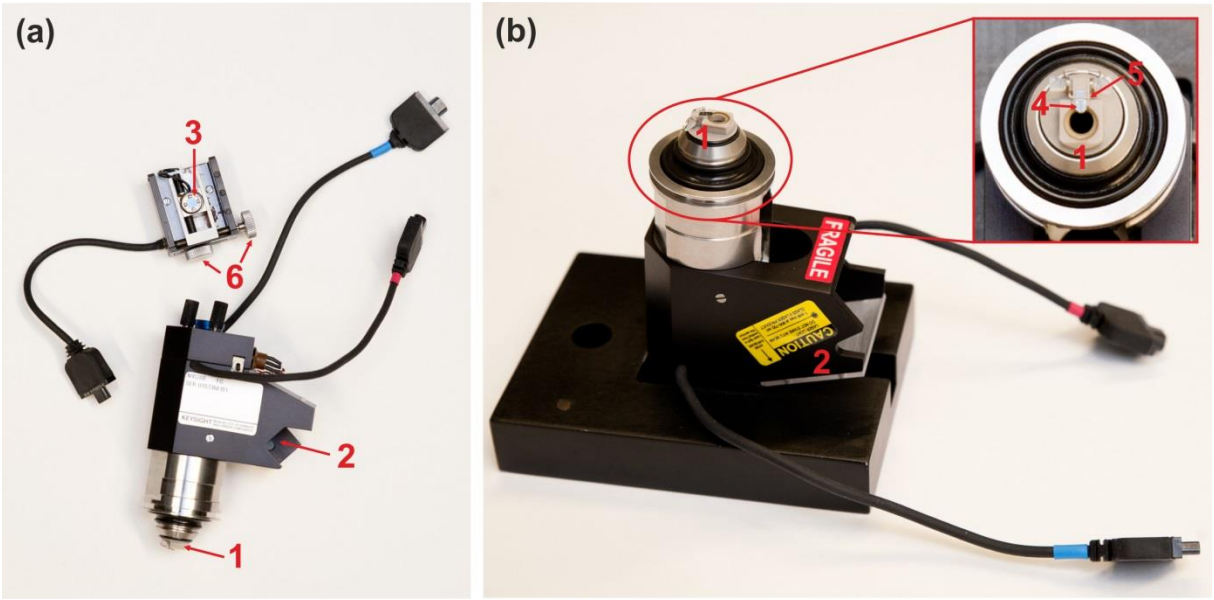

Fig. 3.2.5 *(a, b) Photographs of the AFM (Keysight Technologies) scanner and photodetector. Inset in (b) shows the photograph of the scanner nose.*

The electrochemical cell (Keysight Technologies) consists of polychlorotrifluoroethylene (PCTFE) plate (1), O-ring gasket (2) and two retaining clips (3) (fig. 3.2.6). The plate was clamped with the clips over the O-ring onto the substrate, thus yielding a geometric surface area of the working electrode of 1.77 cm^2. The electrochemical cell was assembled on the standard sample plate or on the temperature control sample plate (as shown in fig. 3.2.6), which enables experiments at elevated temperatures (up to 250 °C). All parts of the electrochemical cell in contact with the electrolyte were formerly cleaned in a mixture of 50/50 vol. % H_2SO_4/H_2O_2 followed by refluxing in ultrapurified water prior to use. Au(111) (a 300 nm thick film on mica) substrates purchased from Molecular Imaging were used as working electrodes (WE). Prior to use, the Au(111) substrates were carefully heated in a hydrogen flame to minimize possible surface contaminations as well as possible. Pt-wire and Pt-ring were used as a quasi-reference (RE) and counter (CE) electrodes, respectively. The

Pt-electrodes were cleaned in a hydrogen flame before use to remove organic impurities.

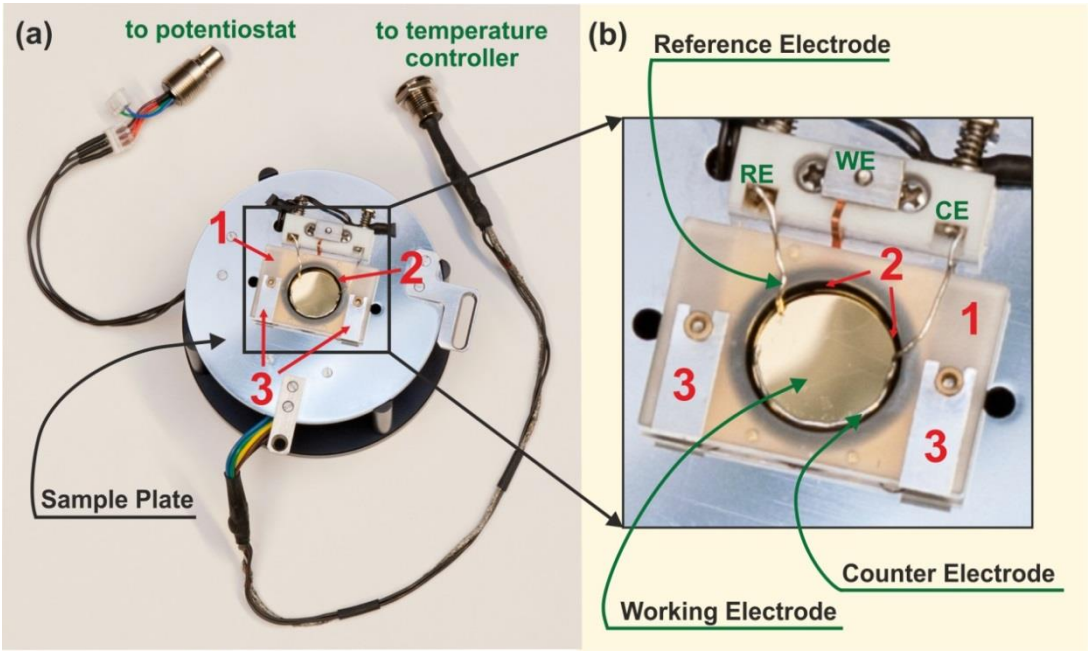

Fig. 3.2.6 *Photographs of the AFM electrochemical cell. The PCTFE plate (1) is clamped with the clips (3) over O-ring (2) onto the working electrode (WE). A Pt-ring and a Pt-wire immersed in the electrolyte serve as counter (CE) and reference (RE) electrodes, respectively.*

The tip-surface interactions in liquids are more complex than in UHV or in air. In general, the tip-surface interactions decrease in liquids, but the interaction of the solvent molecules or ions with the surface causes a short-range order of the liquid at the surfaces (solvation layers), which induces short-range forces (solvation forces) [80]. Charging of the surface can be done by ionization or dissociation of surface groups and adsorption of ions from the solution. The surface charge should be compensated by a formation of the layer of counter ions at the surface (EDL), which may interact with the surface and other layers as well. These electrostatic interactions in liquids can complicate the interpretation of the total force. Furthermore, an EDL also exists at the tip/liquid interface. If the tip and the surface are made of the same material, the repulsive interaction force of EDLs prevents achieving a high resolution images with force microscopy [81]. In the case of ionic liquids, the structure of IL/solid interface is more complex than in aqueous solutions [54, 82]. Electrostatic interactions are strong in ILs. Furthermore, forces based on change of entropy should also be considered, as a large number of energetically similar states is possible in ILs. Various experimental and theoretical studies show the existence of a multi-layered short range nanostructure in ILs and ILs are more structured at highly charged surfaces than at neutral ones [54, 82]. The short range nanostructure regime usually extends

between 1 and 4 nm away from the surface and is strongly dependent on the structure of IL, surface charge and presence or absence of solutes. However, recent studies reveal that in the case of highly charged surfaces both short range (near-surface) and long range surface forces can be obtained in some pure ILs [83]. In this case, the short range nanostructure regime, where surface effects are dominant, extends up to 3 nm away from the surface. The long range regime occurs after the short range structure and might then extend to the distances of greater than 10 nm. In the long range regime, the decay length is dominated by the bulk molecular properties of the used IL [83].

In this work force-distance spectroscopy was applied to reveal the short range nanostructure of the polarized IL/solid interfaces in the pure ILs and in the presence of various solutes. Force-distance curves were collected using the above described 5500 SPM (Keysight Technologies) system in contact mode. The mechanism of operation is presented in Chapter 3.2.3.

3.2.3 Force-Distance Spectroscopy

Force-distance spectroscopy is used to determine the dependence of the tip-surface interaction on the distance between the tip and the surface at a particular location on the sample surface. In this case, the vertical force, which the tip applies to the surface, is measured in the contact mode as a function of the tip-surface separation. This technique can be used to reveal local variations in chemical and mechanical properties of the surface, e.g. adhesion, elasticity, lubrication thickness, etc. Furthermore, force-distance spectroscopy can be applied to evaluate the thickness of adsorbed molecular or ion layers. In this study force-distance spectroscopy was employed to obtain the information on the structure of the polarized IL/solid interface both in the pure ILs (Chapter 5) and in the presence of solutes (Chapter 6).

In AFM force-distance spectroscopy measurement, the cantilever moves toward the sample surface (approach regime) until the contact is reached and then retracted (retract regime), while the deflection of the cantilever vs. an extension of the piezoelectric scanner (piezo movement) is measured. This means that the distance recorded during the measurement (*z*) corresponds to the distance between surface and an equilibrium position of the cantilever (fig. 3.2.7) and has to be converted to an actual position of the tip over the sample surface. The real tip-sample distance (*d*) can be calculated from

$$d = z - (\delta_c + \delta_s) \tag{3.24}$$

where, δ_c and δ_s are distances due to the cantilever deflection and sample deformation, respectively [84].

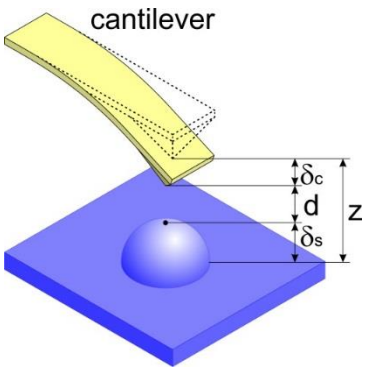

Fig. 3.2.7 *The cantilever bending in the AFM force spectroscopy experiment.*

The cantilever deflection is transformed to a normal force via Hooke's Law (equation (3.23)), using the cantilever spring constant. Fig. 3.2.8 shows a sketch of the tip movement during force-distance spectroscopy measurement in vacuum (simplest case) and the corresponding deflection-distance curve [85]. When the cantilever is far from the surface (A), the deflection of the cantilever is zero as the forces are too small to induce a measurable deflection. If the tip is brought very close to the surface, it may jump into contact with the surface as the attractive forces overcome the cantilever spring constant (B). When the tip is further moved towards the surface, the cantilever starts to bend up (C), as the forces become repulsive and its deflection linearly increases (D) due to increase in repulsive forces. When the cantilever is retracted from the surface (reversed direction), the cantilever bends down (E) as the tip gets stuck on the surface due to adhesion. At some distance, the force applied to the cantilever overcomes the tip-sample adhesion and the tip gets free (F, jump-off contact).

However, fig. 3.2.8 represents the simplest case. Force-distance curves measured in liquid-solid systems are usually quite complex and specific for each system. The situation becomes even more complicated, if ILs are studied. ILs exhibit a remarkably diverse interfacial chemistry with multiple interfacial layers present at the IL/solid interface (Chapter 4). In this case, as the AFM cantilever moves towards the surface, it can even be deflected away due to the forces imparted by the interfacial IL layers.

The mechanism of operation of the AFM force-distance spectroscopy experiment in IL is presented schematically in fig. 3.2.9 [76]. The solid substrate and the AFM tip and cantilever are completely immersed in IL (fig. 3.2.9a). The layers close to the surface are shown schematically as single (blue) layers.

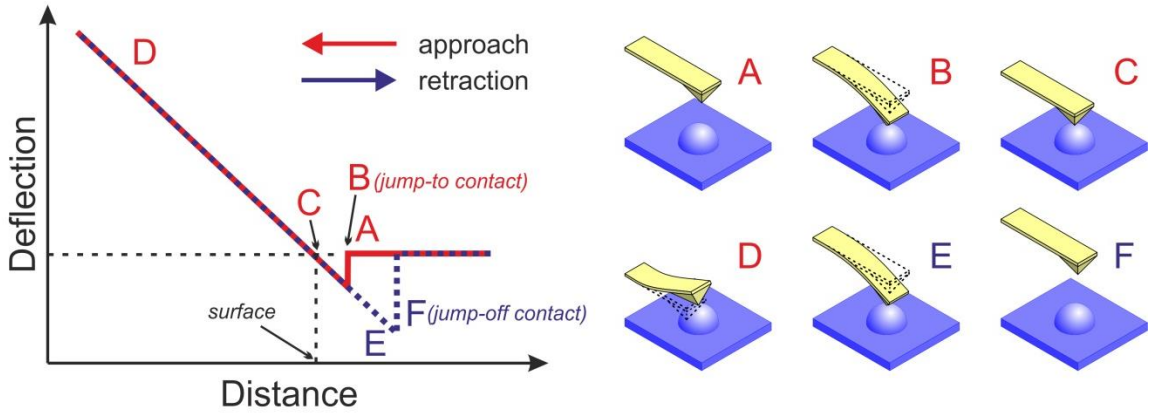

Fig. 3.2.8 *Sketch of the deflection-distance curve at the solid surface in vacuum. Initially, the tip is far away from the surface and the deflection is zero (A). At B, the tip jumps into contact with the surface and the deflection linearly increases after the contact (C, D). On the reverse process the cantilever bends down, as the tip gets stuck with the surface (E) and at some distance the tip becomes free (F).*

As the tip moves towards the surface, it encounters the first layer and the force experienced increases as the tip pushes against this layer until sufficient force is reached to rupture the layer (fig. 3.2.9b). The tip then jumps into contact with the next layer and the process is repeated until the tip reaches the innermost layer. The force increases markedly because the structure in the innermost layer is strongest due to attractive interactions between the IL ions and the surface.

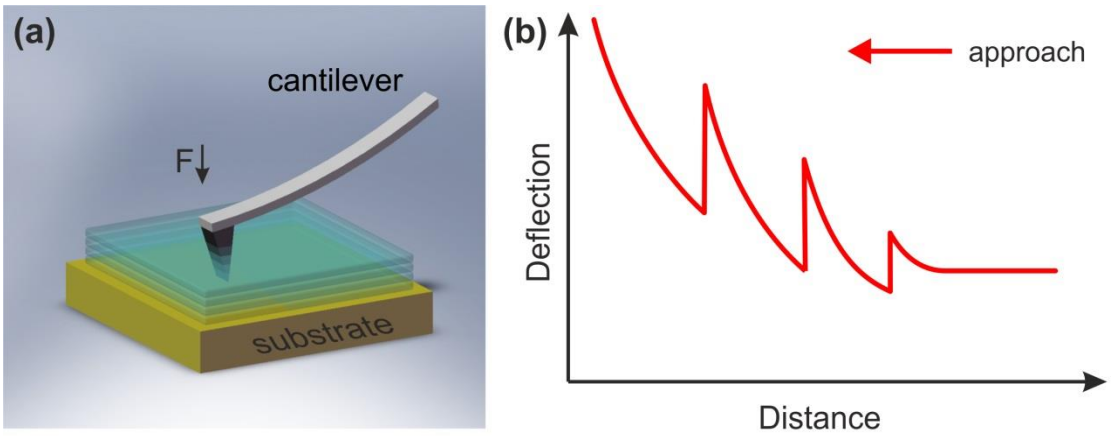

Fig. 3.2.9 *Schematic view of an AFM tip approaching a solid surface in the presence of IL (a) and the corresponding deflection versus distance profile (b). Adopted from ref. [76].*

When the tip pushes through this layer, it comes into contact with either the substrate surface or a layer of ions that are so strongly bound to the substrate that the tip cannot displace it [76]. Thus, the number of peaks corresponds to the number of the well-ordered layers that the AFM tip can distinguish: 3 peaks for 3 ordered layers, 4 peaks for 4 layers, and so on. As it was mentioned above, the obtained deflection vs. distance

(deflection vs. piezo movement) curve (fig. 3.2.9b) should be converted to the force vs. separation (between the tip and the surface) curve. In this case, the positions of the steps (d1, d2 and d3) in the force curve are related to the separation (or spatial distribution) of the layers near the surface (fig. 3.2.10). Zero is the surface itself or the position of the layer of ions, which cannot be ruptured by the AFM tip. The retraction curve can look quite different most likely due to attractive interactions between the tip and the surface or interfacial layers, or fluid dynamic effects.

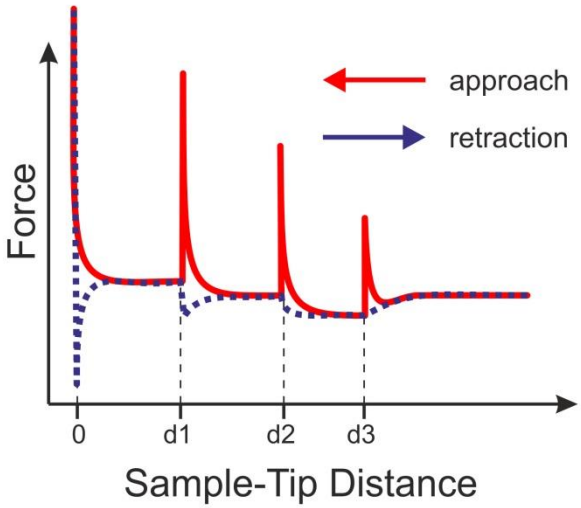

Fig. 3.2.10 *Force vs. distance curve for an AFM tip approaching a solid surface in the presence of IL. Reproduced from ref. [76].*

The principle algorithm of the conversion of deflection vs. distance curves to force vs. separation curves are presented in ref. [86]. In the present study, force spectroscopy curves were obtained with PicoView 1.12 software. The raw data are recorded as potential vs. distance (fig. 3.2.11a), where potential shows the deflection of the cantilever in volts and the distance is the combination of the static displacement and piezo movement. In this case, the deflection in volts (V) can be converted to normal force (F) in each data point i via Hooke's law:

$$F_i = -k\alpha^{-1}V_i \tag{3.25}$$

where, k is the cantilever spring constant and α is the deflection sensitivity - the slope of the repulsive part of the force spectroscopy curve (region C, fig. 3.2.8).

The cantilever-surface distance (x) is converted to tip-surface separation (d) with

$$d_i = \alpha^{-1}V_i - x_i \tag{3.26}$$

After the normalization to "zero" distance and force, the resulting force vs. separation curve (fig. 3.2.11b) is used to analyse the structure of the IL/solid interface.

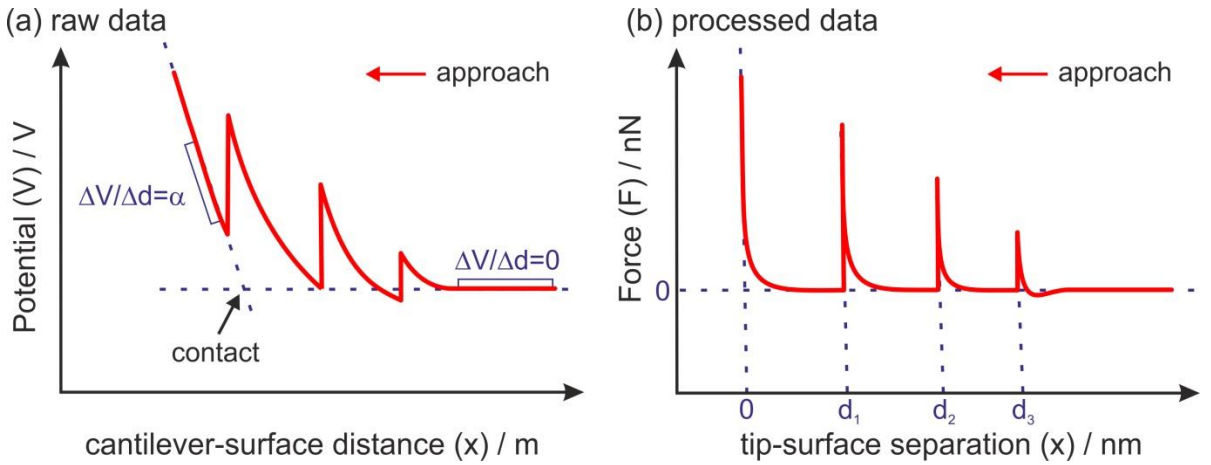

Fig. 3.2.11 *Schematic illustration of the process of conversion of the raw data recorded in AFM force spectroscopy measurement into a standard force vs. separation profile.*

The qualitative analysis of the interfacial nanostructure is only conditionally possible, as AFM cannot determine the composition of the each solvation layer unambiguously. However, the structure of the IL/solid interface can be estimated from the dimension of the ions of the employed IL. Thus, the ion pair diameter (D_{ip}) can be determined from the density (ρ) and molecular weight (M) of the employed IL assuming a cubic packing geometry according to the method described by Horn et al. [87]:

$$D_{ip} = \sqrt[3]{M \cdot \rho^{-1} \cdot N_A^{-1}} \tag{3.27}$$

where N_A is Avogadro constant.

The characteristic dimensions of ions in crystalline phase can be obtained experimentally by means of the specific reflection of the X-ray beam. However, in the case of ILs, the dimensions of ions can be determined with quantum chemistry calculations, e.g. by using density functional theory (DFT) [88].

The width of the solvation layers present at the IL/surface interface can be determined from the position of the steps of the force-distance curve. For example, three steps at d_1, d_2 and d_3 in the force curve presented in fig. 3.2.11b can be seen. The width of these three steps are d_1, (d_2-d_1) and (d_3-d_2), respectively, which correspond to the thickness of three solvation layers present at the IL/solid interface. The correlation of the thickness of each solvation layer with the dimensions of cation and anion and the ion pair diameter may provide information on the composition of each solvation layer and their average orientation. Furthermore, the amount of force required to rupture each solvation layer gives an insight into the strength of the interaction between the layers and the interaction strength of innermost layer with the surface. The polarization of the surface by applying the electrode potential often leads to a reorganization of the

ions in the solvation layers. Therefore, the changes in force profiles that occur with potential may be directly correlated with variation in IL near the surface structure. Moreover, the addition of solutes may also alter the IL/electrode interfacial nanostructure. The molecular diameters of various salt-IL species are often comparable with the dimensions of individual IL ions or IL ion pair and therefore indistinguishable by AFM force spectroscopy. However, by combining this technique with other methods, such as cyclic voltammetry (CV), electrochemical impedance spectroscopy (EIS), electrochemical quartz crystal microbalance (EQCM) measurements, STM, vibrational spectroscopy and theory based calculations, a comprehensive information on the composition of solvation layers at the IL/solid interface and on the organization of ions within the solvation layers can be achieved.

4 Ionic Liquids at Electrified Interfaces

4.1 Structure of the EDL in ILs

Electrode interfaces play a significant role in the performance of IL based devices such as batteries and capacitors, and for electrodeposition from ILs. The arrangement of ions at the IL/electrode interface is defined by the “electrical double layer” (EDL), which describes how the potential changes with the distance from the electrode surface. Understanding the structure of EDL is important for a wide range of applications, which involve reactions at the IL/solid interface (e.g. catalysis, electrochemistry, capacitors, batteries, fuel and solar cells).

During the last decade, the IL/solid interface has been extensively studied both experimentally and theoretically towards understanding the complex structure of the EDL. The distribution of ions at the electrode surface and the double layer capacitance of dilute aqueous electrolyte solutions are usually described by the Gouy-Chapman-Stern (GCS) theory [89-91]. However, the classical GCS theory for aqueous electrolytes is not valid for ILs systems, because solvent-solute and ion-surface interactions are considerably different in ILs compared to aqueous systems. The conventional models reveal that the electrolytes consist of small spherical ions with uniform charge density on their surface, which are dissolved in a large amount of solvent and interact with each other via long-range Coulomb forces. These models are applicable for diluted electrolytes where dissolved salt ions are surrounded by a large number of solvent molecules. In contrast, ILs exhibit a much higher ion charge density compared to aqueous electrolytes. Neat ILs are comprised of only ions (without any molecular solvent), which are generally large and asymmetric in nature and have delocalised charge centers. Therefore, IL ions cannot be modelled as point charges. The ion concentration of charged species at the interface does not differ greatly from the bulk. Furthermore, ILs frequently have well defined self-assembled nanostructures in the bulk and at interfaces which means continuum models are inappropriate. Therefore, the EDL structure of ILs is rather complicated, and leads sometimes to unpredictable capacitance behaviour [92-111]. Consequently, the appearance of capacitance curves for similar IL/electrode systems range from pseudo-parabolic, to “bell-” and “camel-shaped”, which suggests a different IL/electrode interfacial structure. Electrochemical impedance spectroscopy (EIS) measurements reveal the existence of several distinct processes at the IL/electrode interfaces taking place on different time

scales [104-106, 108, 109, 111]. In general, at least two capacitive processes (one on millisecond time scales and one on second time scales) are obtained in the case of IL, due to a double layer charging at the IL/electrode interfaces. However, ultraslow processes can also be detected for IL/electrode interfaces, which seem to be Faradaic or pseudo-capacitive in nature and cannot be unambiguously related to defined processes. Furthermore, the existence of slower processes may lead to hysteresis effects in the capacitance of the fast millisecond process [106].

Recent theoretical studies have progressed towards a fundamental understanding of the structure of EDL in ILs [82, 112-129]. It was shown that the interactions between IL ions and electrode surfaces are strong, mainly due to electrostatic attractions and van der Waals forces. The IL completely screens the charged surfaces within several bound ion layers by electrostatic interactions. Moreover, high ionic densities of ILs results in an overscreening, crowding, and lattice saturation effects as characterized by various capacitance-voltage dependencies [130, 131]. The Bazant-Storey-Kornyshev (BSK) theory is one of the most popular descriptions of these effects in ILs [114]. In the BSK model, an overscreening of ions is predicted if the charge of the innermost (Stern) layer is greater than the potential of the electrode (at low electrode potentials), while crowding of ions and lattice saturation occur if the innermost (Stern) layer is insufficient to neutralize the surface electric potential (at high electrode potentials) [114]. Furthermore, a remarkable progress has been made towards understanding the EDL structure of ILs on flat surfaces and a critical overview is presented in ref. [82]. Later the coupling of density and charge has been described as the ground state for a spin-glass Hamiltonian for nearest neighbour interactions (given their positions) for RTILs [128]. It was shown that the long-range charge oscillations in ILs result from positional ordering, which is strong in the pure ILs and disappears on addition of solvent or increasing the temperature. The recently developed continuum theory [129] further explains the formation of discrete layers of charge at charged surfaces and decaying charge density profile in ILs.

The IL/electrode interface has been explored experimentally using various experimental methods, such as sum-frequency generation spectroscopy [132-135], surface-force apparatus [136-139], X-ray scattering techniques [140-148], X-ray photoelectron spectroscopy (XPS) [149-152], neutron scattering technique [153-159] and scanning probe microscopy [72, 108, 109, 149, 150, 160-184]. Both theoretical and experimental studies of the structure of the EDL in ILs reveal the existence of ion ordering at the IL/solid interface resulting in the formation of a multi-

layered interfacial structure, which is composed of alternating solvation layers enriched in either cations or anions (fig. 4.1).

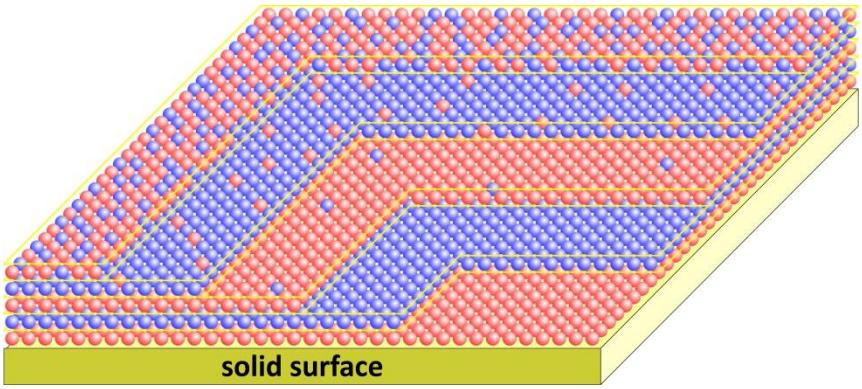

Fig. 4.1 *Schematic representation of the structure of the IL/solid interface. A multi-layered interfacial structure is composed of alternating solvation layers enriched in either anions (red) or cations (blue).*

AFM has been used to probe the normal structure of IL ions at a wide variety of solid interfaces (including electrode interfaces) [108, 109, 163-175, 184-188]. AFM results reveal that the multiple layered structure at the IL/solid interface is composed of the innermost (Stern) layer (a well-ordered single layer of ions in direct contact with the solid surface), that templates the surface-induced ordering in the subsequent layers, which can extend up to several nanometers in the solution [171, 189]. X-ray reflectivity measurements have confirmed this interpretation [146, 147]. Furthermore, AFM results have shown that the adsorption of the ILs on solid surfaces is at least an order of magnitude stronger than the adsorption known for water or organic solvents and that the strength of the interaction is dependent on the cation and the anion [109, 171, 173, 174, 190, 191]. The Stern layer is the most organised one. Applying a potential induces a reordering of the Stern layer structure to compensate the interfacial charge. At negative potentials the Stern layer is enriched in cations, while at positive potentials the innermost layer is anions rich [121, 163, 171, 175, 192]. These results are supported by surface specific sum frequency spectroscopy [132-134] as well as with X-rays [148, 193] and neutron scattering [157, 158].

Based on both experimental and theoretical results, it was concluded that the EDL formed by ILs at solid surfaces is short-ranged with the pronounced charge density oscillation profile. However, in 2013 electrochemical surface force apparatus (SFA) measurements between two charged surfaces (gold and mica) separated by [BMIm]TFSA revealed the existence of attractive forces at distances of up to 35 nm, which were significantly greater than expected [194]. Later, a long-range repulsive force was obtained using SFA between two mica substrates in ILs [137]. These long

range interaction forces were attributed to electrostatic forces and the authors assumed that ILs can behave as diluted electrolyte solutions. Although this conclusion was in contradictory with the generally accepted understanding of EDL formed by ILs, the long-range repulsive forces have since been measured in several research groups [136, 195, 196]. In 2017 it has been reported that both short range (near-surface) and long range surface forces can be obtained in some pure ILs at highly charged surfaces [83]. The short range nanostructure regime, where surface effects are dominant, extends up to 3 nm away from the surface, while the long range regime occurs after the short range structure and might then extend to the distances of greater than 10 nm. In the long range regime, the decay length is dominated by the bulk molecular properties of the used IL [83]. Recently, the structure of the electrified Au(111) / polymeric IL-IL mixture interface was investigated using AFM [184]. It was found that a polymeric cation-enriched boundary layer is formed on Au(111). At negative electrode potentials the polymeric cation chains are compressed due to electrical attractions with the surface, while at positive electrode potentials they are fully stretched due to electrical repulsions, which leads to stronger adsorption at more negative electrode potentials [184].

Over the last 20 year, *in situ* STM has been extensively used to investigate the EDL of ILs laterally at metal and semiconducting surfaces both in the pure IL and in the presence of various solutes [109, 111, 166, 167, 173, 178-180, 183, 191, 197-209]. It was obtained that ILs can induce structural changes in the electrode surface itself due to ion adsorption in the interfacial layer, which is dependent on the electrode potential. At cathodic potentials, the kinetically hindered formation of the herringbone reconstruction, Au(111)(22 x $\sqrt{3}$), has been imaged for a single-crystalline Au(111) surface in contact with neat [BMIm]BF_4 [199], [BMIm]PF_6 [200], 1-butyl-1-methyl-pyrrolidinium bis(trifluoromethylsulfonyl)amide ([$Py_{1,4}$]TFSA) [173], 1-butyl-1-methylpyrrolidinium tris(pentafluoroethyl)trifluorophosphate ([$Py_{1,4}$]FAP) [109], N-propyl-N-methylpiperidinium bis(trifluoromethylsulfonyl)amide ([PMPi]TFSA) [183] and 1-butyl-1-methylpyrrolidinium dicyanamide ([$Py_{1,4}$]DCA) [180]. At the open circuit potential (OCP), the Au(111) surface exhibits a worm-like structure pattern in [$Py_{1,4}$]TFSA [201, 210], 1-hexyl-3-methylimidazolium tris(pentafluoroethyl)-trifluorophosphate ([HMIm]FAP) [191] and [$Py_{1,4}$]FAP containing TaF_5 [167]. Su et al. [202] have reported that in the case of alkylimidazolium ILs ([EMIm]$^+$, [PMIm]$^+$, [BMIm]$^+$ and [OMIm]$^+$), the cation adsorption at negative electrode potentials leads to the formation of an ordered micelle-like structure on the Au(100) surface and irregular worm-like structure on Au(111). It was suggested that both structures are composed

of double-rows arising from counter-facing imidazolium cation pairs. The width of the micelle-like structure is dependent on the side chain length of the cation and constrained by the periodicity along the √2 direction of the Au(100) surface, while the anion of an IL (BF_4^-, PF_6^-, TfO^- and $TFSA^-$) does not influence the formation of micelle-like structures [202]. The authors proposed that this structure is stabilized by strong van der Waals interactions between the alkyl side chains of the adsorbed IL cations. At more negative electrode potentials a formation of Au(100)-hex reconstruction occurs [203]. The formation of $[PF_6]^-$ anion adsorption layers showing a potential-dependent 2D phase transition from a Moiré-like structure to a (√3 x √3) phase has been observed for [BMIm]PF_6 at Au(111) by Pan and Freyland [200]. Gnahm et al. [111, 204] have performed similar *in situ* STM investigations of gold single crystal electrodes and ILs with imidazolium ions and either $[PF_6]^-$ or $[BF_4]^-$ anions. Recent combined *in situ* STM and AFM studies revealed that the interaction between [EMIm]TFSA and the Au(111) surface is much stronger than that between 1-ethyl-2,3-dimethylimidazolium bis(trifluoromethylsulfonyl)amide ([EMMIm]TFSA) and the Au(111) surface [179]. At negative electrode potentials, the formation of the hex-reconstruction on Au(100) and herringbone reconstruction on Au(111) was obtained in hexaalkylguanidinium ILs [205]. The reconstruction of the Au(111) and Au(100) surfaces and surface etching have been reported at positive and negative potential region of the potential of zero total charge (pztc) values in [HMIm]FAP [206]. Ordered adlayers of cations and anions have been imaged by *in situ* STM on Au(100) in [BMIm]TFSA [183, 207]. At electrode potentials more negative than pztc the structuring of cations was observed on Au(100) (micelle-like structure) and Ag(100) (patchwork-like structure) in [BMIm]PF_6, while no such ordering was probed on Pt(100) and HOPG [183]. The ordered interfacial nanostructure was obtained on Au(100) in [PMPi]TFSA [183]. Ueda et al. [182] have reported the specific adsorption of 1-butyl-3-methylimidazolium iodide ([BMIm]I) on Au(111). The authors showed the formation of highly ordered I adatoms composed of c(p x √3) structures and characteristic nanostructured rings consisting of $[BMIm]^+$ cations on Au(111) using *in situ* STM. Recently the influence of both the cation and the anion of IL on the stability of the Au(111) surface was investigated in $[Py_{1,4}]$DCA, $[Py_{1,4}]$TFSA, 1-ethyl-3-methyl imidazolium dicyanamide ([EMIm]DCA) and 1-ethyl-3-methylimidazolium acetate ([EMIm]OAc) [178]. It was found that the appearance of the Au(111) surface depends on the applied electrode potential and is different in various ILs. The authors reported that the anions have a significant effect on the gold etching at negative electrode potentials, whereas cations alter the gold etching rather at positive electrode potentials.

Furthermore, the Au(111) surface was found to be stable in all ILs at high negative electrode potentials [178]. In situ STM studies also revealed that the addition of various solutes can significantly alter the IL/electrode interface [167, 197, 198, 209].

In 2014, different superstructures have been probed on HOPG using *in situ* STM at negative electrode potentials [166]. The lateral size of these structures suggests that cations and anions form ordered layers before the liquid is decomposed at the cathodic limit. Müller et al. [208] reported that at the negative electrode potentials the HOPG surface is stable in [BMIm]PF_6, whereas the Au(100) surface is subject to restructuring in this IL. Nevertheless, *in situ* STM revealed that at negative potentials an ordered structure is obtained on the HOPG surface, which exhibits a larger lattice constant than that of HOPG, while at positive potentials the formation of islands occurs.

In 2015, *in situ* high-speed (video) STM was applied to investigate the molecular arrangement and surface dynamic of Au(111) in [$Py_{1,4}$]TFSA, 1-hexyl-3-methylimidazolium chloride ([HMIm]Cl) and 1-hexyl-3-methylimidazolium bis(trifluoromethylsulfonyl)amide ([HMIm]TFSA) at negative potential regime [72, 73]. In all three ILs, a potential dependent sprite-like arrangement of the adsorbed cations was obtained. In the case of [$Py_{1,4}$]TFSA, at electrode potentials between -1.0 V and -1.6 V cations adsorb in a rectangular unit cell leading to the formation of rows on the gold surface [72]. These rows cannot be probed at electrode potentials higher than -1.0 V due to a high mobility of cations. Since the dimensions of the unit cell change by reducing the electrode potential, it was suggested that at -1.4 V, the cation alkyl chain lies flat on the surface, whereas at -1.6 V it adopts an upright conformation. The sprite-like structures obtained in [HMIm]TFSA on the Au(111) surface were similar to those observed in [$Py_{1,4}$]TFSA, but differ from the structure probed in [HMIm]Cl, which reveals that in-plane arrangement of the cations is affected by co-adsorbed anions [73].

The IL ions adsorbed onto the surface participate in the tunneling process, and the STM tip must move through these adsorbed layers during the scanning process. In this case the STM tip either pushes away the layers that are not strongly adsorbed or images them, which decreases the image resolution compared to what is possible in conventional electrolytes [108]. To overcome this, STM experiments are sometimes completed using frozen monolayers under UHV, which enables the position of ions to be obtained [149, 150, 161, 211-215]. The disadvantage of this approach is that the structure determined might not reflect the ion arrangements at a bulk interface as in a

monolayer the numbers of cations is fixed at 1:1 and the ions in the layer contact the solid surface and a vacuum rather than the surface and the bulk liquid.

Recently UHV-based AFM was applied to study the growth behavior of 1,3-dimethylimidazolium bis(trifluoromethylsulfonyl)amide ([MMIm]TFSA) on Au(111) [160, 177, 181]. The defined amounts of [MMIm]TFSA were deposited on Au(111) at different temperatures to study the morphology and wetting behavior of deposited films. A combined STM and AFM study of the nanoscale arrangement within the first layer of [MMIm]TFSA on Au(111) revealed that [MMIm]TFSA shows a well-ordered hexagonal pattern of circular protrusions due to the small size and high symmetry of the cation [160]. At room temperature a well-known checkerboard structure of anions and cations adsorbed next to each other was obtained. Quite recently, a UHV AFM study of the time- and temperature-dependent growth of [MMIm]TFSA on Au(111) demonstrated that a stable 2D bilayer structure is obtained if the IL's film was deposited below 170 K and slowly annealed to room temperature. Upon deposition at room temperature the formation of 2-30 nm high and 50-500 nm wide metastable 3D droplets on top of a checkerboard-type wetting layer, which with time spread out into stable 2D bilayers, was probed [181].

During the recent about 5 years, *in situ* amplitude-modulated atomic force microscopy (AM-AFM) has been used to reveal the near surface structure of ILs at solid interfaces with molecular resolution both in pure ILs and in the presence of various metal salts [169, 216-219]. Elbourne et al. [216] reported that the IL/mica interfacial nanostructure is strongly influenced by the registry between the cations and the mica surface charge sites, while near surface nanostructure is sensitive to both cation and anion structure. Five protic ILs (ethylammonium nitrate (EAN), propylammonium nitrate (PAN), ethanolammonium nitrate (EtAN), ethylammonium formate (EAF) and dimethylethylammonium formate (DMEAF)) were examined. A comparative AM-AFM study between the protic (EAN) and aprotic ([EMIm]TFSA) ILs reveal that the strength of bulk liquid morphology can also affect the lateral organization of the IL at the surface [217]. In the case of EAN, worm-like structures are present at the mica surface, whereas $[EMIm]^+$ adsorbs in a more isolated fashion, but still in rows templated by the mica surface. The addition of metal salts can significantly alter the IL/mica interfacial nanostructure [219]. Lithium, sodium, potassium magnesium, calcium and aluminum nitrate salts were added to PAN for the study. It was found that the metal ions compete with the IL cation and adsorb to negatively charged sites on the mica surface nanostructure [219]. These AM-AFM measurements reveal that the

nanostructure of PAN/graphite interface is determined by the cation [218]. It was obtained that the structure is highly ordered with a well-defined rhomboidal symmetry, which is produced by relatively immobile surface-adsorbed propylammonium cations. In 2015, the Stern layer nanostructure of the [EMIm]TFSA/HOPG interface was investigated with *in situ* AM-AFM in the presence and absence of lithium bis(trifluoromethylsulfonyl)amide (LiTFSA) or [EMIm]Cl [169]. The authors have reported that well-defined rows formed by anion-cation-cation-anion unit cell are present on the surface for pure [EMIm]TFSA at the OCP. Changing of the electrode potential induces a rearrangement of the IL ions in the Stern layer. Furthermore, the addition of Li^+ or Cl^- ions significantly alters the IL/HOPG interface resulting in various surface structures at different electrode potentials [169].

It can be summarized that the interfacial structure of ILs on metal electrodes is complex and differs depending on the IL chemical structure, applied electrode potential and presence of solutes. The solvation layers play an important role in electrochemical processes [220]. Changing of the surface potential (e.g. by applying a potential), and the addition of co-solvents and salts (e.g. for electrodeposition) can lead to a reordering of the interfacial layer structure that, in turn, may significantly alter electrode reactions. As the IL/electrode interface is influenced by even low (ppm regime) amounts of impurities, only ILs of the highest available quality should be employed for such measurements to reduce the risk of misinterpretations.

4.2 Role of the EDL of ILs in Electrochemical Processes

Recently, ILs have attracted significant interest for various electrochemical applications, e.g. as electrolytes for electrodeposition of metals and semiconductors [29]. It was found that the structure of the IL/electrode interface plays a significant role in the electrodeposition processes influencing the morphology and the properties of the electrodeposits [162, 167, 221-226]. Under similar experimental conditions, the Al and Zn deposits obtained electrochemically in $[Py_{1,4}]$TFSA and 1-butyl-1-methylpyrrolidinium trifluoromethylsulfonate ($[Py_{1,4}]$TfO) were nanocrystalline, whereas the electrodeposition of Al and Zn in [EMIm]TFSA and 1-ethyl-3-methylimidazolium trifluoromethylsulfonate ([EMIm]TfO) led to microcrystalline deposits [221-223]. *In situ* STM and AFM measurements revealed that in the neat ionic liquids $[Py_{1,4}]^+$ cations interact more strongly with the substrate than $[EMIm]^+$ cations [173]. Therefore, it was suggested that the $[Py_{1,4}]^+$ acts as a grain refiner by adsorbing to the substrates and to the growing nuclei, thus hindering the

crystal growth leading to the formation of nanocrystalline Al and Zn electrodeposits. The influence of the imidazolium cation structure on the electrodeposition of Zn was investigated from zinc trifluoromethylsulfonate ($Zn(TfO)_2$) in ILs with $[TfO]^-$ anion and three different cations, namely $[EMIm]^+$, 1-methylimidazolium ($[MIm]^+$) and 1-ethyl-2,3-dimethylimidazolium ($[EMMIm]^+$) [224]. Raman spectroscopy revealed that the addition of $Zn(TfO)_2$ to [MIm]TfO, [EMIm]TfO and [EMMIm]TfO leads to the formation of $[Zn(TfO_3)]^-$, $[Zn(TfO_4)]^{2-}$, $[Zn(TfO_5)]^{3-}$ complexes, respectively. The differences in the zinc species present in the electrolytes have a strong influence on the morphology of the electrodeposits. Zn deposits with a cubic morphology and particle sizes of about 10 μm were obtained in [MIm]TfO at 120 °C, while hexagonal structured Zn with particle sizes of about 5 μm was achieved in [EMIm]TfO. In the case of [EMMIm]TfO, cauliflower-like agglomerates with particle sizes of several hundred nanometers were formed. Furthermore, it was found that the addition of water significantly alters the deposition process and the morphology of the electrodeposited Zn [224]. Recently, the effect of anions on the IL/solid interface and the electrodeposition of Zn were investigated in ILs composed of $[EMIm]^+$ cation and four various anions, namely TfO^-, $TFSA^-$, methylsulfonate (OMs^-) and acetate (OAc^-), which contain $Zn(TfO)_2$, $Zn(TFSA)_2$, $Zn(OMs)_2$, $Zn(OAc)_2$, respectively [162]. Dense Zn deposits with nanowire-like and hexagonal-like structures were obtained in [EMIm]TFSA and [EMIm]TfO, respectively, while thin Zn films with porous and spongy-like structures were found in [EMIm]OMs. In the case of [EMIm]OAc, Zn deposits were not obtained under similar conditions. Raman spectroscopy revealed that the speciation of Zn^{2+} ions is different in these ILs. The influence of the cation of ILs was also observed in the case of Si electrodeposition. Fine spherical Si particles were obtained from $SiCl_4$ in $[Py_{1,4}]$TFSA, while a porous Si deposit was achieved in $[Py_{1,4}]$FAP containing $SiCl_4$ [225]. IR spectroscopy analysis revealed that $SiCl_4$ interacts differently with ILs leading to the formation of different silicon electroactive species. Furthermore, it was reported that both the cation and the anion of the IL can alter the morphology of electrodeposited Sn [226]. Agglomerated Sn deposits were obtained in $[Py_{1,4}]$TfO containing $SnCl_2$, while dendrites were achieved in both [EMIm]DCA and $[Py_{1,4}]$DCA. Infrared (IR) spectra indicated that different complexes are formed in different ILs containing $SnCl_2$. Moreover, it was found that TaF_5 can be reduced to elemental Ta in $[Py_{1,4}]$TFSA, while in $[Py_{1,4}]$FAP the electroreduction processes were practically inhibited, as the presence of TaF_5 could not alter the interfacial nanostructure like in the former case [167]. The composition of electrodeposited Si_xGe_{1-x} depends on the

IL [220, 227]. Furthermore, the choice of the IL cation affects the optical properties of electrochemically made GaSb [228].

These results show that differences in electroactive species can influence the IL/solid interfacial nanostructure, which alters the deposition process and morphology of the resulting electrodeposits [229]. Therefore, understanding the structure and properties of the IL/solid interface in the presence of metal salts is critical to understand electrochemical processes and to produce coatings with a defined morphology. The influence of the IL/electrode interfacial nanostructure on various electrodeposition processes and on the morphology and properties of the resulting deposits will be discussed in Chapter 7.

5 Nanostructure of the IL / Electrode Interface

The content of this section was partly published in ref. [109, 171, 173, 191, 230] and summarized in ref. [75, 76]. In this thesis the key results are presented and discussed.

The part of this work was financially supported by the Deutsche Forschungsgemeinschaft (DFG) within Priority Program SPP 1191-Ionic Liquids (grant number: EN 370/14-1).

5.1 IL / Au(111) Interface

The Au(111) surface is one of the most popular atomically flat single-crystal surfaces studied with scanning probe microscopy. The Au(111) surface is characterized by a hexagonal arrangement of atoms with a herringbone reconstruction, which is sensitive to the local and overall surface stress variations. In 2006 it was found that at the OCP instead of a flat Au(111) surface with terraces, the gold surface exhibits a worm-like pattern in $[Py_{1,4}]$TFSA [201]. Furthermore, *in situ* STM revealed that at more negative electrode potentials a restructuring of the gold surface is obtained leading to the formation of the herringbone (22 x $\sqrt{3}$) reconstruction. The CV of the $[Py_{1,4}]$TFSA on Au(111) revealed the existence of several reduction processes in the cathodic regime prior to the irreversible reduction of the organic cation, which were considered to be correlated with the restructuring/reconstruction of the gold surface. These interesting observations have raised the question why the Au(111) surface is subject to restructuring upon changing the electrode potential in the pure IL. Subsequent combined *in situ* STM and AFM studies showed that at similar experimental conditions the lateral nanostructure of the IL/Au(111) interface is different in various ILs [109, 171, 173, 191, 230]. Thus the appearance of the Au(111) surface and the structure of the IL/Au(111) interface are IL-dependent. In this chapter the key results described in ref. [75, 76] are replicated and supplemented.

In general, both the cation and the anion of the IL can significantly alter the IL/electrode interfacial nanostructure, and even minor modifications in the IL composition can lead to a complete restructuring of the IL/electrode interface. The strong influence of the cation on the IL/electrode interfacial nanostructure can be clearly seen from *in situ* STM and AFM results obtained for ILs with the tris(pentafluoroethyl)trifluorophosphate (FAP^-) anion and 3 different cations, namely 1-butyl-1-methylpyrrolidinium ($[Py_{1,4}]^+$), 1-ethyl-3-methylimidazolium ($[EMIm]^+$) and 1-hexyl-3-methylimidazolium ($[HMIm]^+$) [109, 191, 230]. All these ILs exhibit wide electrochemical windows of more

than 5 V. *In situ* STM images show that the appearance of the Au(111) surface differs for each IL (fig. 5.1.1). In the case of $[Py_{1,4}]$FAP, the Au(111) surface is subjected to a restructuring / reconstruction [109]. At the open circuit potential (OCP) (-0.2 V vs. Pt) the typical terraces like Au(111) surface with a step height of 250 pm is obtained (fig. 5.1.1a). However, in the cathodic regime the Au(111) surface undergoes a (22 x √3) surface reconstruction leading to a herringbone superstructure (fig. 5.1.1b). The surface layer reduces its energy by formation of stacking structures on the surface, in which the atoms occupy fcc and hexagonal closed-packed (hcp) sites. Since the fcc structure is energetically more favourable than the hcp structure, the width of the hcp stacking is smaller. Furthermore, the Au(111) surface exhibits local structures, such as U-connections (neighbouring herringbone rings) and elbows (a corner made by rotation of the herringbone ridge) in $[Py_{1,4}]$FAP, which can be clearly identified with *in situ* STM [109]. The distance between the herringbone rims is about 6.0 ± 0.5 nm, which is in good agreement with the value of 6.3 nm expected for the (22 x √3) reconstruction. The herringbone superstructure pattern was stable in the potential range between ca. -0.6 V and -1.7 V. However, further reducing of the electrode potential leads to a surface restructuring resulting in the formation of a terraces like surface at -2.0 V (fig. 5.1.1c).

For [EMIm]FAP, the Au(111) surface probed at the OCP (-0.2 V vs. Pt) is unclear due to a thin “layer” present on the surface (fig. 5.1.1d). The roughness of this “layer” increases at more negative electrode potentials and at -1.0 V this layer can be clearly seen on the gold surface (fig. 5.1.1e) [230]. As in the present study the highest available quality of the ILs is used, the probed surface is the result of the interaction of the IL with the gold surface and not due to IL impurities. The layer becomes more visible and its structure changes by further reducing the electrode potential (fig. 5.1.1f). Interestingly, it was found that at electrode potentials more positive than OCP the Au(111) surface appearance changes significantly [230]. *In situ* STM revealed the formation of islands, followed by a layer and “dissolution” of that layer at +0.7 V.

In the case of [HMIm]FAP at OCP (-0.1 V vs. Pt) the Au(111) surface shows a worm-like surface structure with ~ 0.3 nm deep vacancies (Figure 5.1.1g) [191]. If the electrode potential is reduced to -1.0 V, islands of 0.2 - 0.4 nm in height are observed (fig. 5.1.1h). At -2.0 V these islands transform to wider islands with heights between 0.4 nm and 0.6 nm (fig.5.1.1i). Interestingly, at an anodic polarization the adsorbed layer is differently structured.

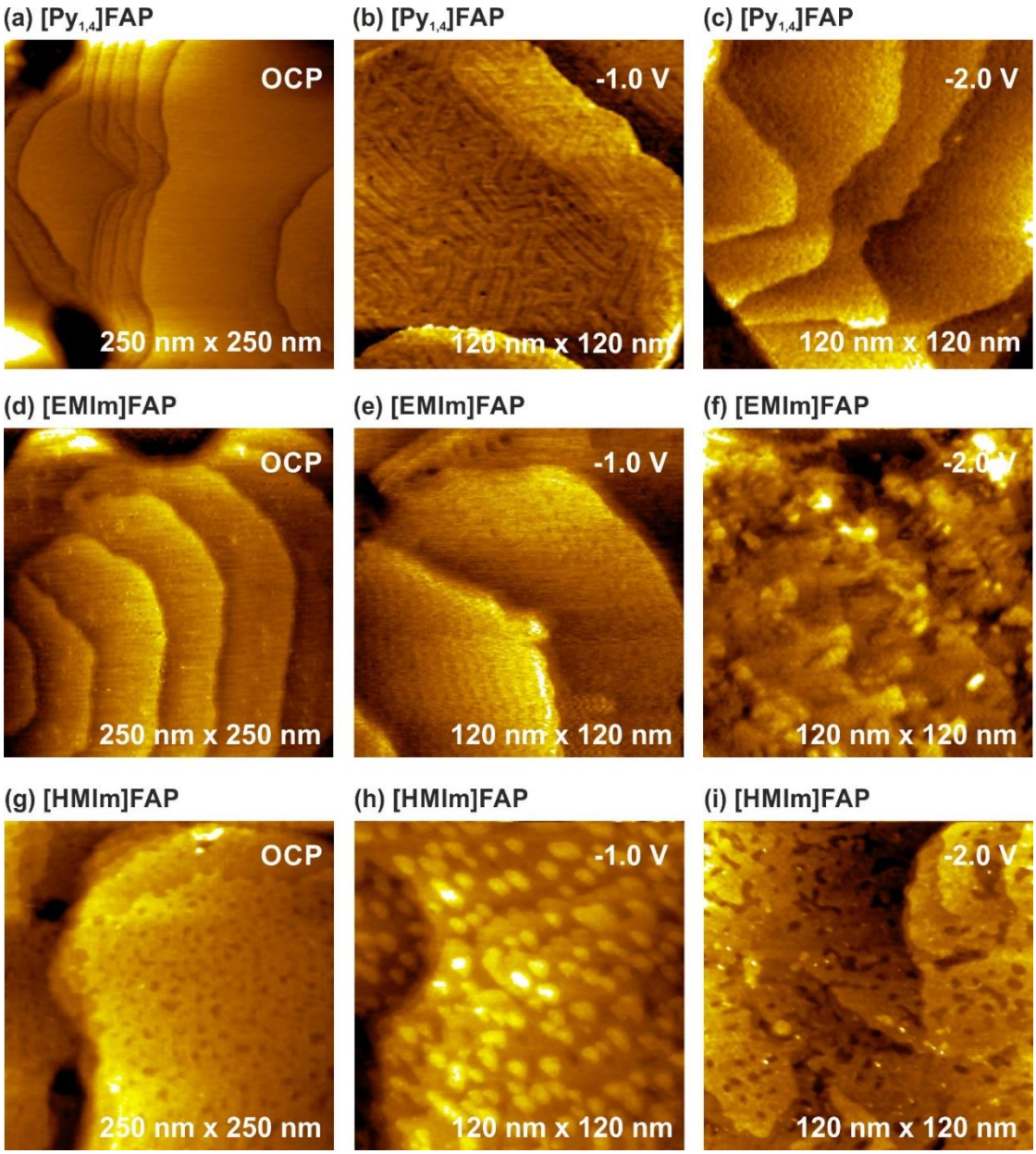

Fig. 5.1.1 *In situ STM images of the Au(111) surface at the OCP, at -1.0 V and at -2.0 V in [Py1,4]FAP (a-c), [EMIm]FAP (d-f) and [HMIm]FAP (g-i). Adopted from ref. [76]*

The IL/Au(111) interfaces were investigated by AFM as a function of potential in order to understand the ion arrangement at the interface and the Au(111) appearance in these ILs [109, 191, 230]. The atomically smooth Au(111) surface is an ideal substrate for this type of AFM investigations, as low roughness enhances the near surface structure. Therefore, changes in force distance profiles may be directly correlated with variation in IL near surface structure.

Figure 5.1.2 shows force-separation profiles for an AFM tip approaching the Au(111) surface at various potentials in [Py1,4]FAP, [EMIm]FAP and [HMIm]FAP. Beyond ~ 6 nm zero force is recorded as the tip experienced negligible resistance

moving through the IL towards the gold surface. In the case of $[Py_{1,4}]$FAP at the OCP (-0.2 V) at least five IL layers are present at the interface (fig. 5.1.2a) [109, 171]. The first outermost detectable layer is obtained at ~ 4 nm from the interface. The force increased as the tip ruptures the layer and jumps 0.9 nm before encountering another layer at 3.1 nm, and the process is repeated. Four 0.9 nm sized steps are probed by *in situ* AFM, which is in excellent agreement with the $[Py_{1,4}]$FAP ion pair (0.89 nm). The force required to rupture the layer increases for each layer as the tip moves closer to the surface that indicates that IL structure is more pronounced closer to the surface. The step closest to the surface is only 0.35 nm, which is much smaller for ion pair or $[FAP]^-$ anion (0.54 nm) and correspond well with the diameter of the $[Py_{1,4}]^+$ cation. This means that the innermost layer is enriched in $[Py_{1,4}]^+$. Furthermore, the push-through force increases from 4 nN for the ion pair at 1.3 nm to 18 nN for the innermost layer at 0.35 nm. The number of solvation layers and the force required to rupture these layers increase by reducing the electrode potential. At -1.0 V the width of the ion layer in contact with the gold becomes thinner (0.25 nm in fig. 5.1.2b), indicating that the cation adopts an orientation that renders it more parallel to the surface, which in turn induces the Au(111) (22 x √3) reconstruction (seen in fig. 5.1.1b). At -2.0 V the innermost cation layer is that strongly bound to the surface that the AFM tip cannot push through this layer and move into contact with the surface. The first layer is detected at 0.5 nm, which corresponds to $[FAP]^-$ anion (fig. 5.1.2c). *In situ* STM reveals that at this electrode potential the Au(111) terraces appear quite rough (fig. 5.1.1c).

In the case of [EMIm]FAP, two small steps, 0.3 nm and 0.5 nm wide, are detected closest to the surface, which likely correspond to cation (0.3 nm) and anion (0.5 nm) sublayers (fig. 5.1.2d). Their sum (0.3 nm + 0.5 nm) gives the [EMIm]FAP ion pair dimension (0.83 nm) [171]. The next 4 steps are 0.8 nm wide that correlate with the IL ion pair. At a potential of -1.0 V, instead of an anion layer adsorbed at the surface, an ion-pair sized step is detected in the second layer (fig. 5.1.2e). The push-through force increases from 7 nN at the OCP to 25 nN at -1.0 V indicating that the layers become more strongly adsorbed to the surface. If the electrode potential is further reduced to -2.0 V the cation layer becomes that strongly bound to the surface that the tip cannot rupture it. The first detectable layer is 0.5 nm thick corresponding to the $[FAP]^-$ anion (fig. 5.1.2f). *In situ* STM clearly shows the presence of a layer on the gold surface, whose structure significantly changes during cathodic polarization (fig. 5.1.1g-i).

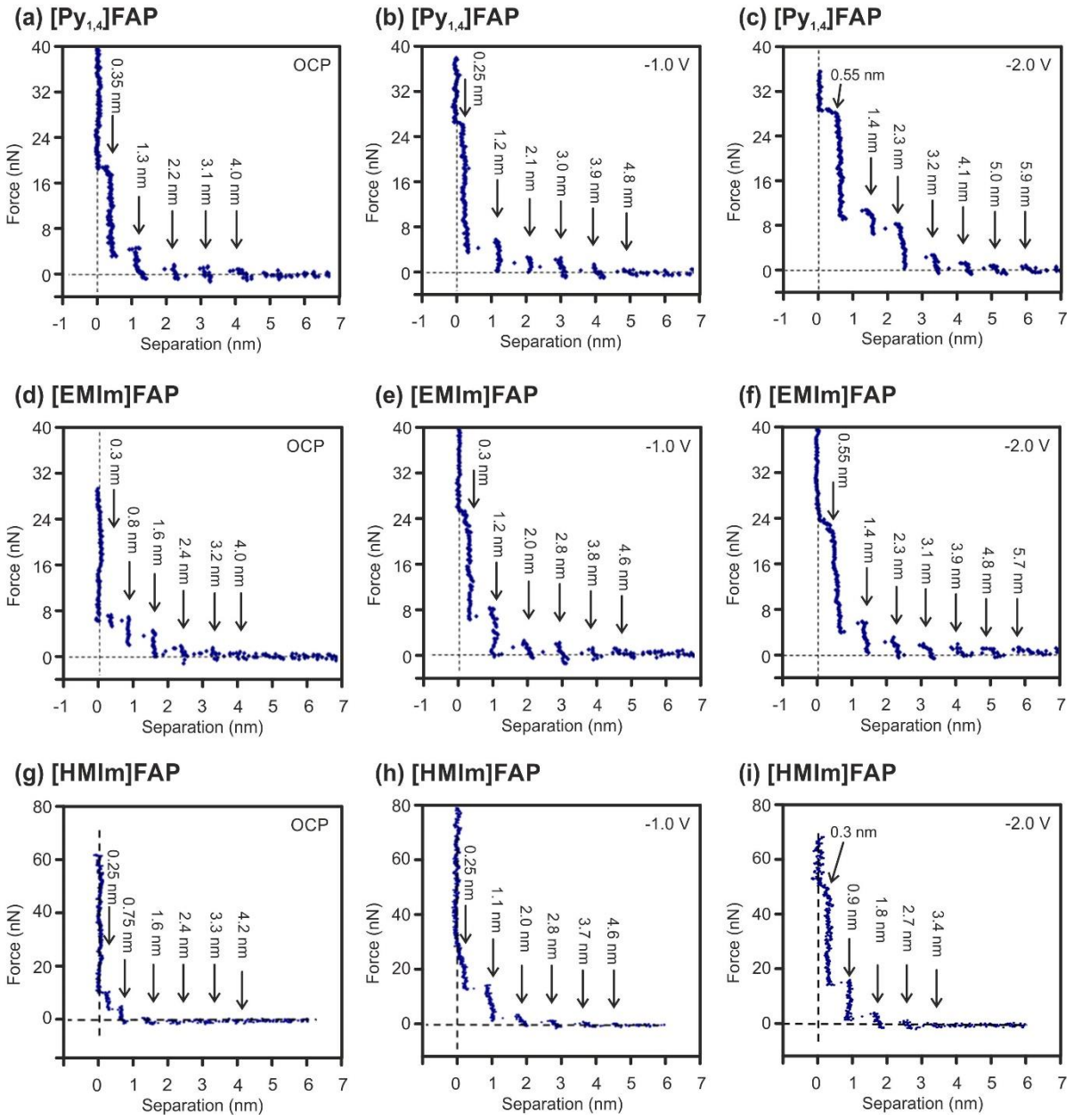

Fig. 5.1.2 *Typical force versus separation profiles for an AFM tip approaching a Au(111) surface at the OCP, at -1.0 V and at -2.0 V in [Py$_{1,4}$]FAP (a-c), [EMIm]FAP (d-f) and [HMIm]FAP (g-i). Adopted from refs. [76, 171, 191]*

Similar to [EMIm]FAP, in the case of [HMIm]FAP a weakly bound cation-rich interfacial layer (0.25 nm) covered by an anion rich layer (0.5 nm) followed by four ion pair layers (0.8 nm thick) are obtained at OCP (-0.2 V) (fig. 5.1.2g). The STM images revealed a wormlike surface pattern with ~ 0.3 nm deep vacancies at the OCP (fig. 5.1.1g). If the electrode potential is reduced to -1.0 V, a cation-sized and an ion pair sized step are detected in the first and the second layers, respectively (fig. 5.1.2h). At this electrode potential the cation layer is more strongly bound and the STM reveals the existence of 0.2 – 0.4 nm high islands, which would be consistent with the size of the cation (fig. 5.1.1h).At more negative electrode potentials (-2.0 V) the innermost layer is

cation-rich (fig. 5.1.2i). However, the force required to rupture this layer increases to 50 nN indicating its strong adsorption. It should be mentioned that the absolute tip-sample separation distance is not known in an AFM experiment, therefore, it is possible that more than one tightly bound (undetectable) cation layer is present at the surface. The STM shows the formation of larger islands of 0.4 – 0.6 nm in height (fig. 5.1.1i).

Interestingly, at positive electrode potentials (+1.0 V; +2.0 V) *in situ* AFM measurements revealed that the innermost layer for all the ILs are anion rich (~0.5 nm) [171, 191], while the STM images showed that the Au(111) surface is subject to restructuring in these ILs, which differs from those obtained by the cathodic polarization [109, 191, 230].

The Au(111) surface exhibits a wormlike appearance with 0.3 – 0.4 nm deep vacancies at the OCP, when immersed in $[Py_{1,4}]$TFSA (fig. 5.1.3a) [173, 201], [EMIm]TFSA (fig. 5.1.3b) [173] and 1-octyl-3-methylimidazolium bis(trifluoromethylsulfonyl)amide ([OMIm]TFSA) (fig. 5.1.3c). These ILs show a stable electrochemical behaviour with electrochemical windows of larger than 5 V. Similar to $[Py_{1,4}]$FAP, in the cathodic regime the Au(111) surface undergoes a $(22 \times \sqrt{3})$ reconstruction in $[Py_{1,4}]$TFSA leading to the herringbone superstructure pattern (fig. 5.1.3d). However, for [EMIm]TFSA and [OMIm]TFSA, the herringbone superstructure was not obtained (fig.5.1.3e, f). In [OMIm]TFSA the wormlike pattern remains stable at more negative electrode potentials (fig. 5.1.3f), while in [EMIm]TFSA an almost vacancy-free terrace-like Au(111) surface is noted (fig. 5.1.3e).

AFM measurements reveal that at the OCP the innermost layer is 0.65 nm and 0.6 nm thick in the case of $[Py_{1,4}]$TFSA and [EMIm]TFSA, respectively (fig. 5.1.4a, c). These step widths are narrower than expected (0.79 nm for $[Py_{1,4}]$TFSA and 0.75 nm for [EMIm]TFSA) due to electrostatic attractions that induce a flatter orientation of the organic cation to the gold surface. The force required to rupture the innermost layer is higher for $[Py_{1,4}]$TFSA than for [EMIm]TFSA. At -1.0 V the innermost layer becomes thinner in the case of $[Py_{1,4}]$TFSA (fig. 5.1.4b), while for [EMIm]TFSA the thickness of the innermost layer does not change (fig. 5.1.4d) compared with the OCP. This means that the pyrrolidinium cation adopts a flatter orientation to the gold surface at -1.0 V, which in turn can induce gold reconstruction.

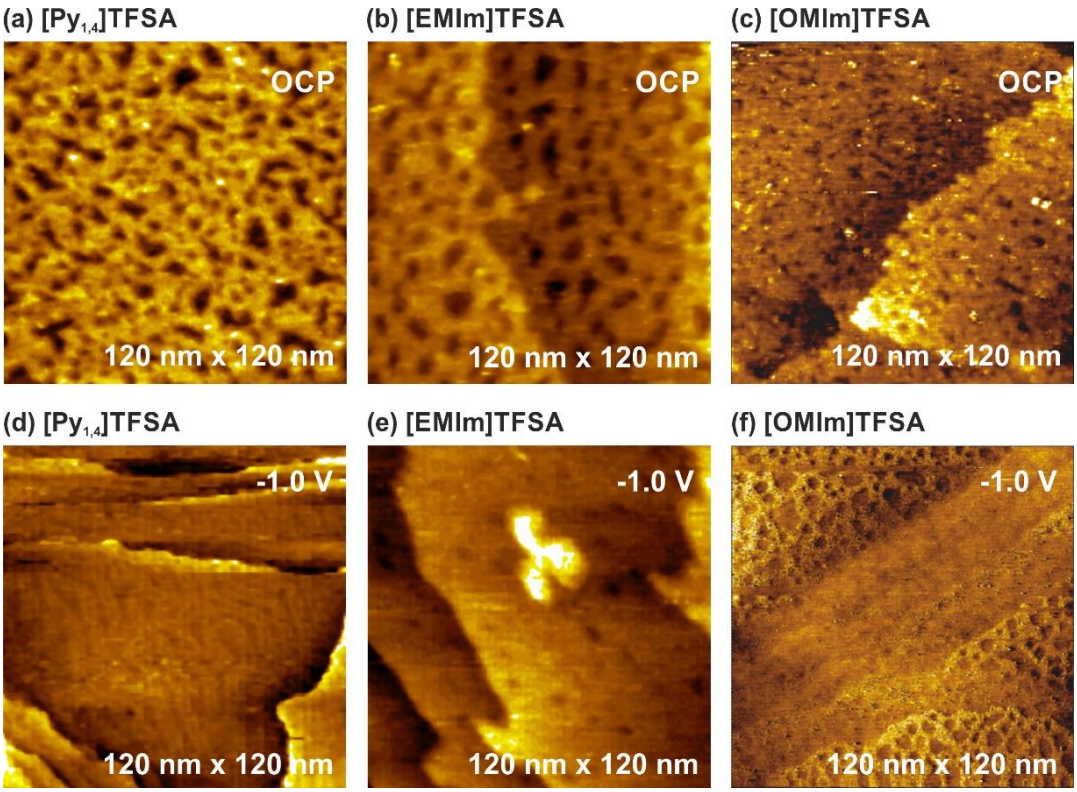

Fig. 5.1.3 *In situ STM images of the Au(111) surface at the OCP and at -1.0 V in [Py1,4]TFSA (a, d), [EMIm]TFSA (b, e) and [OMIm]TFSA (c, f). Reproduced from ref. [75]*

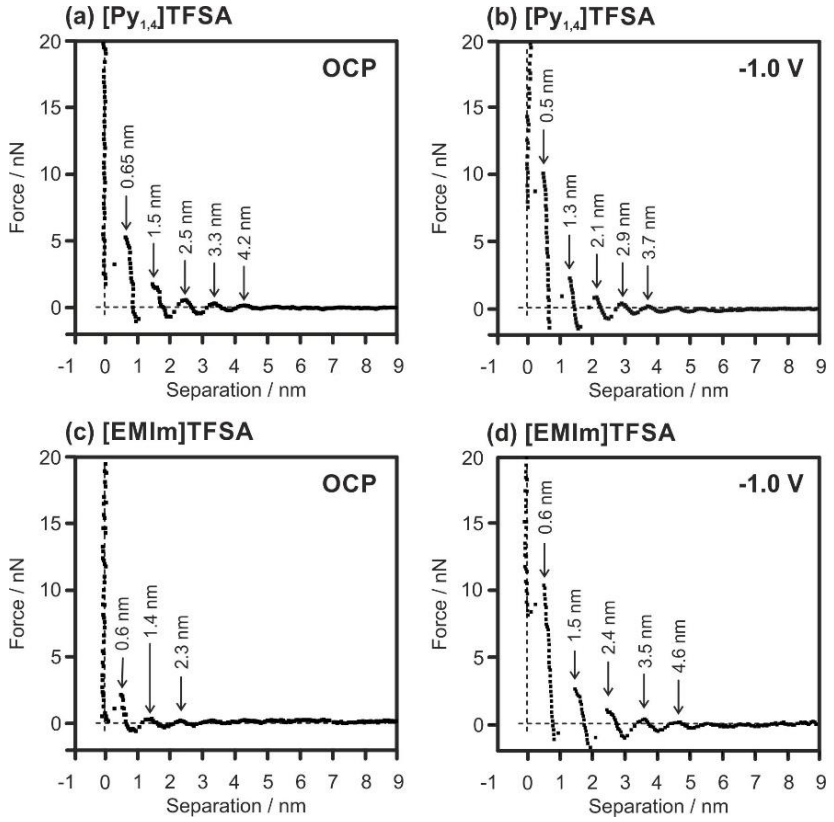

Fig. 5.1.4 *Typical force versus separation profile for an AFM tip approaching the Au(111) surface at the OCP and at -1.0 V in [Py1,4]TFSA (a, b) and [EMIm]TFSA (c, d).*

These *in situ* STM and AFM results show that both the cation and the anion of the IL have a strong influence on the structure and composition of the interface. The different Au(111) surface structures observed when the IL is changed (fig. 5.1.1 and fig. 5.1.3) are due to specific cation/surface, cation/anion and cation/cation interactions. With the same anion, the Au(111) surface undergoes the (22 x √3) reconstruction with $[Py_{1,4}]^+$, but with $[EMIm]^+$, $[HMIm]^+$ and $[OMIm]^+$ the herringbone superstructure has not been obtained. Different ions have different orientations in the interfacial layer depending on their chemical structure and applied electrode potential, which in turn induces different electrode structures. The cation/Au(111) surface interaction is dependent on the type of the functional groups (pyrrolidinium or imidazolium ring and the length of the alkyl chains) resulting in a different interfacial structure for various cations. Thus, a particular geometrical configuration of $[Py_{1,4}]^+$ at a potential of -1.0 V causes the Au(111) (22 x √3) reconstruction, while $[EMIm]^+$, $[HMIm]^+$ and $[OMIm]^+$ do not seem to favour the herringbone superstructure under similar experimental conditions.

5.2 IL / HOPG Interface

The interfacial structure of ILs at the highly ordered pyrolytic graphite (HOPG) interface has attracted some attention in order to understand solvation of nanotubes, graphene, fullerene and various electrochemical applications in supercapacitors, etc. In this chapter the key results described in ref. [75, 166] are summarized.

Similar to Au(111) interfaces, on HOPG the ions arrange into ion/ion pair layers near the interface. The higher the electrode potential, the higher the number of interfacial layers and the forces required to push through a layer. The width of the final steps shows that the Stern layer is rich in counter-ions strongly bound to the HOPG surface that the AFM tip cannot push through. In most cases, more layers and higher push-through forces are detected at the positive potentials than at negative potentials of the same magnitude, i.e. anion packing in the adsorbed (Stern) layer is more effective for templating structure in subsequent layers than cations [163, 169]. This is opposite to results on Au(111) where a more pronounced interfacial structure is found at negative potentials.

The formation of various IL superstructures has been probed with *in situ* STM in [OMIm]TFSA on HOPG (fig. 5.1.5) [166]. The electrochemical window of about 3 V is limited in the cathodic regime by the irreversible reduction of the organic cation at ca. -2.3 V vs. Pt. At OCP (-0.4 V) a periodic structure with a lattice spacing of 0.26 nm is obtained (fig. 5.1.5a). This structure is attributed to a superstructure of the

underlying HOPG. However, the image quality is lower compared to similar STM images in air and in aqueous solutions due to stronger adsorption of the IL ions to the graphite surface, which disturbs the tunneling process considerably. At -2.1 V vs. Pt a marked change in the appearance of the interface occurs (fig. 5.1.5b). With time an unusual periodic structure with semicircle-like structures of 1.2 nm in diameter forms (fig. 5.1.5c). By increasing the electrode potential a square-like structure with lattice spacing of 1.7 nm appears at -2.0 V (fig. 5.1.5d) followed by the formation of a more complicated overstructure revealing “lines” with a spacing of 2 nm at -1.9 V (fig. 5.1.5e). The lateral size of these structures (between 1.2 and 1.7 nm) suggests that cations and anions form ordered layers before the liquid is decomposed at the cathodic limit. The lattice space of the periodic structure is about 6-8 times “larger” than the structure of the underlying HOPG. Such structures must be correlated with adsorbed $[OMIm]^+$ cations. DFT calculations revealed that the lattice dimension of an $[OMIm]^+$ cation arranged parallel is about 1.7 nm [166], which corresponds well to the dimension of the obtained features.

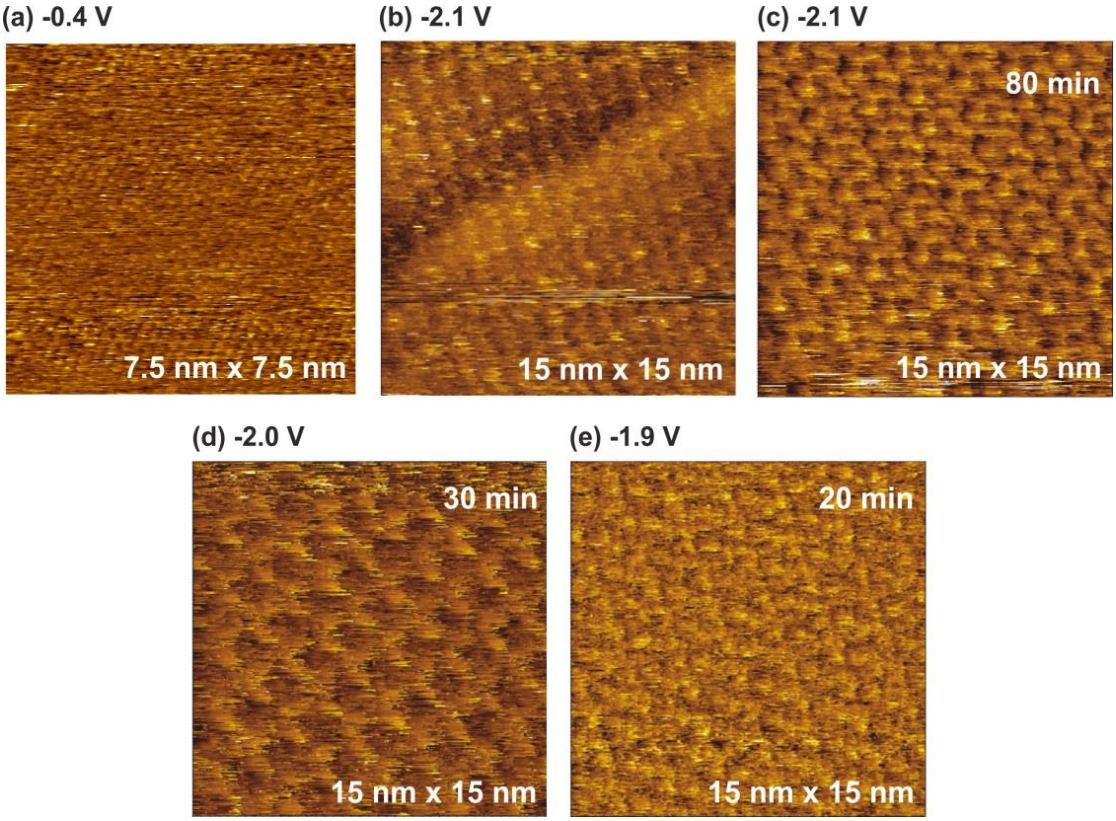

Fig. 5.1.5 *In situ STM images of the HOPG surface in [OMIm]TFSA at different electrode potentials. Reproduced from ref. [75]*

It is possible that more than one layer of cations gives rise to the structure imaged using STM. For this purpose, Fast Fourier Transformation (FFT) of the STM image in fig. 5.1.5e was performed. FFT post processing reveals a complex overstructure,

which cannot be rationalized by a single ion layer from geometric considerations, thus it must be result of a superposition of at least two ordered monolayers at the IL/HOPG interface (fig. 5.1.6). *In situ* AFM measurements prove that at -2.0 V at least two cation layers are present next to the surface and the one closest to the surface is that strongly bound to the surface that the AFM tip cannot displace it [166]. Furthermore, it was found that with time the second last layer was incorporated into the superstructure at -2.0 V resulting in the formation of the unusual overstructures on the HOPG surface (fig. 5.1.5b-e).

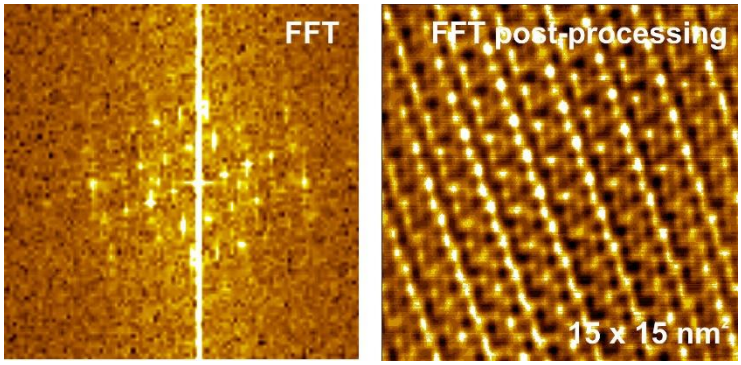

Fig. 5.1.6 *FFT of the STM image in fig. 5.1.5e and inverse FFT image calculated from the most distinctive peaks from FFT image. Reproduced from ref. [166]*

These structures are correlated with adsorbed $[OMIm]^+$ cations as in this potential regime the innermost layer is highly enriched in cations and strongly bound to the graphite surface according to AFM measurements and DFT calculations [166]. The energetically most favorable orientation within this layer is with the $[OMIm]^+$ octyl chains aligned “epitaxially” along the graphitic lattice. This induces quasi-crystallization of cations on the graphite surface and formation of the overstructure. An alternative explanation may be that, because of the bulkiness of the cation sitting along the surface, a single layer of cations is unable to quench the surface potential, thus a second layer forms. The most energetically favourable way to do this might be in a quasi-crystalline / multilayered fashion. It could also be a combination of strong surface binding / orientations and the need for multilayers to quench the charge.

6 Influence of Solutes on the IL / Electrode Interface

The content of this section was partly published in ref. [74-76, 167, 170, 188, 209, 231]. In this thesis the key results are summarized and discussed.

The part of this work was financially supported by the Deutsche Forschungsgemeinschaft (DFG) within Priority Program SPP 1191-Ionic Liquids (grant numbers: EN 370/8-3 and EN 370/14-1).

6.1 IL / Au(111) Interface

Solutes have a strong influence on the double layer structure in aqueous systems [232]. In 2006 it was found that even a very low concentration (ppm regime) of a dissolved material originating from the synthesis process can alter the interfacial structure and chemistry of the IL interface [210]. Thus, the formation of metallic lithium on Au(111) in the “ultrapure” $[Py_{1,4}]$TFSA is noted during cathodic polarization, when $[Py_{1,4}]$TFSA made by a metathesis reaction from $[Py_{1,4}]$Cl and LiTFSA is not thoroughly washed. Furthermore, an “ultrapure” [EMIm]TFSA purified with Al_2O_3 to remove organic impurities can also show an unexpected behavior at the IL-Au(111) interface, as Al_2O_3 seems to be dissolved in the IL in very low (ppm) concentrations and deposited at the electrode surface [210]. Therefore, the addition of metal and semiconductor salts (e.g. in the case of electrodeposition process) must influence the IL-electrode interfacial structure significantly.

In general, the surface interactions and adsorption morphology are markedly different in the presence of dissolved solutes than for pure ILs alone [75]. Figure 6.1.1 shows *in situ* STM images of the Au(111) surface immersed in the pure $[Py_{1,4}]$FAP and in $[Py_{1,4}]$FAP containing 0.1 M of TaF_5, LiCl or $SiCl_4$, respectively. In the case of the pure $[Py_{1,4}]$FAP, in the cathodic regime the Au(111) surface undergoes a (22 x $\sqrt{3}$) surface reconstruction. The herringbone superstructure pattern is first noted at -0.7 V (fig. 6.1.1a), and then obtained in a large potential regime (fig. 6.1.1e). In general, the herringbone reconstruction is obtained in the presence of all three salts; however the appearance of the Au(111) surface changes significantly. In the presence of 0.1 M TaF_5 vacancies are probed at -0.7 V and simultaneously the (22 x $\sqrt{3}$) reconstruction occurs (fig. 6.1.1b). The vacancies disappear completely with decreasing of the electrode potential and at -1.9 V the Au(111) surface exhibits a beautiful herringbone superstructure pattern (fig. 6.1.1f). In the case of 0.1 M LiCl, first herringbones appear at -0.8 V (fig. 6.1.1c). However, instead of a completely

reconstructed gold surface, only a partial reconstruction is seen. Furthermore, this process is very slow and it can even be probed how the rims grow and change with time by reducing the electrode potential [209]. At -1.4 V vacancies with a depth of 250-500 pm form in the non-reconstructed surface (fig. 6.1.1g). Similar to the pure IL the herringbone reconstruction appears already at -0.7 V in the [$Py_{1,4}$] FAP containing 0.1 M $SiCl_4$ (fig. 6.1.1d). However, by reducing the electrode potential, instead of a completely reconstructed gold surface, only a partial reconstruction is seen (fig. 6.1.1h). Furthermore, as in the case of the IL containing LiCl, some vacancies can also be obtained at -1.4 V.

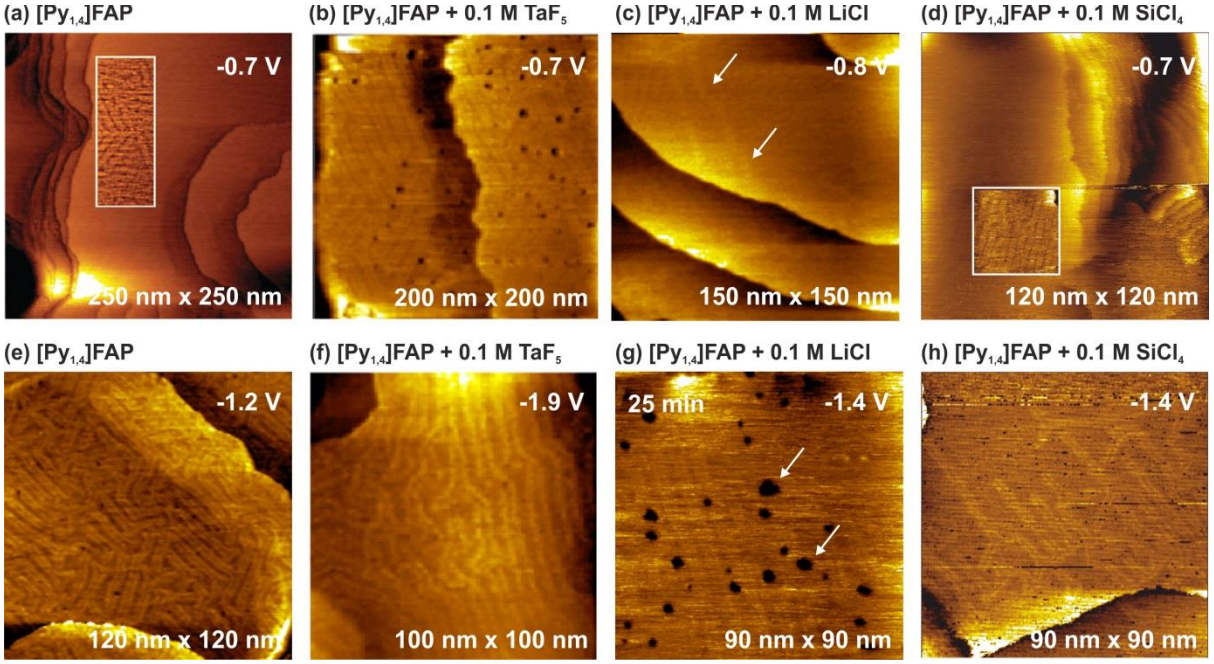

Fig. 6.1.1 *In situ STM images of the Au(111) surface obtained during cathodic polarization in the pure [$Py_{1,4}$]FAP (a, e), 0.1 M TaF_5/[$Py_{1,4}$]FAP (b, f), 0.1 M LiCl/[$Py_{1,4}$]FAP (c, g) 0.1 M $SiCl_4$/[$Py_{1,4}$]FAP (d, h). Reproduced from ref. [75]*

The variation in the interfacial structure for the pure [$Py_{1,4}$] FAP suggests that at negative electrode potentials (-1.0 V, -2.0 V) the innermost layer is enriched in cations strongly bound to the surface, which induces the herringbone reconstruction (fig. 5.1.2a-c) [109, 171]. The various solutes have a different influence on the interfacial structure. In the case of the IL containing LiCl or $SiCl_4$, the presence of Li^+ and Si(IV) affects interactions between $[Py_{1,4}]^+$ and the gold surface [233]. At negative electrode potentials these cations are present at the IL-Au(111) interface together with $[Py_{1,4}]^+$ disturbing the interfacial structure and hindering the Au(111) (22 x $\sqrt{3}$) surface reconstruction, while the increased surface electrode potential favours an interfacial structure leading to the herringbone reconstruction. As a result of these two competing effects, the Au(111) surface undergoes an incomplete herringbone reconstruction in

[$Py_{1,4}$] FAP in the presence of LiCl or $SiCl_4$. However, the addition of TaF_5 does not influence the interfacial structure significantly, consistent with *in situ* AFM data which reveal that Ta ions are expelled from the IL-Au(111) interface and do not disturb the interfacial layers [167].

Interestingly, not only solutes, but also their concentration can significantly alter the IL/electrode interfacial nanostructure. Force-separation profiles in figs. 6.1.3-6.1.5 show the influence of the concentration of sodium bis(fluorosulfonyl)amide (NaFSA) on the structure of the Au(111)/ 1-butyl-1-methylpyrrolidinium bis(fluorosulfonyl)amide ([$Py_{1,4}$]FSA) interface [231]. The pure [$Py_{1,4}$]FSA exhibits a strong interfacial nanostructure (fig. 6.1.2). At the OCP (+0.2 V vs. Pt) five prominent peaks are detected at separation distances of 0.7 nm, 1.6 nm, 2.4 nm, 3.2 nm and 4.0 nm (fig. 6.1.2a). Each peak represents the rupturing of a solvation layer of the [$Py_{1,4}$]FSA by the AFM cantilever. The force required to rupture each layer increases as the tip approaches the Au(111) surface and about 10 nN is needed to push through the innermost layer at 0.7 nm, which correspond to the presence of the [$Py_{1,4}$]FSA ion pair (0.7 nm). The composition of the interfacial structure does not change by reducing the electrode potential, however, the force required to rupture each layer increases significantly (fig. 6.1.2b, c). In general, an increase in force and decrease in separation distance in the innermost layer is observed for ionic liquids and has been related to better ordering of the interfacial structures (see Chapter 5). However in the case of [$Py_{1,4}$]FSA, a five times increase in force is required to rupture the innermost layer, which is much stronger compared to other ILs measured using the same technique. At -1.0 V about 50 nN force is required to rupture the innermost layer at 0.7 nm. Such high forces can be related to stronger interaction of [$Py_{1,4}$]FSA with the Au(111) surface.

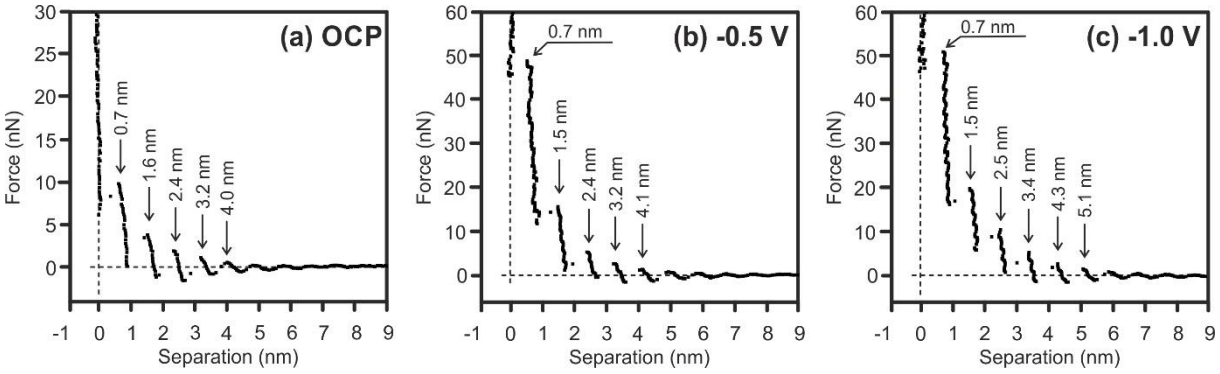

Fig. 6.1.2 *Force-separation curves of an AFM tip approaching a Au(111) surface in [$Py_{1,4}$]FSA at (a) OCP, (b) -0.5 V and (c) -1.0 V. Reproduced from ref. [231]*

The profile of the force-separation curves does not change significantly with addition of 0.05 M NaFSA in $[Py_{1,4}]FSA$ (fig. 6.1.3). Four (at OCP) and five (at -0.5 V and at -1.0 V) solvation layers corresponding each to the IL ion pair are observed at the IL/Au(111) interface. Similar to the pure IL, a force of about 10 nN is required to rupture the innermost layer at 0.7 nm at OCP (fig. 6.1.3a). However, in contrast to the pure IL the push-through forces do not increase significantly in the presence of 0.05 M NaFSA by reducing the electrode potential (fig. 6.1.3b). Thus, at -1.0 V a force of only 15 nN is needed to push the innermost layer (fig. 6.1.3c). This implies that there is some interaction of Na^+ with the IL that weakens the IL-surface attraction. Raman spectra reveal the formation of $[Na(FSA)_3]^{2-}$ species in the bulk phase, which in turn might also affect the IL/Au(111) interfacial structure [231].

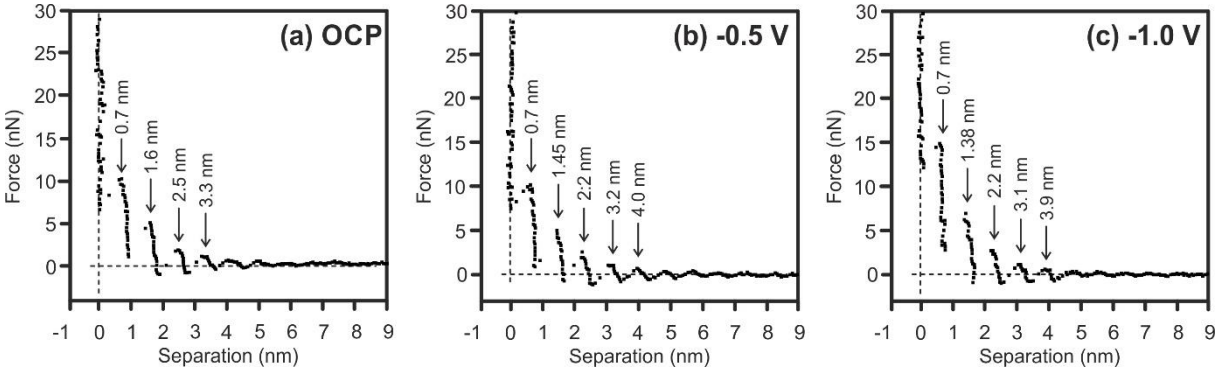

Fig. 6.1.3 *Force-separation curves of an AFM tip approaching a Au(111) surface in $[Py_{1,4}]FSA$ containing 0.05 M NaFSA at (a) OCP, (b) -0.5 V and (c) -1.0 V. Reproduced from ref. [231]*

The interfacial structure changes significantly on increasing the concentration of NaFSA to 0.25 M (fig. 6.1.4). At the OCP (fig. 6.1.4a), the innermost layer width is 0.4 nm, that can be related to the presence of sodium ions at the interface, which form $[Na(FSA)_3]^{2-}$. The separation distance of the second solvation layer is > 0.9 nm, which indicates the presence of both $[Na(FSA)_3]^{2-}$ and $[Py_{1,4}]FSA$ ion pairs.

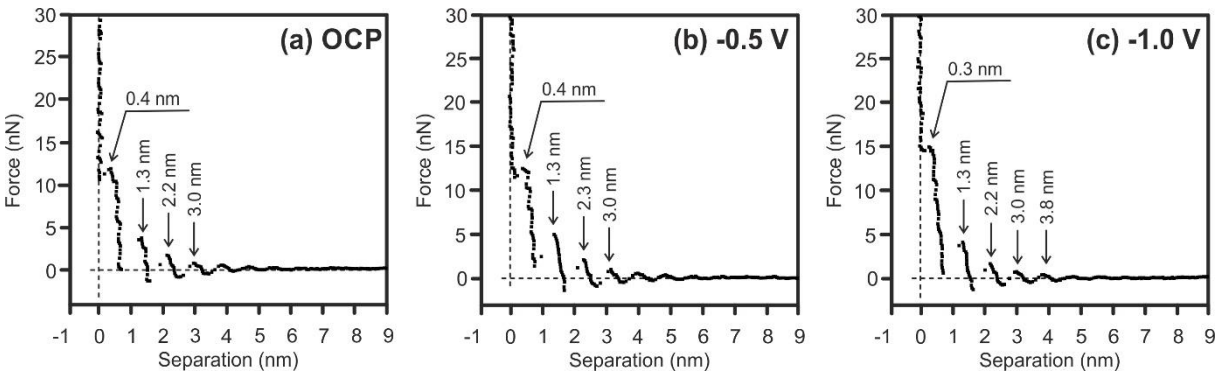

Fig. 6.1.4 *Force-separation curves of an AFM tip approaching a Au(111) surface in $[Py_{1,4}]FSA$ containing 0.25 M NaFSA at (a) OCP, (b) -0.5 V and (c) -1.0 V. Reproduced from ref. [231]*

On changing the potential to -0.5 V (fig. 6.1.4b), no significant change in the separation or force is observed, which indicates that a well ordered structure is formed at the interface. On further reducing the electrode potential to -1.0 V (fig. 6.1.4c), again the innermost structure shows a separation distance of 0.3 nm, which within the uncertainty limit of AFM measurements corresponds to the formation of a $[Na(FSA)_3]^{2-}$ layer at the interface. The AFM measurements suggest that an interfacial structure consisting of $[Na(FSA)_3]^{2-}$ in the innermost layer and a mixture of both $[Na(FSA)_3]^{2-}$ and $[Py_{1,4}]FSA$ ion pair in the second layer forms at the OCP that remains stable with decreasing the electrode potential at least until -1.0 V.

Upon addition of 0.5 M NaFSA only three prominent layers are observed at the OCP (fig. 6.1.5a). However, the innermost layer shows a separation distance of 0.4 nm, which is consistent with that observed in case of 0.25 M NaFSA indicating the presence of $[Na(FSA)_3]^{2-}$. The second layer shows a distance of > 0.9 nm suggesting that both $[Na(FSA)_3]^{2-}$ and $[Py_{1,4}]FSA$ are present. On changing the potential to -0.5 V and -1.0 V (figs. 6.1.5b, c), no significant change in distance in the solvation layers are seen, but an increase in rupture force is observed indicating that the interfacial structure has become stronger.

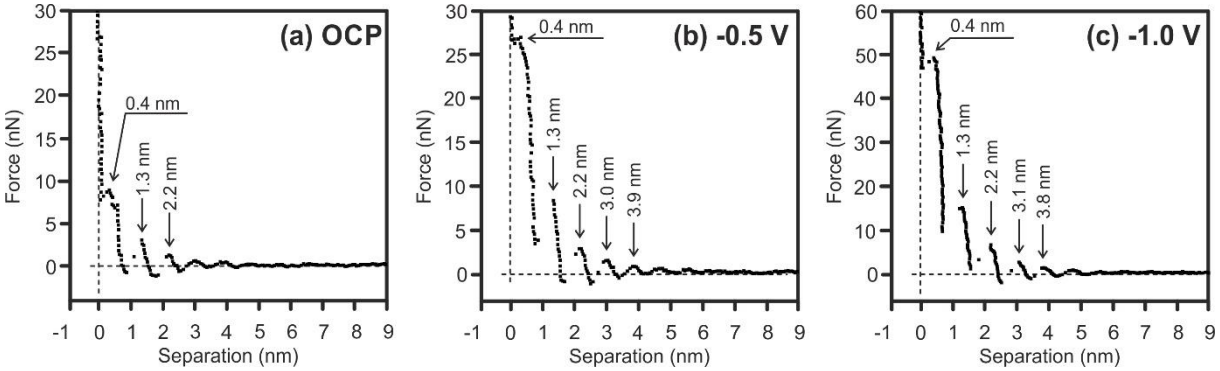

Fig. 6.1.5 *Force-separation curves of an AFM tip approaching a Au(111) surface in $[Py_{1,4}]FSA$ containing 0.5 M NaFSA at (a) OCP, (b) -0.5 V and (c) -1.0 V. Reproduced from ref. [231]*

In situ AFM force-distance measurements reveal that the addition of high concentrations Na^+ ions modify the IL/Au(111) interface. A similar observation was obtained on addition of lithium bis(trifluoromethylsulfonyl)amide (LiTFSA) in $[Py_{1,4}]TFSA$ [188]. The IL/Au(111) interface significantly changes on addition of Li^+ ion, and $[Py_{1,4}]^+$ ions are replaced by Li^+ ions at the interface, thereby reducing the separation distance of the innermost interfacial layer (fig. 6.1.6). Furthermore, on increasing the concentration of Li^+ ions, a decrease in number of interfacial layers occurs.

These results clearly show that Li^+ and Na^+ ions vary the IL/Au(111) interface, especially at high concentrations, which can alter electrochemical processes.

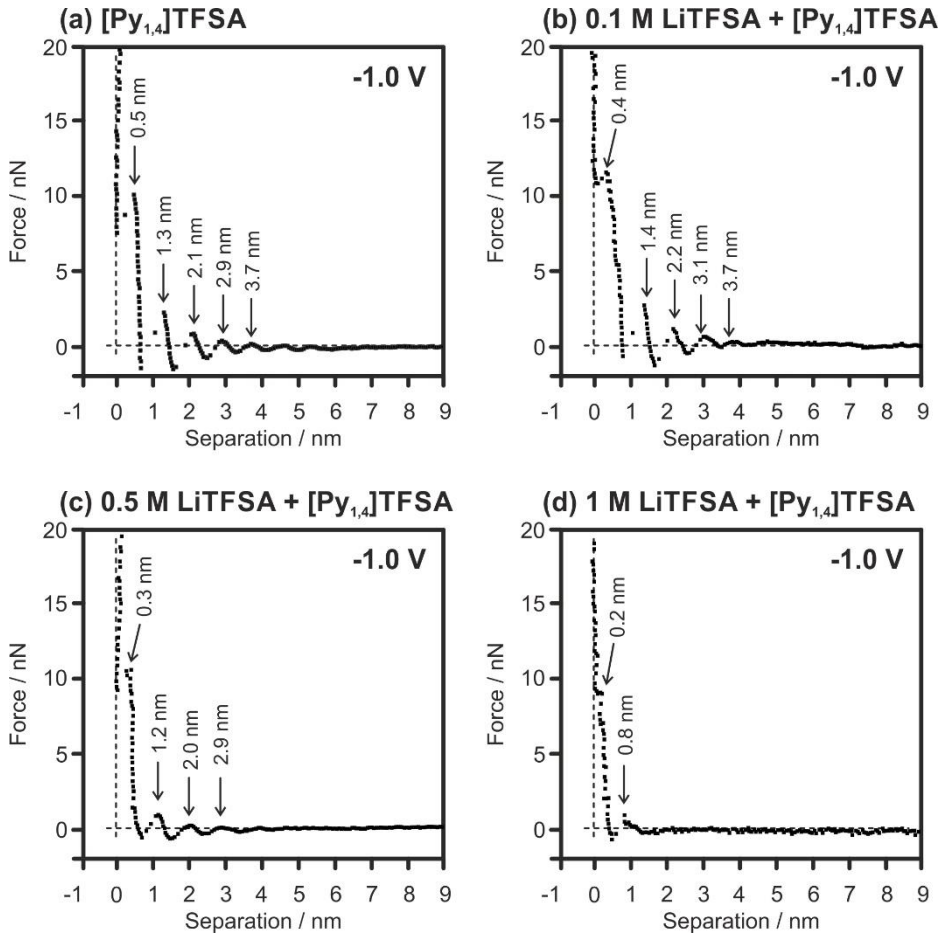

Fig. 6.1.6 *Force-separation curves of an AFM tip approaching a Au(111) surface at -1.0 V in $[Py_{1,4}]$TFSA containing (a) 0.1 M LiTFSA (b) 0.5 M LiTFSA and (c) 1.0 M LiTFSA. Reproduced from ref. [188].*

The addition of water (especially at concentrations above 30 vol%) has a strong impact on the IL/electrode interface [170]. Figure 6.1.7 shows the changes in the structure of the [EMIm]TfO/Au(111) interface at -1.0 V with increasing of the water concentration from 30 vol% to 50 vol% in the IL. In the case of 30 vol% water five solvation layers are obtained at -1.0 V (fig. 6.1.7a). The width of the innermost layer is 0.6 nm, which correlates well with the diameter of the IL ion pair. Both the number of the solvation layers and the width of the innermost layer decrease if more water is added into the IL. Thus, at 40 vol% water three layers with an innermost layer at 0.6 nm are present (fig. 6.1.7b), while at 50 vol% only one layer at 0.4 nm corresponding to the hydrated cationic layer can be detected (fig.6.1.7c).

In situ AFM force-separation measurements revealed that up to 30 vol% water, the typical multilayered IL/electrode structure exists. The innermost structure has a dimension between 0.5 and 0.6 nm and does not change much with varying

potential [170]. A drastic change in the innermost layer was obtained on increasing the water concentration to 50 vol%. Furthermore, a spectroscopy study showed that the cation-anion interactions diminished above 30 vol% water [170]. At 50 vol% the C-H stretching peak corresponding to C(2) position of the imidazolium ring of the pure IL was not observed, which suggests that at 50 vol%, the interface is determined by cations bound to water. Above 50 vol% of water only one well-ordered (Stern) layer exists at the interface and is dominated by hydrated $[EMIm]^+$. Thus, between 30 vol% and 50 vol% of water in the [EMIm]TfO there is a clear transition from a multilayered interfacial structure typical for the pure IL to a classical double layer structure well-known for aqueous electrolytes, which can be clearly seen in figure 6.1.7.

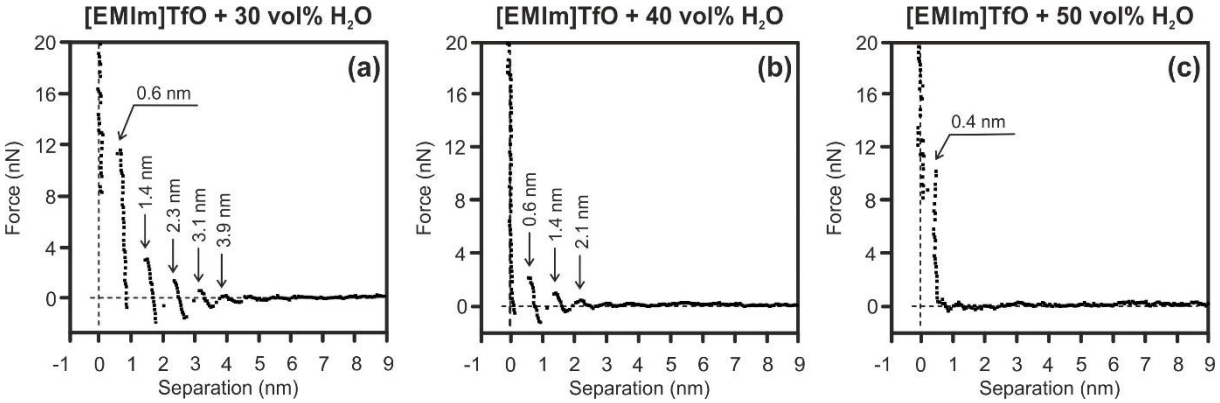

Fig. 6.1.7 *Typical force-separation curves of an AFM tip approaching a Au(111) surface in [EMIm]TfO with (a) 30, (b) 40 and (c) 50 vol% water at -1.0 V. Reproduced from ref. [170].*

In situ STM and AFM measurements confirm that the dissolved solute is present within the Stern layer. The altered interfacial structures represent the best compromise between the IL ion and solute surface affinities, packing constraints, and charge localisations.

6.2 IL / p-Si(111) Interface

The nanostructure of the IL/Si interface was studied using a Cypher S (Asylum Research) AFM inside of a glove box under argon atmosphere [74]. The AFM topography image of H-terminated p-Si(111) under argon is presented in figure 6.2.1. The pure H-Si(111) structure is characterized by large terraces (fig. 6.2.1a) separated by steps of about 310 pm in height (fig. 6.2.1b), which is in good agreement with the expected step height of 313 pm for the Si(111) double-layer periodicity. The terraces of the Si(111) surface are rather rough and zooming in shows that monolayer deep pits are present. Such pits are typical for hydrogen-terminated Si(111) due to the H-related states of the monohydride (SiH) and/or trihydride (SiH_3) phases on Si(111).

Furthermore, contaminations adsorbed during the wet treatment processes can also be present on the surface. The force versus separation curve for an AFM tip approaching the H-Si(111) surface reveals that in argon the jump-to-contact region is ascribed by a small attractive force due to van der Waals attractions between the tip and the surface (fig. 6.2.1c).

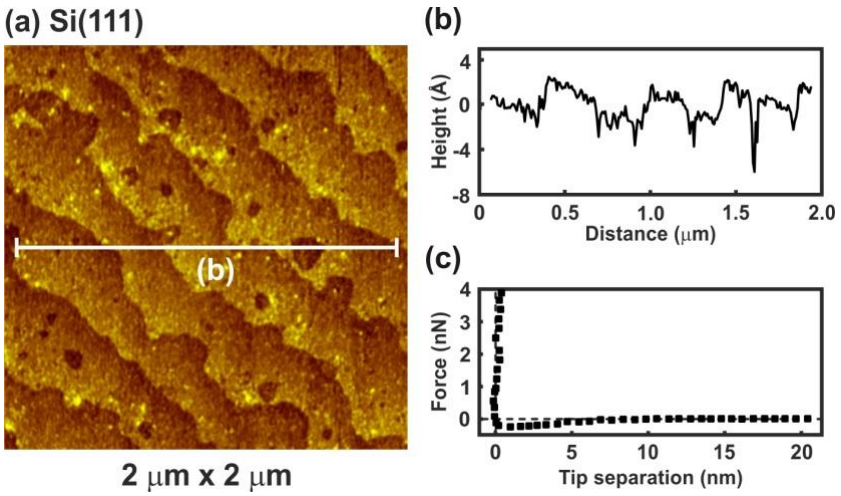

Fig. 6.2.1 *(a) AFM topographic image of the pure H-terminated p-Si(111) surface. (b) Height profile of the H-Si(111) corresponding to the white line drawn in fig. 6.2.1a. (c) Force versus separation profile for an AFM tip approaching the H-Si(111) surface in argon atmosphere. Reproduced from ref. [74].*

Figure 6.2.2 shows the nanostructure of the IL/Si(111) interface in pure [EMIm]TFSA and in the presence of 0.1 M LiTFSA at the OCP. The terraces-like Si(111) structure can be recognized both in the case of the pure IL and in the presence of the Li salt (fig. 6.2.2a and fig. 6.2.2d). However, in general, the surface becomes very rough and the atomic steps cannot be distinguished clearly. Higher magnification (200 nm × 200 nm) images of the terrace are presented in fig. 6.2.2b and fig. 6.2.2e. In the case of the pure [EMIm]TFSA a periodic facet structure can be identified (fig. 6.2.2b). To obtain a more pronounced periodic structure, the original topographic image was processed by FFT with a threshold filter followed by an Inversed Fast Fourier Transformation (IFFT) to return a topographic image (fig. 6.2.2c). The processed image contains only periodic components with an amplitude larger than the selected threshold value of 0.007. The average width of each facet is about 3.7 nm (fig. 6.2.2f, black curve), which is significantly larger than the dimensions of individual IL cations (0.3 nm) and anions (0.5 nm) and even of an IL ion pair (0.8 nm). The obtained structure reproduces the subcell lattice of the Si(111) (7 × 7) surface reconstruction, which is shown in the 40 nm × 40 nm inset in fig. 6.2.2c (white points).

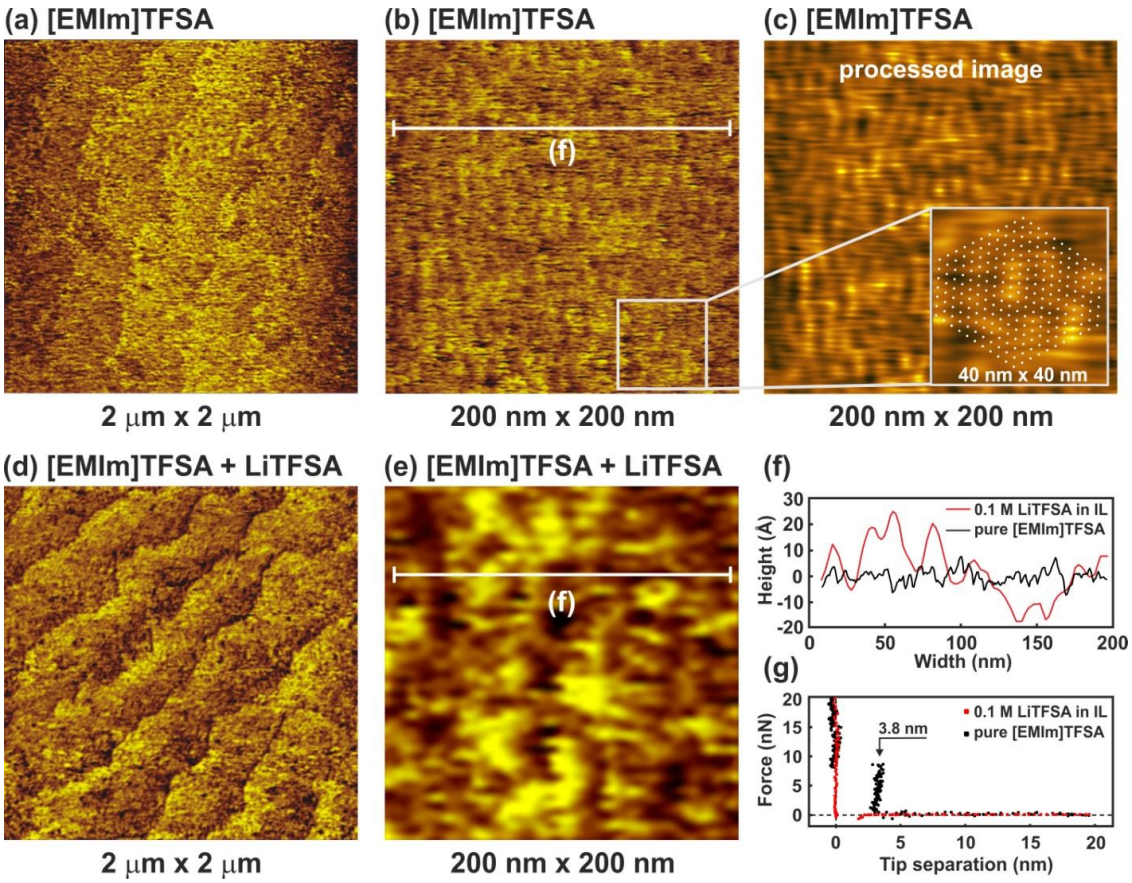

Fig. 6.2.2 *(a, b) AFM topographic images of the H-Si(111) in [EMIm]TFSA. (c) the topographic image of (b) after image processing. (d, e) AFM topographic images of H-Si(111) in [EMIm]TFSA containing 0.1 M LiTFSA. (f) Height profiles of H-Si(111) corresponding to the white lines in figure 6.2.2b and 6.2.2f in the pure IL (black line) and with with 0.1 M LiTFSA (red line). (g) Force versus separation profiles for an AFM tip approaching H-Si(111) in the pure IL (black dots) and with 0.1 M LiTFSA (red dots). Reproduced from ref. [74].*

The force-separation profile reveals the existence of one adsorbed interfacial layer (fig. 6.2.2g, black dots) with a width of about 3.8 ± 0.1 nm, which is the same within uncertainty as the spacing between facets in the AFM image. Furthermore, on continuous scanning, it was observed that the ordered structure is removed. However, the structure can be reobtained on imaging the same site after a while, which suggests that the clusters are not very strongly adsorbed to the H-terminated Si(111). IR measurements revealed that there is an interaction between IL ions and the H-Si(111) surface, which leads to the formation of the orders facet structure present in the AFM images [74]. Therefore, in the case of H-Si(111), the H-termination might have induced ordering of imidazolium IL by van der Waals interaction and suggests a structure formed from many ions or ion pairs.

On addition of 0.1 M LiTFSA, the facet structure disappears completely (fig. 6.2.2e) and the surface becomes rougher (fig. 6.2.2f, red curve) meaning the image quality

decreases (zooming in did not deliver more information). No push throughs are found in the force distance profiles, which means the rough “layer” interacts weakly with the surface (fig. 6.2.2g, red dots). These results show that, as for Au(111) surface, the addition of LiTFSA disrupts interactions between the Si(111) surface and the IL, which weakens the interfacial structure significantly.

Figure 6.2.3 represents the nanostructure of the IL/H-Si(111) interface in pure [$Py_{1,4}$]TFSA and in the presence of 0.1 M LiTFSA at OCP.

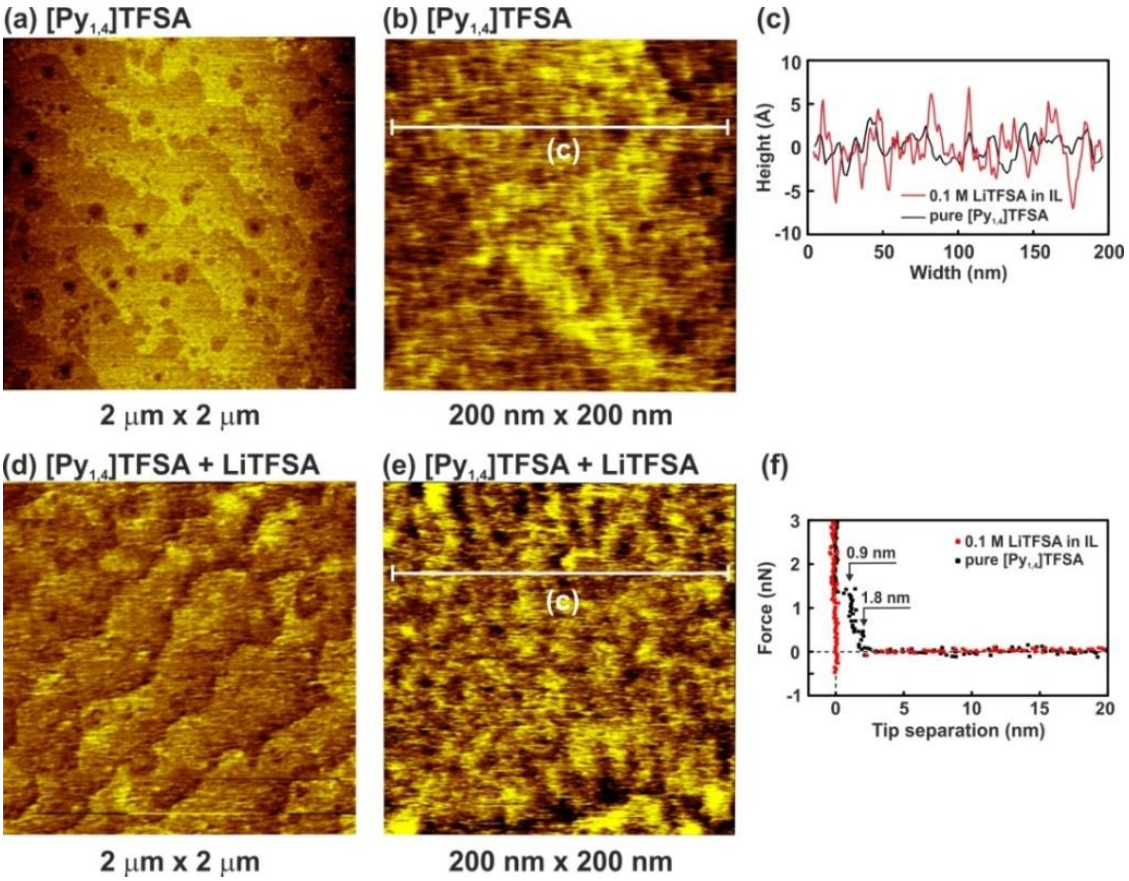

Fig. 6.2.3 *(a, b) AFM topographic images of H-Si(111) in [$Py_{1,4}$]TFSA. (c) Height profiles of H-Si(111) corresponding to the white line in fig. 6.2.3b and 6.3.2e in the pure IL (black line) and with 0.1 M LiTFSA (red line). (d, e) AFM topographic images of H-Si(111) in [$Py_{1,4}$]TFSA containing 0.1 M LiTFSA. (f) Force versus separation profiles for an AFM tip approaching H-Si(111) in the pure IL (black dots) and with 0.1 M LiTFSA (red dots). Reproduced from ref. [74].*

In the case of the pure [$Py_{1,4}$]TFSA the typical terraces-like Si(111) structure with the step height of 310 nm is obtained (fig. 6.2.3a). However, a higher magnification shows that a rough layer is present on the surface of the terraces (fig. 6.2.3b and fig. 6.2.3c, black curve). The force-separation profile reveals the presence of two interfacial layers at 1.8 nm and 0.9 nm (fig. 6.2.3f, black dots), which corresponds well with the diameter of the IL ion pair (0.8 nm). The interfacial layers of [$Py_{1,4}$]TFSA are weaker than for [EMIm]TFSA (~ 9 nN), and only ~ 1.5 nN force is needed to rupture the innermost

layer. The quality of the images decreases significantly with addition of 0.1 M LiTFSA (fig. 6.2.3d). The roughness of the “layer” that is present on the surface increases (fig. 6.2.3e and fig. 6.2.3c, red curve). As for LiTFSA the force-separation profile does not reveal the existence of any interfacial layers (fig. 6.2.3f, red dots). IR measurements also showed that the interaction of $[Py_{1,4}]$TFSA with the Si(111) surface is much weaker compared to [EMIm]TFSA [74]. Moreover, *in situ* XPS measurements revealed that [EMIm]TFSA influences the electronic structure of H-Si(111) resulting in a change of the band gap, and the apparent band gap of H-Si(111) can be varied by increasing the thickness of the IL film [234].

In general, *in situ* STM and AFM studies reveal that some unusual interactions can take place between the cation and/or anion of the IL and the solid surfaces. The applied potential has also an impact on the ion organization at the IL/solid interface. Furthermore, the presence of solute can significantly alter the existing IL/solid interfacial nanostructure, which in turn may influence the electrochemical processes at the IL/solid interface leading sometimes to “unexpected” results, which are discussed in the following chapter.

7 Material Synthesis in ILs

The content of this section was partly published in ref. [167, 228, 229, 235]. In this chapter the key results are summarized and discussed.

Raman spectra were recorded with a VERTEX 70 V, RAM 2 (Bruker Optic GmbH) with a (Nd:YAG 1064 nm laser) Ge detector. For Raman analysis, the electrolytes were sealed in a glass capillary inside of the glove box and then transferred to the instruments. Fourier transform infrared spectroscopy was also performed using VERTEX 70 V (Bruker Optic GmbH). The Raman and IR spectra were recorded at an average of 250 scans with a resolution of 2 cm^{-1}.

The morphology of the electrodeposits was characterized using scanning electron microscope (SEM) from JEOL (JSM 7610F). The SEM measurements were performed by Mrs. Silvia Löffelholz.

Part of this work was financially supported by the Deutsche Forschungsgemeinschaft (DFG) within Priority Programs SPP 1191-Ionic Liquids (grant numbers: EN 370/8-3 and EN 370/14-1) and SPP 1708-Material Synthesis near Room Temperature (grant numbers: BO 4290/1-1 and BO 4290/1-2) and by the Bundesministerium für Bildung und Forschung (BMBF) within the project LUZI (grant number: 03SF0499A).

7.1 Electrodeposition of Tantalum

Tantalum is one of the key elements in many applications due to its special anticorrosive properties and inertness in aggressive electrolytes. As for most refractory metals, high temperature molten salts of alkali metal halides as a solvent and K_2TaF_7 as a source of Ta have been used for the electrodeposition of tantalum. A low temperature electrodeposition would have many advantages from a technical point of view. Due to its negative deposition potential Ta cannot be electrochemically deposited from aqueous solutions. Ionic liquids, due to their low melting points, good thermal and chemical stabilities, low vapour pressure, high ionic conductivities and large electrochemical windows, have attracted the interest of chemists as perspective electrolytes for the electrodeposition of refractory metals and in particular tantalum [236]. However, it was obtained that the electrodeposition of tantalum from ILs is not straightforward and the IL has a strong influence on the electrochemical process and on the quality of the deposited tantalum [167, 237, 238]. In this chapter the results described in ref. [229] are summarized.

In general, the electrodeposition of Ta from its halides in an IL is complicated by the formation of non-stoichiometric sub-halides. In the case of $[Py_{1,4}]$TFSA, TaF_5 is reduced via TaF_3, TaF_2, $TaF_{1.5}$ and Ta_2F to elemental Ta, which can form TaF_x again by decreasing the electrode potential to more negative values [238]. Nevertheless, it was found that elemental Ta can be deposited from TaF_5 in different ILs with $[TFSA]^-$ anions and various cations [237]. However, no elemental Ta was obtained in $[Py_{1,4}]$FAP containing TaF_5 even at elevated temperature (above 100 °C) [167]. *In situ* STM and AFM measurements reveal that $[Py_{1,4}]$TFSA and $[Py_{1,4}]$FAP adsorb differently onto Au(111) (Chapter 5) and solutes (e.g. TaF_5) can significantly alter the IL/electrode interface (Chapter 6). Therefore, the question arises, if the electroactive species of TaF_5 in $[Py_{1,4}][TFSA]$ differ from $[Py_{1,4}][FAP]$ and how they can alter the deposition process.

Typical cyclic voltammograms (CVs) of 0.1 M TaF_5 in $[Py_{1,4}][TFSA]$ and in 0.1 M TaF_5 of $[Py_{1,4}][FAP]$ on Au(111) at 25 °C are presented in figure 7.1.1. The electrode potentials were initially swept negatively from the OCP at a scan rate of 10 mV s^{-1}.

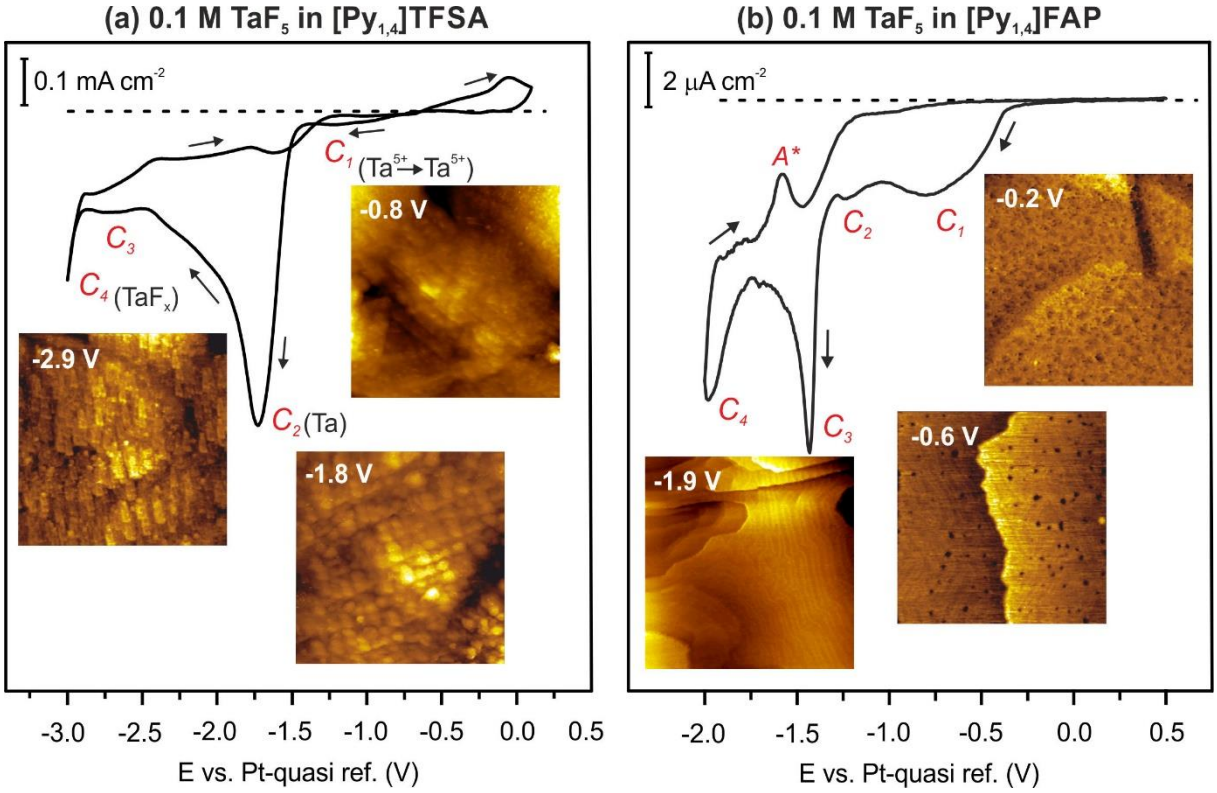

Fig. 7.1.1 *CVs of 0.1 M TaF_5 in (a) $[Py_{1,4}]$TFSA and (b) $[Py_{1,4}]$FAP on Au(111) at RT and in situ STM images of the Au(111) surface in these electrolytes at the mentioned electrode potentials. Reproduced from ref. [229]*

In the case of TaF_5-$[Py_{1,4}]$TFSA, a series of reduction processes (C_1-C_4) is obtained prior to the decomposition of the organic cation (fig. 7.1.1a). *In situ* STM shows that

at -0.8 V (C_1) a thin rough layer is present on the gold surface, at -1.8 V (C_2) a clear deposit forms and by further reducing the electrode potential to -2.9 V (C_3-C_4) “chopstick like” structures are observed (STM images in the insets of fig 7.1.1a). Electrochemical quartz crystal microbalance (EQCM) measurements reveal that at C_2 the deposition of elemental Ta occurs, while C_1, C_3 and C_4 are correlated with the formation of various non-stoichiometric tantalum sub-halides [167].

In the case of TaF_5-[$Py_{1,4}$]FAP, four cathodic processes (C_1-C_4) can also be seen, however the current densities are very low for the reduction processes (fig. 7.1.1b). *In situ* STM reveals that the Au(111) surface is subject to reconstruction. At -0.2 V (OCP), a rough gold surface with wormlike structures is observed. By reducing the electrode potential, a surface restructuring occurs (C_1-C_3) leading to the (22 x √3) reconstruction, which remains stable until -2.0 V (C_4) (insets in fig. 7.1.1b). EQCM measurements do not indicate any deposition of elemental Ta in this IL [167].

Changes in the interfacial structures of [$Py_{1,4}$]TFSA and [$Py_{1,4}$]FAP containing TaF_5 were also probed using *in situ* AFM force-distance measurements. Figure 7.1.2 represents force versus separation curves for an AFM tip approaching Au(111) at -1.0 V (prior to the electrodeposition of Ta) in [$Py_{1,4}$]TFSA and [$Py_{1,4}$]FAP in the presence (red) and in the absence (black) of 0.1 M TaF_5.

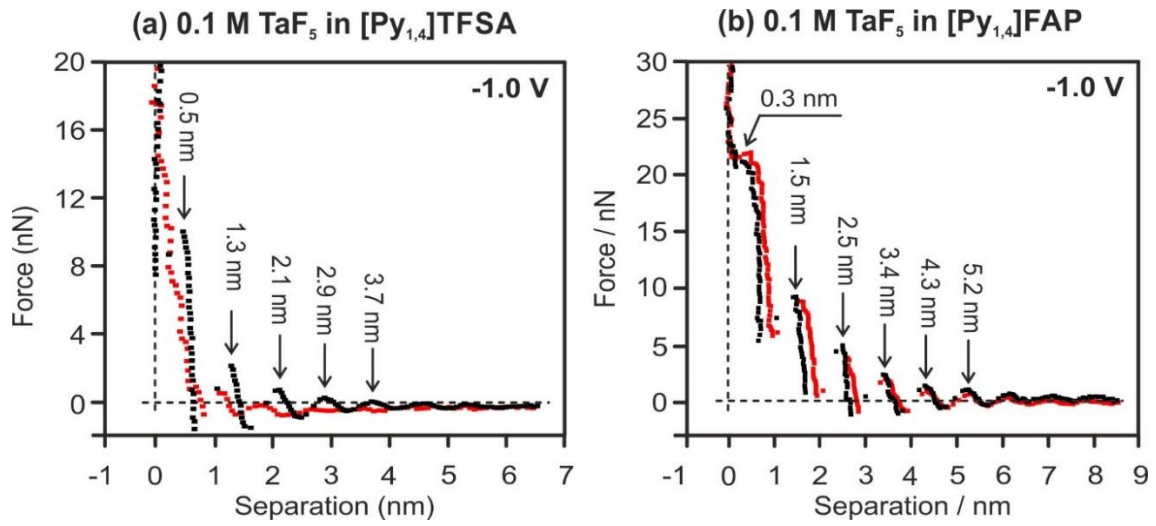

Fig. 7.1.2 *Force versus separation profiles for an AFM tip approaching the Au(111) surface at -1.0 V in (a) [$Py_{1,4}$]TFSA and (b) [$Py_{1,4}$]FAP in the presence (red curves) and in the absence (black curves) of 0.1 M TaF_5. Reproduced from ref. [229]*

In the case of [$Py_{1,4}$]TFSA, the appearance of the force-distance curves changes markedly when TaF_5 is added to it. For the pure IL five adsorbed layers can be detected at -1.0 V (fig.7.1.2a, black curve). For all the layers the width of the steps is ~0.8 nm except for the innermost layer, which correlates well with the diameter of the IL ion

pair. The width of the innermost layer is only 0.5 nm, which is associated with $[Py_{1,4}]^+$ and indicating that the cation adopts a flatter orientation on the electrode surface under the influence of an applied electrode potential (see Chapter 5). The addition of TaF_5 weakens the interfacial structure (fig.7.1.2a, red curve). Furthermore, the width of the innermost layer reduces to 0.25 nm, which might be due to the presence of the TaF_5 species at the surface, as at more negative electrode potentials the electrodeposition of Ta occurs [167].

The important observation is that the addition of 0.1 M TaF_5 does not alter the $[Py_{1,4}]$FAP/Au(111) interface (fig.7.1.2b). Both the width of the innermost layer and the push through force remain quite similar with and without TaF_5. The width of the innermost layer is 0.3 nm, consistent with the size of $[Py_{1,4}]^+$. These results reveal that TaF_5 was expelled from the electrode surface in $[Py_{1,4}]$FAP, while in $[Py_{1,4}]$TFSA the interfacial structure is disturbed by the addition of TaF_5. Thus, $[TFSA]^-$ might interact in a different manner with TaF_5 than with $[FAP]^-$, which alters the interface.

Vibrational spectroscopy was performed to find changes in the bulk structure of ILs and TaF_5-ILs. Figure 7.1.3 shows the regions in which the changes can be observed in the Raman and IR spectra of the ILs on addition of TaF_5. The peaks are assigned based on refs. [239-242]. Marginal changes are observed in the intensities of peaks related to the ILs, indicating a weak interaction of the TaF_5 in them (fig.7.1.3a, b). However, neither new waves/peaks nor new shoulders except a new peak at ~ 690 cm^{-1} for both ILs could be observed. This new peak could be related to TaF_5-IL species. In the IR spectra of TaF_5-$[Py_{1,4}]$TFSA quite a broad new peak appears at 884 cm^{-1} (fig.7.13c), which can -however- not be assigned to a definite species. Apart from this, no recognizable changes have been observed in the IR spectrum for $[Py_{1,4}]$FAP upon addition of 0.1 M TaF_5 (fig. 7.1.3d).

It is thus quite difficult to comment on the speciation/complexation based on the vibrational spectroscopy results alone and to correlate them with the observed changes in *in situ* AFM results.

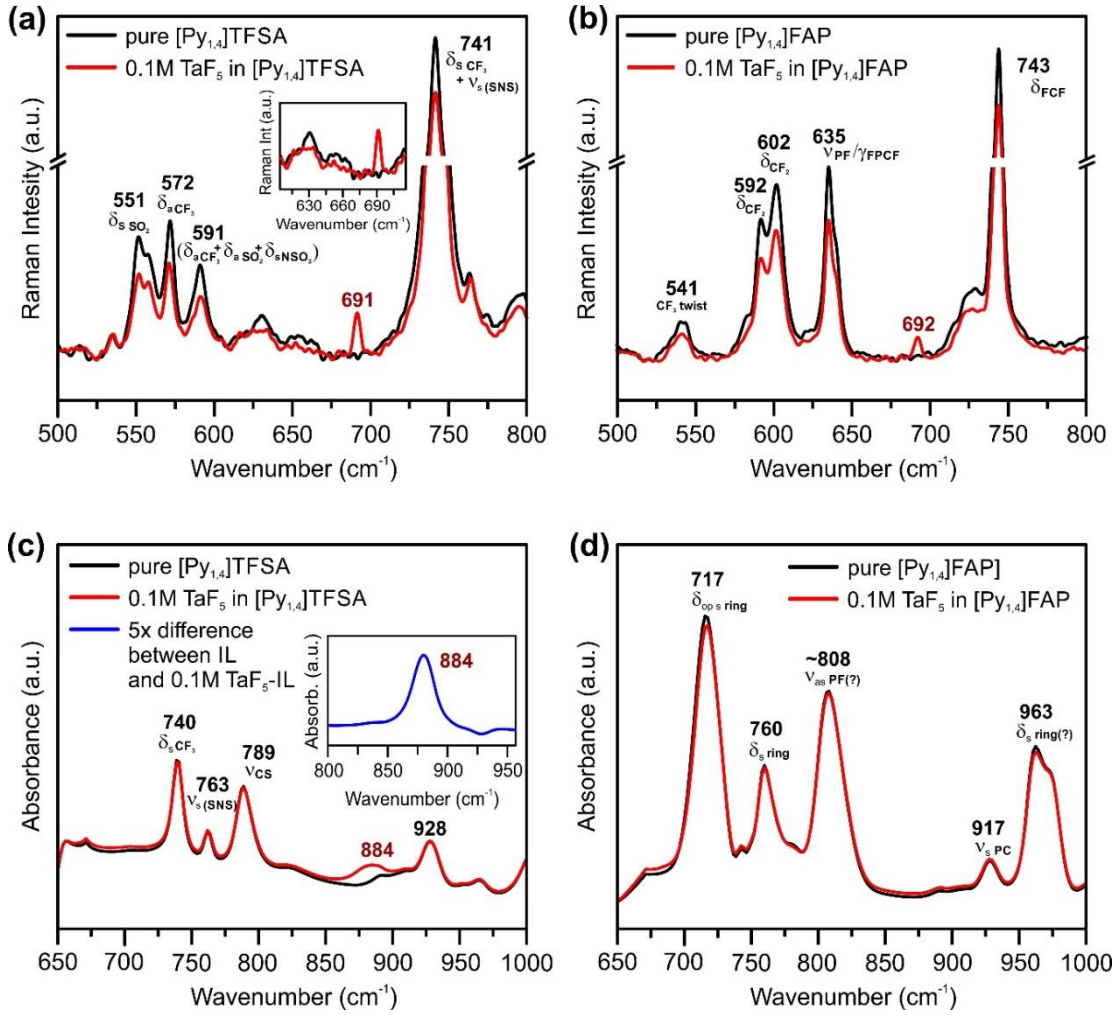

Fig. 7.1.3 *Raman spectra between the wavenumbers of 500 and 800 cm^{-1} in (a) $[Py_{1,4}]TFSA$ and (b) $[Py_{1,4}]FAP$ in the presence (red) and in the absence (black) of 0.1 M TaF_5. Comparison of IR spectra between the wavenumbers of 650 and 1000 cm^{-1} (c) $[Py_{1,4}]TFSA$ and (d) $[Py_{1,4}]FAP$ in the presence (red) and in the absence (black) of 0.1 M TaF_5. Insets in (a) show Raman spectra between 605 and 710 cm^{-1}, in (c) difference Raman spectra of the solutions, where the absorbance of $[Py_{1,4}]TFSA$ is subtracted from the absorbance of 0.1 M TaF_5-$[Py_{1,4}]TFSA$ (blue, 5× magnification). Reproduced from ref. [229]*

7.2 Electrodeposition of Silicon

ILs are promising solvents for the electrodeposition of various semiconductors, which cannot be obtained electrochemically from aqueous solutions [235]. The studies reveal that in general the quality and properties of semiconducting materials are dependent on the type of the IL used as a solvent media for the electrodeposition. Thus, the morphology and crystal size of Si deposits made electrochemically from ILs containing $SiCl_4$ can be altered by changing the constituent ions [225]. Si was electrodeposited on gold and copper at room temperature and at 100 °C from $SiCl_4$ dissolved in three different ILs with the same cation, $[Py_{1,4}]^+$, but three different anions, (e.g. $[Py_{1,4}]TFSA$, $[Py_{1,4}]TfO$ and $[Py_{1,4}]FAP$). In all cases, the electrodeposited silicon films were

amorphous. However, it was found that the number of reduction steps and the deposition potentials of Si differ upon changing the IL anion. IR spectroscopy analysis also showed that $SiCl_4$ interacts differently with the ILs leading to the formation of different electroactive species [225]. Furthermore, *in situ* STM measurements reveal a significant difference in the interfacial behavior of $SiCl_4$/[$Py_{1,4}$]TFSA and $SiCl_4$/[$Py_{1,4}$]FAP on Au(111) (fig. 7.2.1). In the case of [$Py_{1,4}$]TFSA, small Si islands appear at the electrode potential at 1.5 V more negative than the OCP (fig. 7.2.1a). Their lateral and vertical growth leads to the formation of a rough layer. If [$Py_{1,4}$]FAP is employed, a number of randomly distributed two-dimensional islands is formed at the electrode potential of 0.5 V more negative than OCP (fig. 7.2.1b). These islands grow in a layer-by layer process. The difference of Si islands deposition between [$Py_{1,4}$]TFSA and [$Py_{1,4}$]FAP is roughly 1 V. The layers deposited in both ILs exhibit a band gap of about 1.1 eV indicating the deposition of semiconducting Si (insets in fig. 7.2.1a, b).

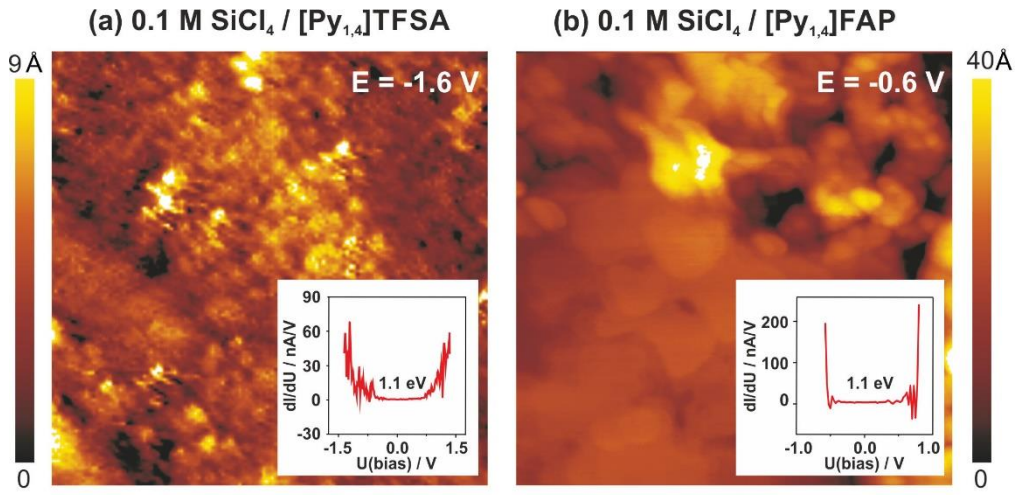

Fig. 7.2.1 *In situ STM images of the Au(111) surface in (a) 0.1 M $SiCl_4$-[$Py_{1,4}$]TFSA at -1.6 V vs. Pt and (b) 0.1 M $SiCl_4$-[$Py_{1,4}$]FAP at -0.6 V vs. Pt. Insets: in situ I/U tunnelling spectroscopy of the electrodeposits. Reproduced from ref. [235]*

Interestingly the concentration of $SiCl_4$ has also a significant influence on the structure of the IL/Au(111) interface, which in turn alters the deposition process [229]. Figures 7.2.2a and 7.2.2b show the electrochemical behaviour of [$Py_{1,4}$]FAP at two different concentrations of 0.1 M and 0.25 M $SiCl_4$ on Au(111) at room temperature. In the cathodic regime, three reduction processes (C_1-C_3) can be obtained for 0.1 M $SiCl_4$/[$Py_{1,4}$]FAP (fig. 7.2.2a). The reduction waves C_1 and C_2 can be associated with the adsorption of $SiCl_4$-IL species complexes. The bulk deposition of Si occurs at C_3. On increasing the concentration of $SiCl_4$ to 0.25 M, the magnitude of the

reduction current increases (fig. 7.2.2b). Furthermore, the potentials of surface reduction processes were not affected by increasing the concentration of $SiCl_4$ in IL. However, the onset of Si electrodeposition is significantly shifted to more positive values when increasing the concentration of $SiCl_4$ to 0.25 M. The Si deposits obtained from 0.1 M $SiCl_4$-[$Py_{1,4}$]FAP on gold are quite thin and have been observed only in STM investigations (fig. 7.2.1b). However, a relatively thick layer of Si can be obtained from 0.25 M $SiCl_4$-[$Py_{1,4}$]FAP on gold, which is surprising with respect to the results with TaF_5 (Chapter 7.1) at the first glance.

A comparison of Raman spectra for the neat IL and its solutions with two different concentrations of $SiCl_4$ (0.1 M and 0.25 M) is presented in figure 7.2.2c. The peaks are assigned based on refs. [240, 242] There are neither new waves nor new peaks for ILs containing two different concentrations of $SiCl_4$. However, on addition of 0.1 M $SiCl_4$, the intensity of the neat IL peak at 743 cm^{-1} increases, which is more pronounced at 0.25 M. This change in the intensity can be related to the formation of $SiCl_4$-IL species. To find changes in the Raman spectra, the recorded ones were analysed by subtracting the absorbance of $SiCl_4$/[$Py_{1,4}$]FAP from the absorbance of pure [$Py_{1,4}$]FAP (fig. 7.2.2d). In the difference spectra, a rise in the intensity of the peak at 743 cm^{-1} can be noticed.

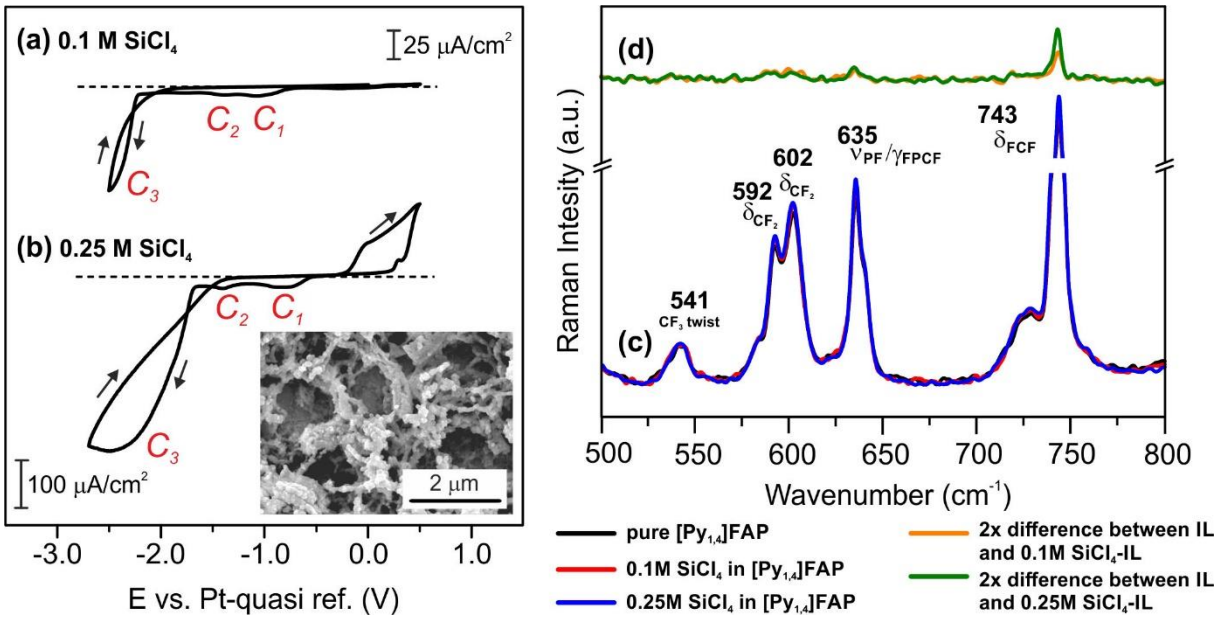

Fig. 7.2.2 *CVs of (a) 0.1 M $SiCl_4$ and (b) 0.25 M $SiCl_4$ in [$Py_{1,4}$]FAP on polycrystalline Au at 25 °C. Inset in (b) shows SEM image of Si electrodeposited at -2.5 V from 0.25 M $SiCl_4$ in [$Py_{1,4}$]FAP. (c) Raman spectra between 500 and 800 cm^{-1} in [$Py_{1,4}$]FAP (black), 0.1 M $SiCl_4$-[$Py_{1,4}$]FAP (red) and 0.25 M $SiCl_4$-[$Py_{1,4}$]FAP (blue) (d) Difference Raman spectra of the solutions, where the absorbance of [$Py_{1,4}$]FAP is subtracted from the 0.1 M $SiCl_4$-[$Py_{1,4}$]FAP (orange) and 0.25 M $SiCl_4$-[$Py_{1,4}$]FAP (green) absorbance (2× magnification). Reproduced from ref. [229]*

At present, it is unclear why the intensity of this peak increases with the concentration of $SiCl_4$ in this liquid. For a simple approximation, it might be due to weakening of the bending mode of C-F-C in the anion due to a possible interaction of $SiCl_4$ with $[FAP]^-$. Apart from such an intensity change, there was no recognizable change either in the as recorded spectra or in the difference spectra in this region of wavenumbers (500 - 800 cm^{-1}).

In situ AFM was performed to understand the effect of $SiCl_4$ concentration on the Au(111)/IL interface at the electrode potentials prior to the electrodeposition of Si [229]. As was already mentioned for the pure IL, at OCP and at slightly negative electrode potentials the width of the innermost layer is ~0.3 nm, indicating the presence of $[Py_{1,4}]^+$ on the Au(111) surface. At more negative electrode potentials (at -1.5 V and -2.0 V) the cation layer can be that strongly bound to the surface that the AFM tip cannot displace them and thus probes only the anion layer at ~ 0.6 nm (fig. 7.2.3, black curves).

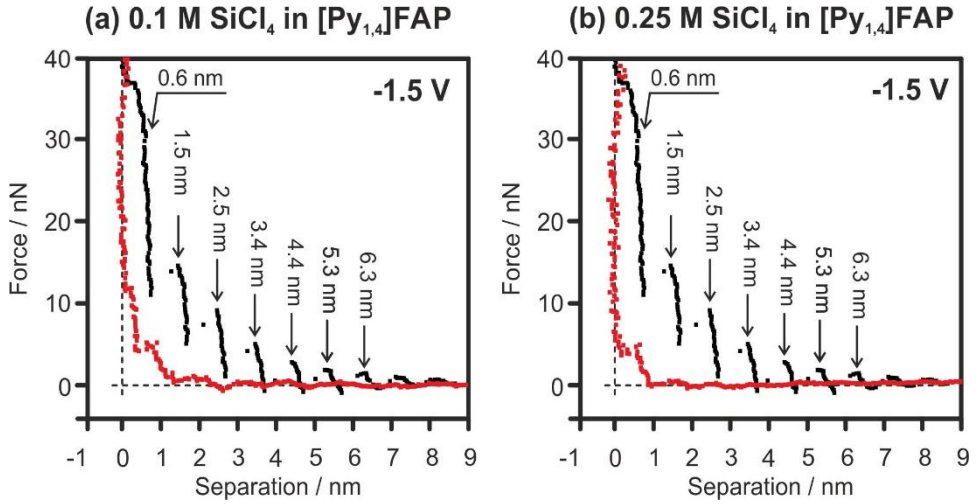

Fig. 7.2.3 *Force versus separation profiles for an AFM tip approaching the Au(111) surface at -1.5 V in $[Py_{1,4}]FAP$ (black curves) and in $[Py_{1,4}]FAP$ containing (a) 0.1 M and (b) 0.25 M $SiCl_4$ (red curves). Reproduced from ref. [229]*

However, by addition of $SiCl_4$ the appearance of the AFM curves changes significantly. In the case of 0.1 M $SiCl_4$-IL, only 3 layers (at 0.4, 0.9 and 1.9 nm) can be identified (fig. 7.2.3a, red curve). The force required to rupture the layers is significantly reduced, with only 12 nN needed to displace the innermost layer. Furthermore, the innermost layer is only 0.4 nm wide suggesting the presence of $SiCl_4$-IL species at the surface. Interestingly, on increasing the concentration of $SiCl_4$ to 0.25 M, only a double layer is seen at 0.6 nm (fig. 7.2.3b, red curve). A similar double layer structure is obtained for the Au(111)/[EMIm]TfO-H_2O interface (see Chapter 6): on increasing the water content to 50 vol%, the multilayered IL/electrode interfacial structure was changed to a double

layer structure, which consequently affected the rate and morphology of electrodeposition of Zn [170]. In the case of $SiCl_4$, increasing the concentration of $SiCl_4$ modifies the Au(111)/IL interface significantly, which can enhance the quality of the Si deposits.

7.3 Electrodeposition of Gallium

The electrodeposition of gallium is of interest for the production of III-V compound semiconductors. In general air- and water stable ILs are well suited to the electrochemical deposition of gallium at room temperature. However, the quality of the obtained electrodeposits is dependent on the IL applied as a solvent in the electrodeposition process. Herein the effect of an IL anion on gallium solvation, the structure of the IL/Au(111) interface and the morphology of Ga electrodeposits is discussed. The electrodeposition of Ga was studied in ILs with the $[Py_{1,4}]^+$ cation and three different inions, namely $[TFSA]^-$, $[TfO]^-$ and $[FSA]^-$.

Vibrational spectroscopy was performed to investigate the influence of the IL anions on the interaction/solvation of $GaCl_3$. Figure 7.3.1 shows the anion region (between 200 and 1600 cm^{-1}) of the Raman spectra for the neat ILs and their solutions with 0.3 M $GaCl_3$. In general, a decrease in the peaks intensities related to the ILs was observed on addition of $GaCl_3$ for all three ILs employed in this study. However, the changes are more pronounced for $[Py_{1,4}]$FSA upon adding $GaCl_3$. The most significant changes are noticed in three regimes: between 200 and 400 cm^{-1} for all three ILs, between 600 and 800 cm^{-1} for $[Py_{1,4}]$TfO and $[Py_{1,4}]$FSA, and between 1200 and 1250 cm^{-1} for $[Py_{1,4}]$FSA. The peaks at 740 cm^{-1} (for pure $[Py_{1,4}]$TFSA), at 756 cm^{-1} (for pure $[Py_{1,4}]$TfO) and 725 cm^{-1} (for pure $[Py_{1,4}]$[FSA) are assigned to a coupled symmetric CF_3 bending and SNS stretching modes of $[TFSA]^-$ (fig.7.3.1a, black curve), symmetric CF_3 bending mode of $[TfO]^-$ (fig.7.3.1b, black curve) and a coupled SO_2 bending and symmetric SNS stretching modes of $[FSA]^-$ (fig.7.3.1c, black curve), respectively. These bands are sensitive to interactions with metal ions [243]. The peak observed at 1216 cm^{-1} for $[Py_{1,4}]$FSA is attributed to the symmetric SO_2 stretching mode of free $[FSA]^-$. In the case of $GaCl_3$-$[Py_{1,4}]$TfO and $GaCl_3$-$[Py_{1,4}]$FSA additional peaks are observed at 768 cm^{-1} (fig.7.3.1b, red curve) and at 665 cm^{-1} (fig.7.3.1c, red curve), respectively, and such new peaks are not obtained in $GaCl_3$-$[Py_{1,4}]$TFSA. Furthermore, for $GaCl_3$-$[Py_{1,4}]$FSA, the intensity of the peak at 1216 cm^{-1} significantly reduces and an additional peak is recorded at 1230 cm^{-1}. Moreover, new peaks were found at 366 cm^{-1} for $GaCl_3$-$[Py_{1,4}]$TFSA (inset in fig. 7.3.1a) and at 363 cm^{-1} for $GaCl_3$-$[Py_{1,4}]$TfO (inset in fig. 7.3.1b), whereas in the case of $GaCl_3$-$[Py_{1,4}]$FSA, two

new peaks (at 230 and 337 cm^{-1}) were recorded (inset in fig. 7.3.1c). For further analysis, the Raman modes of $GaCl_3$ (or Ga_2Cl_6) and $GaCl_4^-$ were compared with the stretching modes of $GaCl_3$ in ILs. The Raman stretching modes ($\upsilon 1$ and $\upsilon 3$) of $GaCl_4^-$ were reported at 346 and 386 cm^{-1}, respectively [244]. The Raman spectra of $GaCl_3/Ga_2Cl_6$ at 140 °C exhibit peaks at 168, 310, 344, 416, and 472 cm^{-1} [245]. However, such peaks were not observed in the $GaCl_3$-ILs spectra, indicating that $GaCl_4^-$, $GaCl_3$ and Ga_2Cl_6 are absent in the solutions. Furthermore, a low intensity peak at 230 cm^{-1} for the FSA liquid might be attributed to the vibrational modes of Cl-Ga-N, as Ga-N vibrations in gallium trihalide complexes were reported to occur below 300 cm^{-1} [246]. The decrease in intensity of the peaks originated from ILs and the appearance of the new peaks/shoulders can be assigned to an interaction of $GaCl_3$ with the anion of the respective IL. The average coordination number for the species can be determined from signals in these regimes. It was reported that the solvation behaviour and the type of coordination of Li^+ in TFSA IL differs from FSA ILs [247]. It was shown that $[FSA]^-$ is bound to the cation in two different ways, in which $[FSA]^-$ coordinates to Li^+ in bidentate and monodentate fashion, whereas $[TFSA]^-$ is bound bidentately to Li^+. In the case of $GaCl_3$ a marked difference is also observed, where a new peak is found at low wavenumbers (665 cm^{-1}) for FSA liquid, however, there is no observable change in this regime for TFSA liquid. The $[TfO]^-$ possesses quite a strong band at 756 cm^{-1} in the Raman spectra (fig. 7.3.1b, black curve), which is sensitive to the interactions with metal ions [248]. The intensity of this peak decreases upon adding $GaCl_3$ to $[Py_{1,4}]TfO$, and also a satellite peak appears at higher wavenumbers (at 768 cm^{-1}) (fig. 7.3.1b, red curve). A similar shift was noticed for $Al(TfO)_3$-Digylme systems [249].

Figure 7.3.2 represents a comparison of IR spectra for the pure ILs and their mixtures with 0.3 M $GaCl_3$ between 450 and 1500 cm^{-1}. In the case of $GaCl_3$-$[Py_{1,4}]TFSA$, the peak at 1175 cm^{-1}, which can be related to the asymmetrical CF_3 stretching mode of $TFSA^-$, is blue shifted by ~4 cm^{-1} (fig. 7.3.2a, red curve). Furthermore, two additional broad peaks at 881 and 1437 cm^{-1} are observed, which cannot yet be assigned to definite species. Similar observations were obtained for $[Py_{1,4}]TFSA$ containing 0.1 M TaF_5 (Chapter 7.1). Marginal changes are observed in the IR spectra of $[Py_{1,4}]TfO$ with and without $GaCl_3$ (fig. 7.3.2b). There are neither new waves/peaks nor new shoulders except a peak at 1300 cm^{-1} (fig. 7.3.2b, red curve). In the case of $GaCl_3$-$[Py_{1,4}]FSA$, the IL peak at 730 cm^{-1} corresponding to the symmetrical SNS bending mode of FSA^- is blue shifted by ~8 cm^{-1} on addition of $GaCl_3$ (fig. 7.3.2c, red curve).

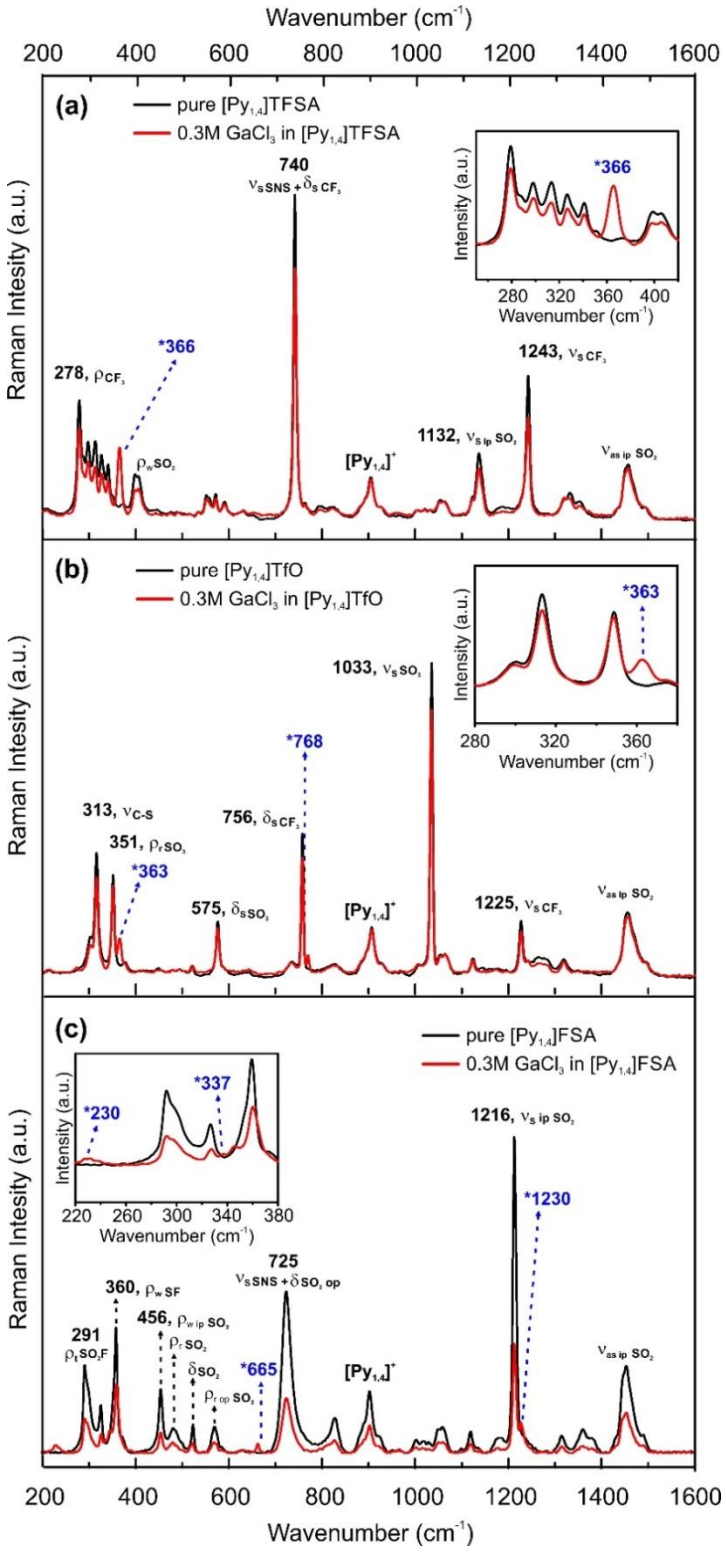

Fig. 7.3.1 *Raman spectra between 200 and 1600 cm^{-1} of (a) [Py$_{1,4}$]TFSA, (b) [Py$_{1,4}$]TfO and (c) [Py$_{1,4}$]FSA in the presence (red) and in the absence (black) of 0.3 M GaCl$_3$. Insets show in (a) Raman spectra between 250 and 420 cm^{-1}, in (b) Raman spectra between 250 and 380 cm^{-1} and in (c) Raman spectra between 220 and 380 cm^{-1}. The peak are assigned based on refs. [239, 241, 250, 251]*

Furthermore, in the presence of $GaCl_3$ two additional peaks are observed at 1062 and 1405 cm^{-1}, which might be associated with the formation of $GaCl_3$-IL species.

Nevertheless, the observed peaks in the described IR regime are mainly due to the response of the ILs. Furthermore, the metal-ligand vibrational stretching frequencies fall below 600 cm^{-1} [252]. Therefore, Far-IR spectroscopy is more suitable to study the structure of molecular addition compounds of metal halides [253]. In addition, the Raman spectra are inconclusive for the structural studies of $GaCl_3$ adducts, because they are either white powders or pale yellow coloured, and such samples are prone to undergo fluorescence. Thus, the Far-IR spectra of the neat ILs and their mixtures with $GaCl_3$ were recorded (fig.7.3.3).

All the spectra related to the neat ILs show quite a broad peak below 100 cm^{-1}, which can be attributed to cation-anion interactions [254]. Besides, only a few low intensity peaks are observed for the employed ILs in this Far-IR region (fig. 7.3.3a-c, black curves). Apparently, all the spectra related to the $GaCl_3$-ILs mixtures exhibit new peaks in two regimes: around 150 cm^{-1} and between 350 and 410 cm^{-1} (figure 7.3.3a-c, red curves). These peaks/shoulders are correlated to species formed by the interaction of $GaCl_3$ with the anions of the ILs. Greenwood et al. [253] investigated the Far-IR spectra and structure of some complexes of gallium trihalides with ligands containing nitrogen, oxygen, and sulfur donor atoms. Furthermore, the positions of the metal-ligand bond vibrations, the strength of the coordinated bond, and the monomeric structure of L-$GaCl_3$ (with a C_{3v} symmetry) have been discussed. The peak positions of L-$GaCl_3$ were noticed at 396 ± 7, 359 ± 2, and 153 ± 3 cm^{-1}, where L represents ligands consisting of the donor atoms viz. nitrogen, oxygen, and sulfur. The peaks at 150, 360, and 396 cm^{-1} have been assigned to the deformation, symmetric stretching, and asymmetric stretching modes of $GaCl_3$ with L [253]. Therefore, in the $GaCl_3$-ILs spectra, the peaks observed at ~150 cm^{-1} can be attributed to complexes of the form $GaCl_3A^-$, where A= $[FSA]^-$, $[TFSA]^-$, and $[TfO]^-$. Moreover, quite a broad peak is noticed at 377 cm^{-1} with shoulders at ~ 355 and ~ 405 cm^{-1} for the liquids with $[FSA]^-$ and $[TfO]^-$. In the case of $[Py_{1,4}]$TFSA, two weak and broad waves were noticed between 360 and 375 cm^{-1}. The discrepancies/shifts in the peak positions could be attributed to the strength of neutral ligands when compared to the anions of the ILs or to the larger mass of the IL anions. Furthermore, the asymmetric stretching modes of the L-$GaCl_3$ shift to low wavenumbers on changing the donor atoms attached to the ligands (O: 412 cm^{-1}, S: 398 cm^{-1}, N: 392 cm^{-1}). However, the symmetric stretching modes are not affected strongly on changing the donor atoms of the ligands [253].

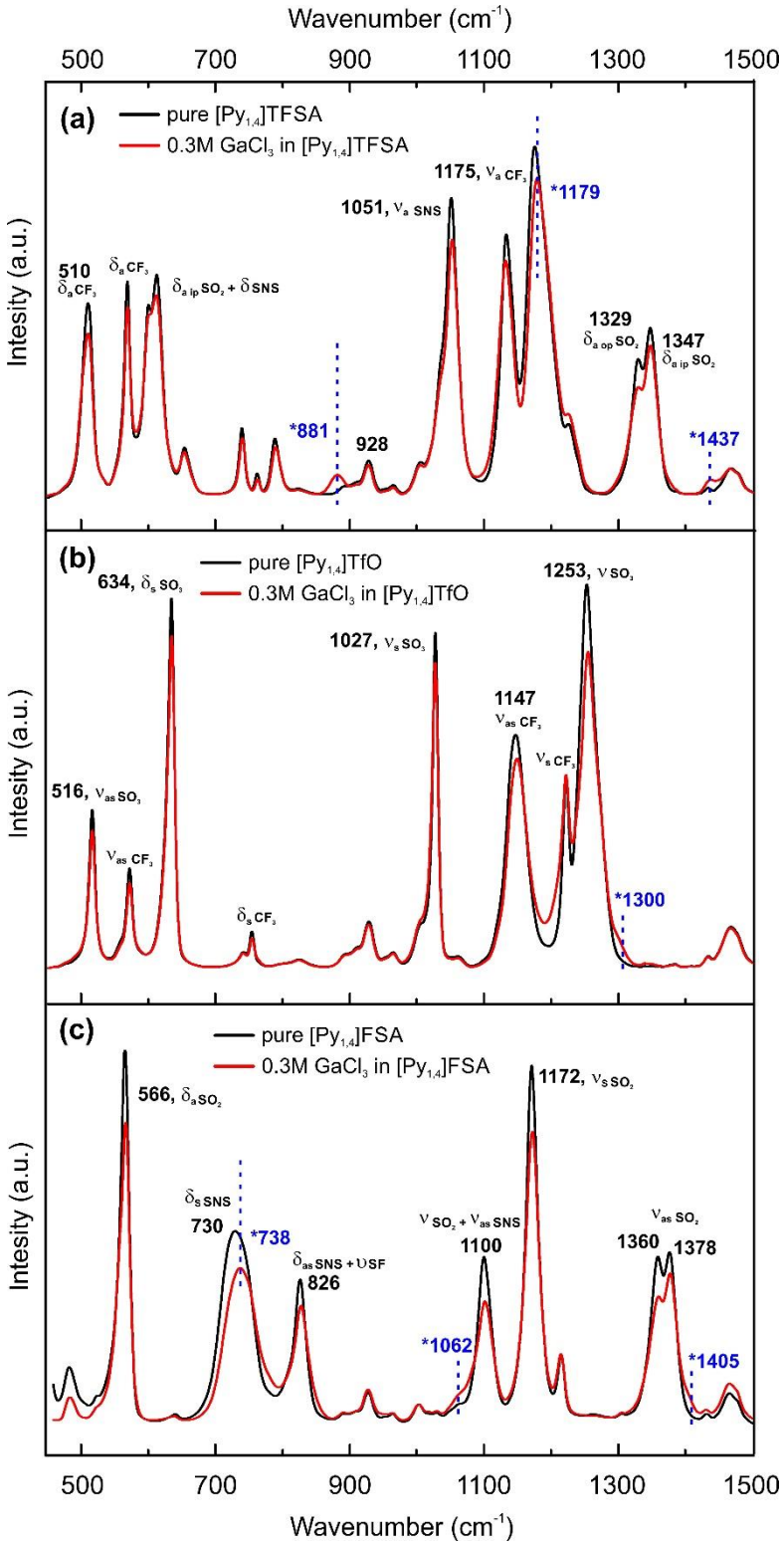

Fig. 7.3.2 *IR spectra between 450 and 1500 cm^{-1} of (a) [Py$_{1,4}$]TFSA, (b) [Py$_{1,4}$]TfO and (c) [Py$_{1,4}$]FSA in the presence (red) and in the absence (black) of 0.3 M GaCl$_3$. The peak are assigned based on refs. [241, 251, 255]*

In summary, few changes have been noticed in the mid-IR region as most of the vibrational modes are solely due to the ions of the ILs, which does not provide reliable information on the coordination of metal ions with anions of ILs. In the Raman spectra,

the intensities of the peaks related to the anions decrease on adding $GaCl_3$ except a few new peaks for all the ILs. Prominent changes are noticed for the mixtures of $GaCl_3$ and ILs in the Far-IR region.

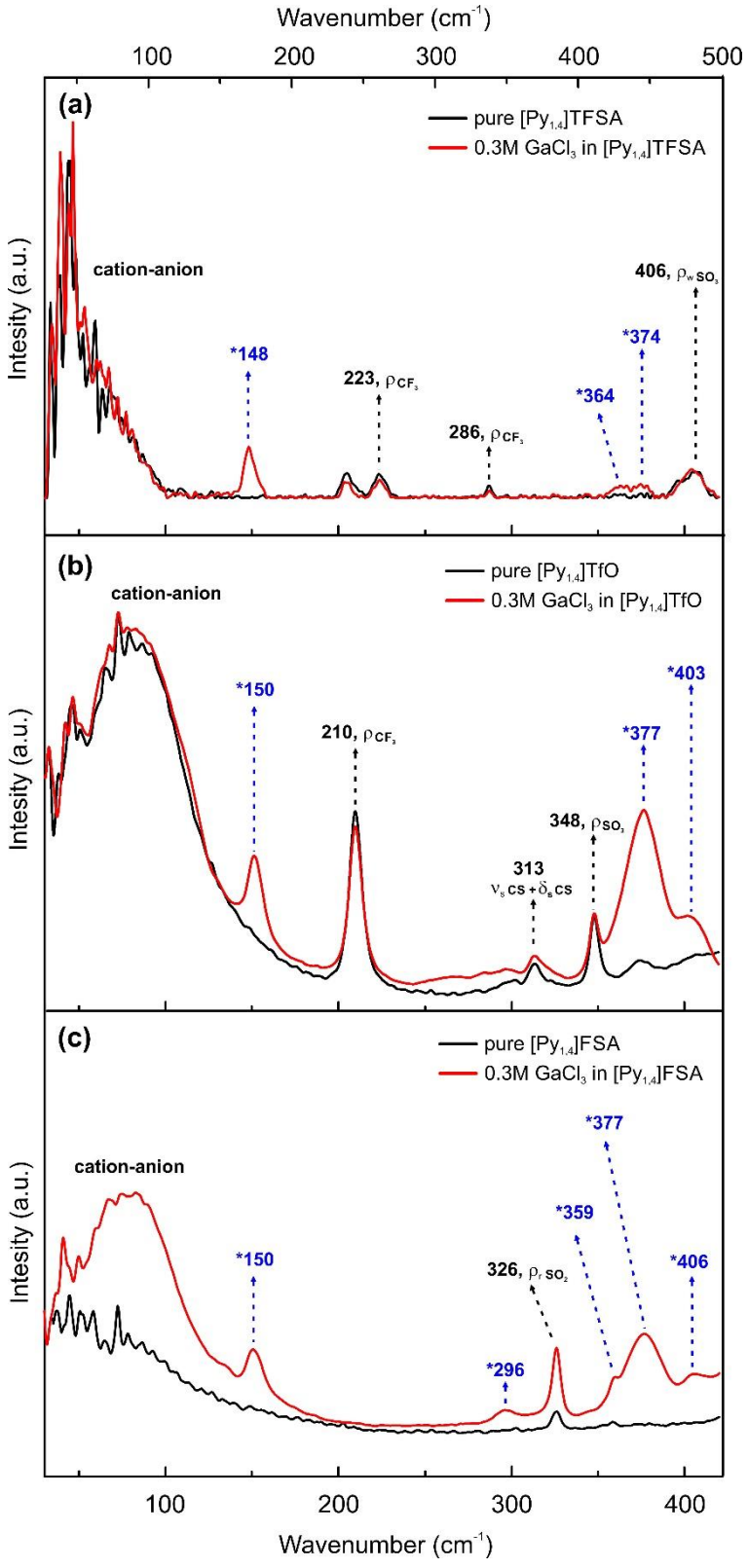

Fig. 7.3.3 *Far-IR spectra of (a) [$Py_{1,4}$]TFSA, (b) [$Py_{1,4}$]TfO and (c) [$Py_{1,4}$]FSA in the presence (red) and in the absence (black) of 0.3 M $GaCl_3$.*

To identify the $GaCl_3$ solvation number in the ILs, the coordination number was evaluated from the Raman spectra in the regions of 740-790 cm^{-1} and 1200-1245 cm^{-1} for $[Py_{1,4}]TfO$ and $[Py_{1,4}]FSA$, respectively. The Raman bands were deconvoluted with Voigt functions as shown in figure 7.3.4. In the case of pure $[Py_{1,4}]TfO$, the symmetric CF_3 bending mode of $[TfO]^-$ consists of only one component (A) at 756 cm^{-1} (fig. 7.3.4a, black curve). Upon addition of 0.3 M $GaCl_3$ an additional component (B) at 768 cm^{-1} occurs, which corresponds to the interaction of the metal salt with the TfO^- anion. In pure $[Py_{1,4}]FSA$ the symmetric SO_2 stretching mode gives a peak at 1216 cm^{-1}, which can be deconvoluted to three components (fig. 7.3.4b, black curve). Components A (at 1216 cm^{-1}) and B (at 1220 cm^{-1}) are the two conformers of the $[FSA]^-$ anion, and peak C (at 1211 cm^{-1}) can be ascribed to the cation [256-258]. On addition of 0.3 M $GaCl_3$ the new components A* (at 1231 cm^{-1}) and B* (at 1235 cm^{-1}) occur, which are both blue shifted by ~ 15 cm^{-1} from the corresponding A and B components (fig. 7.3.4b, red curve). Furthermore, the intensities of A* and B* are 16 % of the intensities of the main A and B components, respectively.

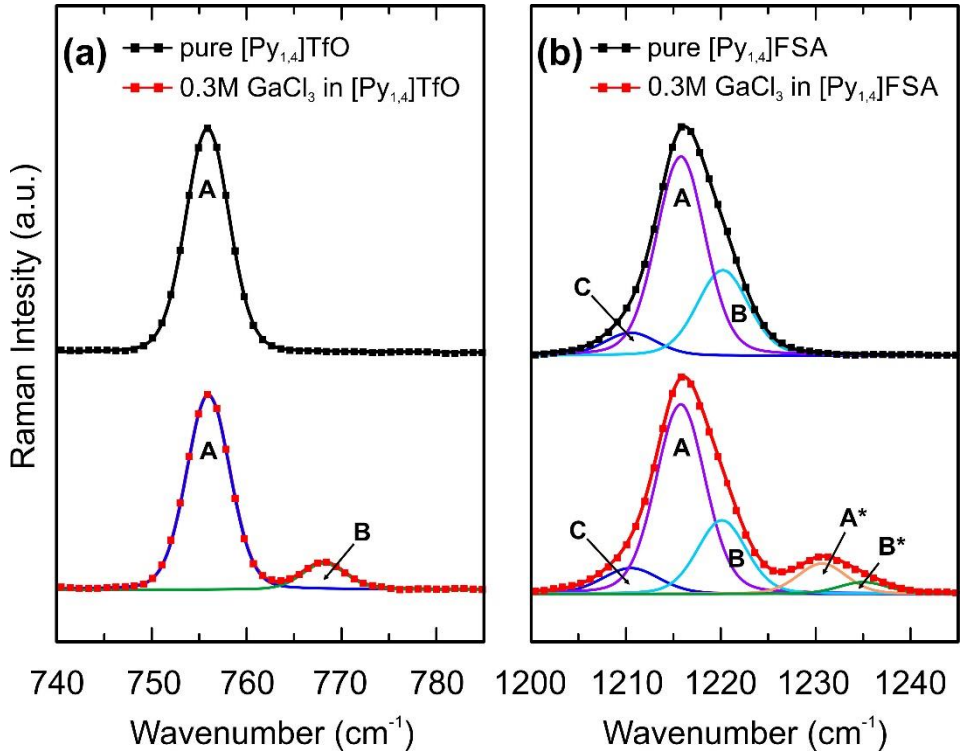

Fig. 7.3.4 *The experimental Raman spectra (dots) and the Voigt fit components of (a) $[Py_{1,4}]TFSA$, (b) $[Py_{1,4}]TfO$ and (c) $[Py_{1,4}]FSA$ in the presence (red) and in the absence (black) of 0.3 M $GaCl_3$.*

From the peak fit analysis, the average coordination number (N) can be obtained by the following equation:

$$N = \frac{\frac{a_{Ga(Co)}}{\left(a_{Ga(Co)} + a_L\right)}}{\frac{n_{GaCl_3}}{\left(n_{GaCl_3} + n_L\right)}} \qquad (7.1)$$

where, $a_{Ga(CO)}$ is the Raman integral intensity of the coordinated Ga^{3+} with ligand, a_L is the Raman integral intensity of the free anions, n_{GaCl3} is the molar concentration of $GaCl_3$ and n_L is the molar concentration of the respective IL.

The $GaCl_3$ solvation number was found to be 1.7 ± 0.2 and 1.8 ± 0.2 for $[TfO]^-$ and $[FSA]^-$, respectively, from which it can be suggested that both $[GaCl_3A]^-$ and $[GaCl_2A_2]^-$ (where A=TfO or FSA) can be present in the solution. However, the formation of $[GaCl_3A]^-$ is evident in all three ILs. Therefore, based on the vibrational spectroscopy results it can be summarized that anionic species of $GaCl_3$ with the respective anions ($[GaCl_xA_y]^-$, where A=TFSA or TfO, x≅3-2 and y≅1-2) might be formed in the ILs.

In situ AFM force-distance measurements were performed to investigate the interfacial structure of the neat ILs and in the presence of $GaCl_3$ in the potential regime between the OCP and prior to the electrodeposition of Ga. Figure 7.3.5 presents the AFM force-distance curves for neat $[Py_{1,4}]$TFSA, $[Py_{1,4}]$TfO and $[Py_{1,4}]$FSA ionic liquids and in the presence of 0.3 M $GaCl_3$ on Au(111) at various electrode potentials. At the applied electrode potentials multiple interfacial layers are present in the case of the pure ILs (fig. 7.3.5, black curves). At the OCP the ILs show similar interfacial behaviour on Au(111) and at least 4 layers can be detected in them (fig. 7.3.5a, d, g). The measured spacing between the layers corresponds well with the diameter of the IL ion pair. The force required to rupture each layer increases as the AFM tip approaches the surface. In the case of $[Py_{1,4}]$FSA a force of about 10 nN is needed to rupture the innermost layer, while in the case of both $[Py_{1,4}]$TFSA and $[Py_{1,4}]$TfO about 5 nN is required, indicating that at the OCP the FSA IL is roughly 2 times more strongly adsorbed on the gold surface than TFSA and TfO ILs.

In general, the interfacial nanostructure of ILs becomes stronger by changing the electrode potential to more negative values. However, significant changes can be noticed in the nanostructure of the IL/Au(111) interface. In the case of $[Py_{1,4}]$TFSA, the innermost layer becomes thinner by reducing the electrode potential (from ~0.55 nm at -0.5 V to ~0.45 nm at -0.8 V) indicating that the cation of the IL adopts an orientation more parallel to the surface (fig. 7.3.5a-c black curves). For $[Py_{1,4}]$TfO and $[Py_{1,4}]$FSA, the width of the innermost layer (~0.7 nm) remains the same in this potential range

(fig. 7.3.5d-i). The force required to rupture the innermost layer increases by reducing the electrode potential for all the ILs. However, in the case of $[Py_{1,4}]FSA$, the force increases markedly indicating the formation of a very strong interfacial nanostructure (at -1.2 V of about 50 nN force is required to rupture the innermost layer) (fig. 7.3.5i, black curve).

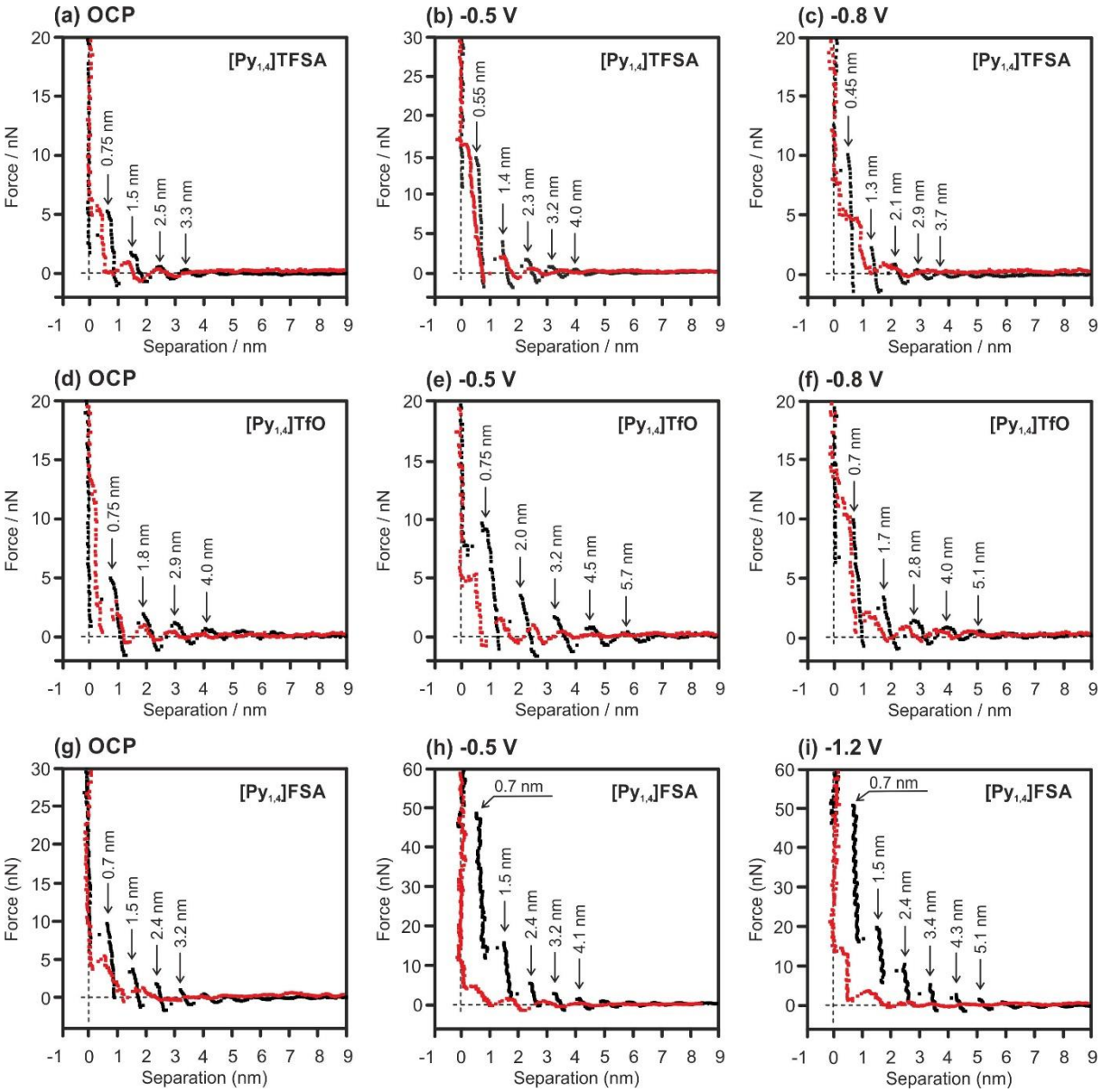

Fig. 7.3.5 *Force-distance profiles for an AFM tip approaching the Au(111) surface in $[Py_{1,4}]$TFSA at (a) OCP, (b) -0.5 V and (c) -1.0 V; in $[Py_{1,4}]$TfO at (d) OCP, (f) -0.5 V and (e) -1.0 V; and in $[Py_{1,4}]$FSA at (g) OCP, (h) -0.5 V and (i) -1.0 V in the presence (red) and in the absence (black) of 0.3 M $GaCl_3$.*

The IL/Au(111) interfacial structure changes significantly on the addition of 0.3 M $GaCl_3$. Spectroscopic data reveals that anionic species $[GaCl_3A]^-$ and $[GaCl_2A_2]^-$ (where A=TFSA, TfO and FSA) might be formed. These anionic species should participate in the formation of the IL/solid interfacial nanostructure and may alter the

electrochemical processes. The force-distance measurements show that the addition of $GaCl_3$ influences the IL/electrode interfacial nanostructure for all three ILs, but the influence is different (fig. 7.3.5, red curves). In the case of $[Py_{1,4}]$TFSA, the interfacial structure becomes even stronger upon addition of 0.3 M $GaCl_3$ (fig. 7.3.5a, b, red curves). At OCP and at -0.5 V the thickness of the innermost layer is ~0.3 nm, but prior to electrodeposition the innermost layer gets thinner (~0.2 nm) and the interfacial structure becomes weaker, as only ~7 nN force is needed to remove the innermost layer at -0.8 V (figure 7.3.5c, red curve). Similar to the $[Py_{1,4}]$TFSA, at OCP an about 0.3 nm thick innermost layer is detected for $GaCl_3$-$[Py_{1,4}]$TfO (fig. 7.3.5d). However, by decreasing the electrode potential the innermost layer gets thicker (~0.5 nm) and the interfacial structure becomes weaker probably due to the reorganization of the electroactive species at the gold surface (fig. 7.3.5e). At -0.8 V (prior to electrodeposition) the innermost layer seems to consist of two sublayers (~0.3 nm each), as two small steps at ~0.3 nm and ~0.6 nm can be identified (fig. 7.3.5f). Furthermore for $[Py_{1,4}]$TfO, the electroactive species is more strongly adsorbed to the electrode surface, wherein ~ 12 nN force is needed to rupture the innermost layer. In the case of $[Py_{1,4}]$FSA, the addition of $GaCl_3$ drastically weakens the interfacial nanostructure (fig. 7.3.5g-i, red curves), as only ~5 nN and ~12 nN force is required to rupture the innermost layer at the OCP/-0.5 V and at -1.2 V, respectively, which is ~4 times smaller compared to ~50 nN force (at -1.2 V) for the pure $[Py_{1,4}]$FSA. For all electrode potentials the thickness of the innermost layer is about 0.5 nm, which corresponds well with the dimensions of the anionic species of Ga.

In situ AFM measurements reveal that the structure of the $GaCl_3$-IL/electrode interface varies for the employed ILs and the anion of the IL has a strong influence on the interfacial nanostructure. Such differences in the adsorption strength of the $GaCl_3$-IL/Au(111) interface can affect the deposition characteristics and control the rate and growth of the Ga deposits.

Figure 7.3.6 shows typical CVs of 0.2 M $GaCl_3$ in $[Py_{1,4}]$TFSA, $[Py_{1,4}]$TfO and $[Py_{1,4}]$FSA on gold at room temperature and the morphology of Ga electrodeposits obtained from these mixtures under similar experimental conditions [229]. The reduction processes at -0.9 V (for $[Py_{1,4}]$TFSA), at -1.1 V (for $[Py_{1,4}]$TfO) and at -1.3 V (for $[Py_{1,4}]$FSA) are attributed to the deposition of Ga (fig.7.3.6a-c). The SEM micrographs show micrometer-thick layers of Ga deposited at -1.3 V for 1 hour (fig. 7.3.6d-f) [229]. The crystal sizes of the obtained deposits varied with the ILs. The deposit made from $[Py_{1,4}]$TFSA consists of spherical structures of 60-260 nm in

diameter (fig.7.3.6d), while the crystal sizes of Ga deposit obtained from $[Py_{1,4}]TfO$ are between 15 and 110 nm (fig. 7.3.6e). In the case of $[Py_{1,4}]FSA$ a nanocrystalline Ga deposit with the crystal size of less than 50 nm is obtained.

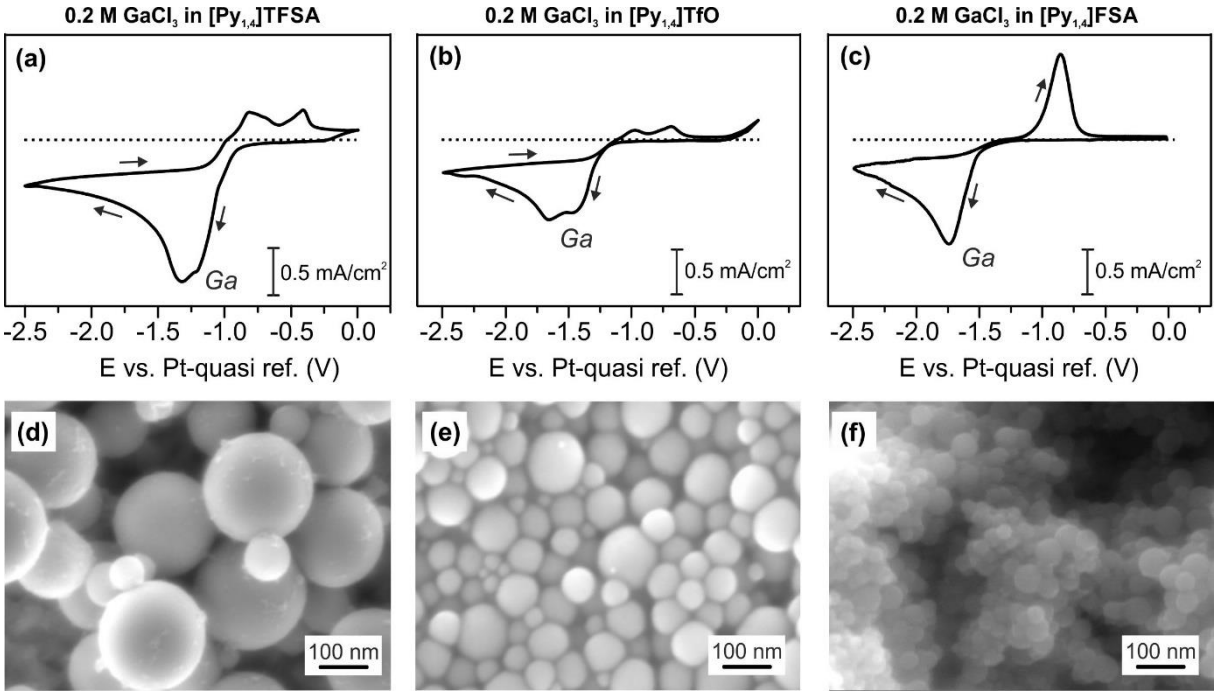

Fig. 7.3.6 *CVs of 0.2 M $GaCl_3$ in (a) $[Py_{1,4}]TFSA$ (b) $[Py_{1,4}]TfO$ and (c) $[Py_{1,4}]FSA$ on polycrystalline Au at RT. SEM images of Ga electrodeposited on Au at -1.3 V for 1 hour at RT from 0.2 M $GaCl_3$ in (d) $[Py_{1,4}]TFSA$ (f) $[Py_{1,4}]TfO$ and (e) $[Py_{1,4}]FSA$. Adapted from ref. [229]*

These results show that the anion of the IL has a strong influence on the IL/Au(111) interface. The addition of $GaCl_3$ in the IL leads to the formation of gallium containing anionic species, which adsorb differently to the gold surface and are reduced at negative electrode potentials resulting in the formation of Ga deposits with different morphology.

7.4 Electrodeposition of GaSb

Gallium antimonide (GaSb) is a direct band gap semiconductor with a band gap of 0.72 eV at room temperature. It is applied in photodetectors operating in infrared region and tunnel diodes. It was shown that GaSb can be directly synthesized at room temperature by galvanic displacement of $SbCl_3$/ionic liquid on electrodeposited Ga, Ga nanowires and on commercial Ga [228, 235]. Initially Ga was electrochemically deposited on copper from $[Py_{1,4}]TFSA$ or [EMIm]TFSA containing $GaCl_3$. Subsequently $SbCl_3$-$[Py_{1,4}]TFSA$ or $SbCl_3$-[EMIm]TFSA electrolyte was applied onto the deposited Ga. It was proposed that a galvanic displacement reaction takes place at the surface leading to coverage of Sb on Ga and formation of GaSb at the interface. The

displacement process continues even after formation of GaSb due to the fast diffusion of Ga through the Sb/GaSb layers. Stopping the process at an appropriate time leads to the formation of a thick layer of GaSb. Figures 7.4.1 and 7.4.2 represent AFM height and deflection images taken at various time intervals during galvanic displacement of Sb on electrodeposited Ga in 25 mM $SbCl_3$-[$Py_{1,4}$]TFSA and 25 mM $SbCl_3$-[EMIm]TFSA, respectively. The measurements were performed using a Cypher S (Asylum Research) AFM inside of a glove box under argon atmosphere.

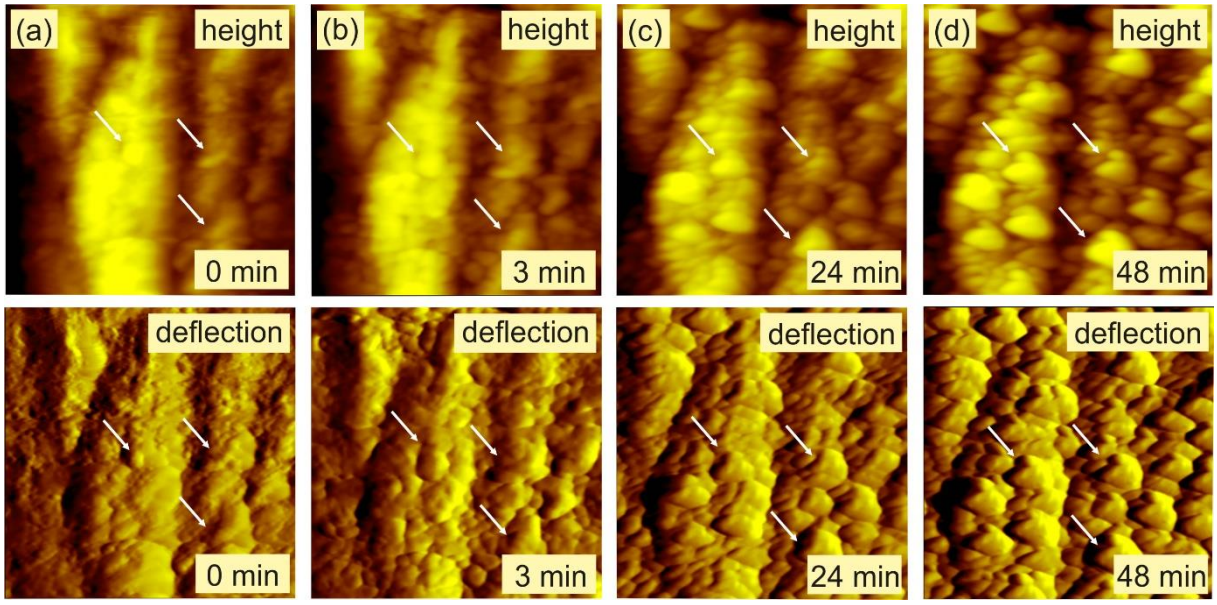

Fig. 7.4.1 *AFM snapshots taken at various time intervals during galvanic displacement of Sb on electrodeposited Ga in 25 mM $SbCl_3$-[$Py_{1,4}$]TFSA, (2 μm $\times$ 2 μm) image. Reproduced from ref. [228]*

The gallium deposit obtained from [$Py_{1,4}$]TFSA consists of spherical nanoparticles in the size range between 40 and 70 nm (fig. 7.4.1a). The particles start to grow rapidly when the ionic liquid containing $SbCl_3$ is placed onto the Ga deposit (fig. 7.4.1b). From the topography and deflection images, one can clearly see the coagulated spherical shapes of the nanoparticles (marked by arrows). With time the formation of triangular plate like structures with sizes of about 250 nm are obtained (fig. 7.4.1c). After 48 minutes of deposition, triangular/heart shaped structures with a size of about 300 nm are observed (fig. 7.4.1d). Similar to [$Py_{1,4}$TFSA, the gallium deposit made in [EMIm]TFSA consists of spherical nanoparticles of 30-60 nm in diameter (fig. 7.4.2a, white arrows) and the particles grow rapidly when the IL containing $SbCl_3$ is applied onto the Ga deposit (fig. 7.4.2b). After 30 min, nanoparticles with a size of about 300 nm can be obtained (fig. 7.4.2c).

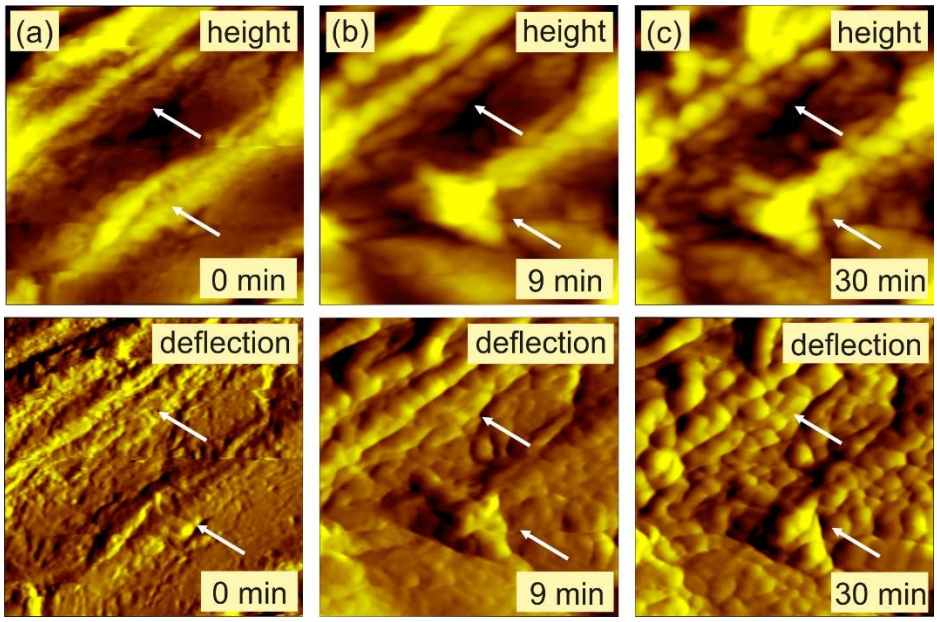

Fig. 7.4.2 *AFM snapshots taken at various time intervals during galvanic displacement of Sb on electrodeposited Ga in 25 mM $SbCl_3$-[EMIm]TFSA, (2 μm $\times$ 2 μm) image. Reproduced from ref. [235]*

XPS, auger electron spectroscopy (AES) and Raman measurements revealed the formation of GaSb in both ILs. However, the direct bandgap was found to be ~0.9 eV and ~1.2 eV for electrodeposits obtained in $[Py_{1,4}]$TFSA and [EMIm]TFSA, respectively [228]. This indicates that the deposit property was influenced by the IL cation due to the change in the reaction kinetics. Thus the properties of the obtained electrodeposits can be tuned by varying the IL chemical structure, which opens perspectives to produce materials with tailor-made properties.

8 Conclusions

Ionic liquids are an innovative class of materials that are of technological interest due to their attractive properties. They are potential materials to replace traditional molten salts and classical molecular solvents in various industrial processes. Many technological processes take place at the IL/solid interface, where charge transfer and mass transfer occur. The structure and properties of the IL/solid interfaces play an important role in many applications and therefore a deep understanding of the IL/solid interface is an essential prerequisite for further development and widespread use of ILs.

In this thesis the structure of the electrified IL/solid interface was investigated using *in situ* STM and AFM, which reveal details of the IL EDL structure down to the molecular level (Chapter 5). Various ILs, namely [$Py_{1,4}$]TFSA, [$Py_{1,4}$]FAP, [$Py_{1,4}$]FSA, [$Py_{1,4}$]TfO, [EMIm]TFSA, [OMIm]TFSA, [EMIm]FAP and [HMIm]FAP were examined. It was found that ILs behave very differently to common molecular solvents: the IL/solid interface is more complex compared to conventional aqueous electrolytes. This remarkable difference is ascribed to higher adsorption strength of ILs onto solid surfaces compared to typical organic solvents or water. The force-separation profiles reveal that multiple interfacial layers are present at the IL/solid interface. The number of solvation layers depends on applied electrode potential. Larger applied potential leads to a stronger interfacial nanostructure: both the number of solvation layers and the forces required to rupture these layer increase with increasing the electrode potential. Furthermore, higher surface potential results in stronger electrostatic interactions with the innermost (Stern) layer that produce more enriched, more compact and more tightly bound ion layer closest to the surface. Moreover, the applied potential determines whether cations (cathodic regime) or anions (anodic regime) are preferentially adsorbed to the surface. The ions in the innermost layer interact with the surface, leading to a surface restructuring/reconstruction and/or formation of various, sometimes “unusual” overstructures, which can be displayed with *in situ* STM and AFM.

In situ STM measurements show that the appearance of the Au(111) surface is different in the employed ILs (Chapter 5.1). Both the IL cation and the IL anion have a strong influence on the structure and composition of the IL/Au(111) interface. A Au(111) surface restructuring was obtained in all ILs used in this study, however the

appearance of the gold surface differs in these ILs and depends on the applied electrode potential. Thus, with the same anion, the Au(111) surface undergoes the (22 x √3) reconstruction with $[Py_{1,4}]^+$, but with $[EMIm]^+$, $[HMIm]^+$ and $[OMIm]^+$ the herringbone superstructure pattern was not obtained, as a particular configuration of $[Py_{1,4}]^+$ during cathodic polarization causes the Au(111) (22 x √3) reconstruction.

The presence of such strongly adsorbed ions layers influences the STM and AFM image quality, as the tip cannot displace the ion layers and directly probe the surfaces. Thus, it is difficult to probe the HOPG surface with atomic resolution in [OMIm]TFSA at all electrode potentials (Chapter 5.2). However, close to the cathodic limit of the electrochemical window of [OMIm]TFSA different superstructures with lateral sizes between 1.2 and 1.7 nm are observed with *in situ* STM, as a result of several cation and/or anion layers probed at the same time by the STM tip.

In general, solutes dissolved in ILs alter the existing IL/solid interfacial nanostructure (Chapter 6). However, various solutes have a different influence on the structure of the IL/solid interface. Thus, in the case of $[Py_{1,4}]$FAP containing LiCl or $SiCl_4$, the presence of Li^+ and Si(IV) ions affects interactions between $[Py_{1,4}]^+$ and the gold surface (Chapter 6.1). At negative electrode potentials these cations are present at the IL/Au(111) interface together with $[Py_{1,4}]^+$ reducing the interfacial structure and hindering the Au(111) (22 x √3) surface reconstruction that results in an incomplete reconstruction of the Au(111) surface during cathodic polarization probed by *in situ* STM. However, the addition of TaF_5 does not significantly alter the $[Py_{1,4}]$FAP/Au(111) interfacial structure and the complete herringbone reconstruction of the gold surface is obtained. In the case of $GaCl_3$, the IL/Au(111) interface modifies upon addition of 0.3 M $GaCl_3$ (Chapter 7.3). However, the ions arrangement at the gold surface is different in $[Py_{1,4}]$TFSA, $[Py_{1,4}]$TfO and $[Py_{1,4}]$FSA.

The concentration of added solute has also a strong influence on the electrified IL/solid interface (Chapter 6.1). *In situ* AFM measurements reveal that the addition of high concentrations of NaFSA and LiTFSA has a stronger influence on the structure of IL/Au(111) interface in $[Py_{1,4}]$FSA and $[Py_{1,4}]$TFSA, respectively, as during cathodic polarization the $[Py_{1,4}]^+$ ions are replaced by Na^+ or Li^+ at the interface reducing the IL/surface interfacial nanostructure. In the case of water, the typical multilayered IL/Au(111) structure exists up to 30 vol% water in [EMIm]TfO. Above 50 vol% of water only one well-ordered (Stern) layer dominated by the hydrated $[EMIm]^+$ is detected at the interface. Furthermore, between 30 vol% and 50 vol% of water in the [EMIm]TfO there is a clear transition from a multilayered interfacial structure typical for the pure IL

to a classical double layer structure as it has been known for aqueous electrolytes. The formation of a double layer structure occurs during cathodic polarization of the $[Py_{1,4}]$FAP/Au(111) interface in the presence of 0.25 M $SiCl_4$ (Chapter 7.2).

In the case of [EMIm]TFSA, AFM measurements shows that an ordered structure with a lateral dimension of 3.8 nm is present at the H-terminated p-Si(111) surface, which is much larger than the dimension of the IL cation, anion, or ion pair (Chapter 6.2). Interestingly in contrast to the Au(111) surface, the interfacial structures are much stronger for [EMIm]TFSA than for $[Py_{1,4}]$TFSA on H-Si(111). The addition of 0.1 M LiTFSA weakens the interfacial nanostructure for both ILs.

The *in situ* AFM and STM studies clearly show that the structure of the IL/solid interface has a significant influence on electrodeposition processes (Chapter 7). Thus, elemental Ta can be electrodeposited in $[Py_{1,4}]$TFSA containing 0.1 M TaF_5, whereas under similar experimental conditions *in situ* STM does not indicate any tantalum deposition in $[Py_{1,4}]$FAP containing 0.1 M TaF_5 (Chapter 7.1). *In situ* AFM reveals that $[TFSA]^-$ interacts differently with TaF_5 than $[FAP]^-$. Force-distance measurements elucidate that TaF_5 is expelled from the electrode surface in $[Py_{1,4}]$FAP, while in $[Py_{1,4}]$TFSA the interfacial nanostructure is disturbed by the addition of TaF_5.

In situ STM shows that a semiconducting Si layer can be deposited in both $[Py_{1,4}]$TFSA and $[Py_{1,4}]$FAP containing 0.1 M $SiCl_4$ (Chapter 7.2). However, the difference for Si deposition is roughly 1 V. Furthermore, increasing the concentration of $SiCl_4$ to 0.25 M in $[Py_{1,4}]$FAP leads to the formation of a double layer structure at the IL/Au(111) interface, which in turn facilitates the electrodeposition of Si.

The structure of the IL/Au(111) interface has a strong influence on the quality and morphology of electrodeposited Ga (Chapter 7.3). The electrodeposition of Ga was studied in $[Py_{1,4}]$TFSA, $[Py_{1,4}]$TfO and $[Py_{1,4}]$FSA containing 0.3 M $GaCl_3$. Raman and IR spectroscopy reveal that $GaCl_3$ interacts with the ILs leading to the formation of $[GaCl_xA_y]^-$ (where A=TFSA, TfO or FSA) anionic species. The force-distance profiles show that the applied electrode potential has an influence on the structure of the $GaCl_3$-IL/Au(111) interface leading to the reorganization of the electroactive species at the surface. The crystal sizes of the electrodeposited Ga varies upon changing the ILs. The deposit made from $[Py_{1,4}]$TFSA consists of spherical structures of 60-260 nm in diameter, while the crystal sizes of the Ga deposit obtained from $[Py_{1,4}]$TfO are between 15 and 110 nm. In the case of $[Py_{1,4}]$FSA a nanocrystalline Ga deposit with a crystal size of less than 50 nm is obtained.

Furthermore, it was shown that the optical properties of GaSb can be influenced by the applied IL (Chapter 7.4). GaSb obtained by galvanic displacement of $SbCl_3$-[$Py_{1,4}$]TFSA on electrodeposited Ga exhibits a band gap of 0.9 eV, while GaSb synthesized from $SbCl_3$-[EMIm]TFSA shows a band gap of 1.2 eV. It indicates that the IL can influence the optical properties of the obtained semiconductor.

Based on aforementioned results the following general conclusions can be drawn:

- ILs exhibits a remarkably diverse interfacial chemistry, with multiple interfacial layers present at the IL/solid interface.
- The adsorption strength of ILs onto solid surfaces is much higher than for typical organic solvents or water.
- Solutes have a strong influence on the IL/solid interfacial nanostructure.
- The structure and composition of the interfacial layer can be tuned by varying the surface potential, the ionic structure and by addition of solutes.
- The structure of the IL/electrode interface influences the electrochemical processes that in turn can alter the quality and properties of the obtained metals and semiconductors.

These effects are unique for each IL and therefore cannot be generalized, if at all. An understanding of such interfacial and solvation effects is challenging and opens new possibilities to the design of the IL/solid interface with required properties, which could impact a diverse range of electrochemical applications.

9 References

[1] N. Borisenko, *STM supported electrodeposition in air and water stable ionic liquids: Silicon, selenium and poly(para)phenylene*. 2007, Clausthal-Zellerfeld: Papierflieger.

[2] T. Welton, *Room-temperature ionic liquids. Solvents for synthesis and catalysis.* Chem. Rev., 1999. **99**(8): p. 2071-2084.

[3] J. P. Hallett, T. Welton, *Room-temperature ionic liquids: Solvents for synthesis and catalysis. 2.* Chem. Rev., 2011. **111**(5): p. 3508-3576.

[4] N. V. Plechkova, K. R. Seddon, *Applications of ionic liquids in the chemical industry.* Chem. Soc. Rev., 2008. **37**(1): p. 123-150.

[5] D. Pletcher, F. P. Walsh, *Industrial electrochemistry*. Second edition ed. 1993, Glasgow, New York, Tokyo, Melbourne, Madras: Blackie Academic & Professional.

[6] P. Wasserscheid, T. Welton, *Ionic liquids in synthesis*. Vol. 1. 2007, Weinheim: WILEY-VCH Verlag GmbH & Co.KGaA.

[7] P. Walden, *Ueber die Molekulargrösse und elektrische Leitfähigkeit einiger geschmolzenen Salze.* Bull. Acad. Imp. Sci. St.-Pétersbourg, 1914. **8**(6): p. 405-422.

[8] S. Gabriel, J. Weiner, *Ueber einige Abkömmlinge des Propylamins.* Ber. Dtsch. Chem. Ges., 1888. **21**(2): p. 2669-2679.

[9] J. S. Wilkes, *A short history of ionic liquids-from molten salts to neoteric solvents.* Green Chem., 2002. **4**(2): p. 73-80.

[10] C. Graenacher, *Cellulose solution*. 1934: US Patent.

[11] F. H. Hurley, *Electrodeposition of aluminium*. 1948: US Patent.

[12] T. P. Wier, F. H. Hurley, *Electrodeposition of aluminium*. 1948: US Patent.

[13] F. H. Hurley, T. P. Wier, *The electrodeposition of aluminum from nonaqueous solutions at room temperature.* J. Electrochem. Soc., 1951. **98**(5): p. 207-212.

[14] J. T. Yoke, J. F. Weiss, G. Tollin, *Reactions of triethylamine with copper(I) and copper(II) halides.* Inorg. Chem., 1963. **2**(6): p. 1210-1216.

[15] H. L. Chum, V. R. Koch, L. L. Miller, R. A. Osteryoung, *Electrochemical scrutiny of organometallic iron complexes and hexamethylbenzene in a room temperature molten salt.* J. Am. Chem. Soc., 1975. **97**(11): p. 3264-3265.

[16] J. Robinson, R. A. Osteryoung, *An electrochemical and spectroscopic study of some aromatic hydrocarbons in the room temperature molten salt system aluminum chloride-n-butylpyridinium chloride.* J. Am. Chem. Soc., 1979. **101**(2): p. 323-327.

[17] J. S. Wilkes, J. A. Levisky, R. A. Wilson, C. L. Hussey, *Dialkylimidazolium chloroaluminate melts: A new class of room-temperature ionic liquids for electrochemistry, spectroscopy and synthesis.* Inorg. Chem., 1982. **21**(3): p. 1263-1264.

[18] T. B. Scheffler, C. L. Hussey, K. R. Seddon, C. M. Kear, P. D. Armitage, *Molybdenum chloro complexes in room-temperature chloroaluminate ionic liquids: stabilization of hexachloromolybdate(2-) and hexachloromolybdate(3-).* Inorg. Chem., 1983. **22**(15): p. 2099-2100.

[19] D. Appleby, C. L. Hussey, K. R. Seddon, J. E. Turp, *Room-temperature ionic liquids as solvents for electronic absorption spectroscopy of halide complexes.* Nature, 1986. **323**: p. 614-616.

[20] C. L. Hussey, *Room temperature molten salts systems*, in *Advances in molten salt chemistry*, G. Mamantov, Editor. 1983, Elsevier: New York. p. 185-230.

[21] T. Tsuda, G. R. Stafford, C. L. Hussey, *Review-Electrochemical surface finishing and energy storage technology with room-temperature haloaluminate ionic liquids and mixtures.* J. Electrochem. Soc., 2017. **164**(8): p. H5007-H5017.

[22] H. A. Oye, M. Jagtoyen, T. Oksefjell, J. S. Wilkes, *Vapour pressure and thermodynamics of the system 1-methyl-3-ethyl-imidazolium chloride-aluminium chloride.* Mater. Sci. Forum, 1991. **73-75**: p. 183-190.

[23] P. Koronaios, D. King, R. A. Osteryoung, *Acidity of neutral buffered 1-ethyl-3-methylimidazolium chlorid-$AlCl_3$ ambient-temperature molten salts.* Inorg. Chem., 1998. **37**(8): p. 2028-2032.

[24] J. S. Wilkes, M. J. Zaworotko, *Air and water stable 1-ethyl-3-methylimidazolium based ionic liquids.* J. Chem. Soc., Chem. Commun., 1992(13): p. 965-967.

[25] P. A. Z. Suarez, J. E. L. Dullius, S. Einloft, R. F. De Souza, J. Dupont, *The use of new ionic liquids in two-phase catalytic hydrogenation reaction by rhodium complexes.* Polyhedron, 1996. **15**(7): p. 1217-1219.

[26] P. Bonhôte, A.-P. Dias, N. Papageorgiou, K. Kalyanasundaram, M. Grätzel, *Hydrophobic, highly conductive ambient-temperature molten salts.* Inorg. Chem., 1996. **35**(5): p. 1168-1178.

[27] D. R. MacFarlane, P. Meakin, J. Sun, N. Amini, M. Forsyth, *Pyrrolidinium imides: A new family of molten salts and conductive plastic crystal phases.* J. Phys. Chem. B, 1999. **103**(20): p. 4164-4170.

[28] H. Ohno, *Electrochemical aspects of ionic liquids*. 2005: John Wiley & Sons, Inc., Hoboken, New Jersey.

[29] F. Endres, A. Abbott, D. R. MacFarlane, *Electrodeposition from Ionic Liquids. 2nd Edition*. 2017, Weinheim: Wiley-VCH Verlag GmbH & Co. KGaA.

[30] M. Watanabe, M. L. Thomas, S. Zhang, K. Ueno, T. Yasuda, K. Dokko, *Application of ionic liquids to energy storage and conversion materials and devices.* Chem. Rev., 2017. **117**(10): p. 7190-7239.

[31] K. S. Egorova, E. G. Gordeev, V. P. Ananikov, *Biological activity of ionic liquids and their application in pharmaceutics and medicine.* Chem. Rev., 2017. **117**(10): p. 7132-7189.

[32] C. Dai, J. Zhang, C. Huang, Z. Lei, *Ionic liquids in selective oxidation: Catalysts and solvents.* Chem. Rev., 2017. **117**(10): p. 6929-6983.

[33] A. A. J. Torriero, *Electrochemistry in ionic liquids. Volume 2: Applications*. 2015, Cham, Heidelberg, New York, Dordrecht, London: Springer International Publishing.

[34] B. Kirchner, *Ionic liquids*. Topics in current chemistry. 2010, Berlin Heidelberg: Springer-Verlag Berlin Heidelberg.

[35] D. R. MacFarlane, M. Kar, J. M. Pringle, *Fundamentals of ionic liquids: From chemistry to applications*. 2017, Weinheim: Wiley-VCH Verlag GmbH & Co. KGaA

[36] J. Dupont, L. Kollar, *Ionic liquids (ILs) in organometallic catalysis*. Topics in organometallic chemistry. 2015, Berlin Heidelberg: Springer-Verlag Berlin Heidelberg.

[37] P. Wasserscheid, W. Keim, *Ionic liquids - new "solutions" for transition metal catalysis.* Angew. Chem. Int. Edit., 2000. **39**(21): p. 3772-3789.

[38] S. Forsyth, J. Golding, D. R. MacFarlane, M. Forsyth, *N-methyl-N-alkylpyrrolidinium tetrafluoroborate salts: ionic solvents and solid electrolytes.* Electrochim. Acta, 2001. **46**(10): p. 1753-1757.

[39] J. D. Holbrey, K. R. Seddon, *The phase behaviour of 1-alkyl-3-methylimidazolium tetrafluoroborates; Ionic liquids and ionic liquid crystals.* J. Chem. Soc., Dalton Trans., 1999(13): p. 2133-2140.

[40] D. R. MacFarlane, J. M. Pringle, K. M. Johansson, S. A. Forsyth, M. Forsyth, *Lewis base ionic liquids.* Chem. Commun., 2006(18): p. 1905-1917.

[41] M. J. Earle, J. M. S. S. Esperança, M. A. Gilea, J. N. Canongia Lopes, L. P. N. Rebelo, J. W. Magee, K. R. Seddon, J. A. Widegren, *The distillation and volatility of ionic liquids.* Nature, 2006. **439**: p. 831-834.

[42] P. M. Dean, J. M. Pringle, D. R. MacFarlane, *Structural analysis of low melting organic salts: Perspectives on ionic liquids.* Phys. Chem. Chem. Phys., 2010. **12**(32): p. 9144-9153.

[43] A. Noda, K. Hayamizu, M. Watanabe, *Pulsed-gradient spin-echo 1H and 19F NMR ionic diffusion coefficient, viscosity, and ionic conductivity of non-chloroaluminate room-temperature ionic liquids.* J. Phys. Chem. B, 2001. **105**(20): p. 4603-4610.

[44] K. Tochigi, H. Yamamoto, *Estimation of ionic conductivity and viscosity of ionic liquids using a QSPR model.* J. Phys. Chem. C, 2007. **111**(43): p. 15989-15994.

[45] S. Carda-Broch, A. Berthod, D. W. Armstrong, *Solvent properties of the 1-butyl-3-methylimidazolium hexafluorophosphate ionic liquid.* Anal. Bioanal. Chem., 2003. **375**(2): p. 191-199.

[46] K. R. Seddon, A. Stark, M. Torres, *Influence of chloride, water, and organic solvents on the physical properties of ionic liquids.* Pure Appl. Chem., 2000. **72**(12): p. 2275-2287.

[47] O. O. Okoturo, T. J. VanderNoot, *Temperature dependence of viscosity for room temperature ionic liquids.* J. Electroanal. Chem., 2004. **568**: p. 167-181.

[48] K. N. Marsh, J. A. Boxall, R. Lichtenthaler, *Room temperature ionic liquids and their mixtures - A review.* Fluid Phase Equilib., 2004. **219**(1): p. 93-98.

[49] R. Hagiwara, K. Matsumoto, Y. Nakamori, T. Tsuda, Y. Ito, H. Matsumoto, K. Momota, *Physicochemical properties of 1,3-dialkylimidazolium fluorohydrogenate room-temperature molten salts.* J. Electrochem. Soc., 2003. **150**(12): p. D195-D199.

[50] C. Chiappe, M. Malvaldi, C. S. Pomelli, *Ionic liquids: Solvation ability and polarity.* Pure Appl. Chem., 2009. **81**(4): p. 767-779.

[51] A. J. Bard, L. R. Faulkner, *Electrochemical methods. Fundamentals and applications. 2nd edition*. 2001, Hoboken: John Wiley&Sons, Inc.

[52] E. Meyer, H. J. Hug, R. Bennewitz, *Scanning probe microscopy. The lab on a tip.* Advanced Texts in Physics. 2004, Berlin, Heidelberg, New York: Springer-Verlag Berlin Heidelberg New York.

[53] B. Voigtlaender, *Scanning probe microscope*. NanoScience and Technology. 2015, Berlin, Heidelberg, New York Springer-Verlag Berlin Heidelberg.

[54] R. Hayes, G. G. Warr, R. Atkin, *Structure and nanostructure in ionic liquids.* Chem. Rev., 2015. **115**(13): p. 6357-6426.

[55] A. A. Tseng, Z. Li, *Manipulations of atoms and molecules by scanning probe microscopy.* J. Nanosci. Nanotechnol., 2007. **7**(8): p. 2582-2595.

[56] O. Custance, R. Perez, S. Morita, *Atomic force microscopy as a tool for atom manipulation.* Nat. Nanotechnol., 2009. **4**: p. 803-810.

[57] M. Gerhard, R. Jascha, Z. Sven, B. Kai-Felix, H. Saw Wai, F. Stefan, B. Ludwig, M. Francesca, R. Karl Heinz, *Controlled manipulation of atoms and small molecules with a low temperature scanning tunneling microscope.* Single Molecules, 2000. **1**(1): p. 79-86.

[58] G. Binnig, H. Rohrer, *Scanning tunneling microscopy.* Helv. Phys. Acta, 1982. **55**: p. 726-735.

[59] G. Binnig, H. Rohrer, *Scanning tunneling microscopy-from birth to adolescence (Nobel lecture).* Angew. Chem. Int. Edit., 1987. **26**(7): p. 606-614.

[60] C. Bai, *Scanning tunneling microscopy and its applications*. 2000, Berlin, Heidenberg, New York: Springer-Verlag Berlin Heidelberg.

[61] P. Atkins, J. de Paula, *Atkin's physical chemistry. Seventh edition*. 2002, New York: Oxford University Press Inc.

[62] D. Drakova, *Theoretical modelling of scanning tunnelling microscopy, scanning tunnelling spectroscopy and atomic force microscopy.* Rep. Prog. Phys., 2001. **64**(2): p. 205-290.

[63] J. Tersoff, D. R. Hamann, *Theory and application for the scanning tunneling microscope.* Phys. Rev. Lett., 1983. **50**(25): p. 1998-2001.

[64] J. Tersoff, D. R. Hamann, *Theory of the scanning tunneling microscope.* Phys. Rev. B, 1985. **31**(2): p. 805-813.

[65] J. Bardeen, *Tunnelling from a many-particle point of view.* Phys. Rev. Lett., 1961. **6**(2): p. 57-59.

[66] S. H. Cohen, M. L. Lightbody, *Atomic force microscopy/scanning tunneling microscopy*. 1999, New York, Boston, Dordrecht, London, Moscow: Kluwer Academic/Plenum Publishers.

[67] D. Bonnell, *Scanning probe microscopy and spectroscopy. Theory, techniques, and applications. Second edition*. 2001: Wiley-VCH.

[68] T. P. Moffat, *Scanning tunneling microscopy studies of metal electrodes*, in *Electroanalytical chemistry. A series of advances*, A. J. Bard, I. Rubinstein, Editors. 1999, Marcel Dekker, Inc.: New York, Basel. p. 221.

[69] J. Halbritter, G. Repphun, S. Vinzelberg, G. Staikov, W. J. Lorenz, *Tunneling mechanisms in electrochemical STM - Distance and voltage tunneling spectroscopy.* Electrochim. Acta, 1995. **40**(10): p. 1385-1394.

[70] J. Halbritter, *Tunnel channels, spectroscopy and imaging in STM.* Appl. Phys. A, 1998. **66**(1): p. S181-S186.

[71] G. Repphun, J. Halbritter, *Tunnel channels, charge transfer, and imaging mechanisms in scanning tunneling microscopy.* J. Vac. Sci. Technol. A: Vac. Surf. Films, 1995. **13**(3): p. 1693-1698.

[72] R. Wen, B. Rahn, O. M. Magnussen, *Potential-dependent adlayer structure and dynamics at the ionic liquid/Au(111) interface: A molecular-scale in situ video-STM study.* Angew. Chem. Int. Edit., 2015. **54**(20): p. 6062-6066.

[73] R. Wen, B. Rahn, O. M. Magnussen, *In situ video-STM study of adlayer structure and surface dynamics at the ionic liquid/Au (111) interface.* J. Phys. Chem. C, 2016. **120**(29): p. 15765-15771.

[74] V. Hoffmann, A. Lahiri, N. Borisenko, T. Carstens, G. Pulletikurthi, A. Borodin, R. Atkin, F. Endres, *Nanostructure of the H-terminated p-Si(111)/ionic liquid interface and the effect of added lithium salt.* Phys. Chem. Chem. Phys., 2017. **19**(1): p. 54-58.

[75] H. Li, T. Carstens, A. Elbourne, N. Borisenko, R. Gustus, F. Endres, R. Atkin, *Ionic liquid - solid interfaces*, in *Electrodeposition from ionic liquids. 2nd edition*, F. Endres, A. Abbott, D. R. MacFarlane, Editors. 2017, Wiley-VCH Verlag GmbH & Co. KGaA: Weinheim. p. 321-343.

[76] N. Borisenko, R. Atkin, F. Endres, *Influence of molecular organization of ionic liquids on electrochemical properties.* Electrochem. Soc. Interface, 2014. **23**(1): p. 59-63.

[77] G. Binnig, C. F. Quate, C. Gerber, *Atomic force microscope.* Phys. Rev. Lett., 1986. **56**(9): p. 930-933.

[78] Y. Martin, C. C. Williams, H. K. Wickramasinghe, *Atomic force microscope-force mapping and profiling on a sub 100-Å scale.* J. Appl. Phys., 1987. **61**(10): p. 4723-4729.

[79] Q. Zhong, D. Inniss, K. Kjoller, V. B. Elings, *Fractured polymer/silica fiber surface studied by tapping mode atomic force microscopy.* Surf. Sci. Lett., 1993. **290**(1): p. L688-L692.

[80] J. N. Israelachvili, *Intermolecular and surface forces (third edition)*. 2011, San Diego: Academic Press.

[81] S. Morita, F. J. Giessibl, R. Wiesendanger, *Noncontact atomic force microscopy*. Vol. 2. 2009, Berlin Heidelberg: Springer Verlag.

[82] M. V. Fedorov, A. A. Kornyshev, *Ionic liquids at electrified interfaces.* Chem. Rev., 2014. **114**(5): p. 2978-3036.

[83] M. A. Gebbie, A. M. Smith, H. A. Dobbs, A. A. Lee, G. G. Warr, X. Banquy, M. Valtiner, M. W. Rutland, J. N. Israelachvili, S. Perkin, R. Atkin, *Long range electrostatic forces in ionic liquids.* Chem. Commun., 2017. **53**(7): p. 1214-1224.

[84] F. L. Leite, L. H. C. Mattoso, O. N. Oliveira Jr, P. S. P. Herrmann Jr, *The atomic force spectroscopy as a tool to investigate surface forces: Basic principles and applications* in *Modern research and educational topics in microscopy: Applications in physical/chemical sciences, techniques*, A. Méndez-Vilas, J. Díaz, Editors. 2007, Formatex. p. 747-757.

[85] P. Eaton, P. West, *Atomic force microscopy*. 2010, New York: Oxford University Press Inc.

[86] T. J. Senden, *Force microscopy and surface interactions.* Curr. Opin. Colloid Interface Sci., 2001. **6**(2): p. 95-101.

[87] R. G. Horn, D. F. Evans, B. W. Ninham, *Double-layer and solvation forces measured in a molten salt and its mixtures with water.* J. Phys. Chem., 1988. **92**(12): p. 3531-3537.

[88] H. Sun, B. Qiao, D. Zhang, C. Liu, *Structure of 1-butylpyridinium tetrafluoroborate ionic liquid: Quantum chemistry and molecular dynamic simulation studies.* J. Phys. Chem. A, 2010. **114**(11): p. 3990-3996.

[89] L. G. Gouy, *Sur la constitution de la charge électrique à la surface d'un electrolyte.* J. Phys. Theor. Appl., 1910. **9**(1): p. 457-468.

[90] D. L. Chapman, *LI. A contribution to the theory of electrocapillarity.* Philos. Mag. Series 6, 1913. **25**(148): p. 475-481.

[91] O. Z. Stern, *Zur Theorie der elektrolytischen Doppelschicht.* Z. Elektrochem. Angew. Phys. Chem., 1924. **30**(21-22): p. 508-516.

[92] V. Lockett, R. Sedev, J. Ralston, M. Horne, T. Rodopoulos, *Differential capacitance of the electrical double layer in imidazolium-based ionic liquids: influence of potential, cation size, and temperature.* J. Phys. Chem. C, 2008. **112**(19): p. 7486-7495.

[93] V. Lockett, M. Horne, R. Sedev, T. Rodopoulos, J. Ralston, *Differential capacitance of the double layer at the electrode/ionic liquids interface.* Phys. Chem. Chem. Phys., 2010. **12**(39): p. 12499-12512.

[94] L. Siinor, K. Lust, E. Lust, *Electrical double layer capacitance at Bi(111) / 1-ethyl-3-methylimidazolium tetrafluoroborate interface as a function of the electrode potential.* J. Electrochem. Soc., 2010. **157**(7): p. F83-F87.

[95] L. Siinor, K. Lust, E. Lust, *Influence of anion composition and size on the double layer capacitance for Bi(111)|room temperature ionic liquid interface.* Electrochem. Commun., 2010. **12**(8): p. 1058-1061.

[96] F. Silva, C. Gomes, M. Figueiredo, R. Costa, A. Martins, C. M. Pereira, *The electrical double layer at the [BMIM][PF_6] ionic liquid/electrode interface - Effect of temperature on the differential capacitance.* J. Electroanal. Chem., 2008. **622**(2): p. 153-160.

[97] J. P. Zheng, P. C. Goonetilleke, C. M. Pettit, D. Roy, *Probing the electrochemical double layer of an ionic liquid using voltammetry and impedance spectroscopy: A comparative study of carbon nanotube and glassy carbon electrodes in [EMIM]$^+$[$EtSO_4$]$^-$.* Talanta, 2010. **81**(3): p. 1045-1055.

[98] M. T. Alam, M. Islam, T. Okajima, T. Ohsaka, *Measurements of differential capacitance in room temperature ionic liquid at mercury, glassy carbon and gold electrode interfaces.* Electrochem. Commun., 2007. **9**(9): p. 2370-2374.

[99] M. T. Alam, M. M. Islam, T. Okajima, T. Ohsaka, *Ionic liquid structure dependent electrical double layer at the mercury interface.* J. Phys. Chem. C, 2008. **112**(7): p. 2601-2606.

[100] M. T. Alam, M. M. Islam, T. Okajima, T. Ohsaka, *Capacitance measurements in a series of room-temperature ionic liquids at glassy carbon and gold electrode interfaces.* J. Phys. Chem. C, 2008. **112**(42): p. 16600-16608.

[101] M. T. Alam, M. M. Islam, T. Okajima, T. Ohsaka, *Measurements of differential capacitance at mercury/room-temperature ionic liquids interfaces.* J. Phys. Chem. C, 2007. **111**(49): p. 18326-18333.

[102] Y. Lauw, M. D. Horne, T. Rodopoulos, A. Nelson, F. A. M. Leermakers, *Electrical double-layer capacitance in room temperature ionic liquids: Ion-size and specific adsorption effects.* J. Phys. Chem. B, 2010. **114**(34): p. 11149-11154.

[103] C. Nanjundiah, S. F. McDevitt, V. R. Koch, *Differential capacitance measurements in solvent-free ionic liquids at Hg and C interfaces.* J. Electrochem. Soc., 1997. **144**(10): p. 3392-3397.

[104] T. Pajkossy, D. M. Kolb, *The interfacial capacitance of Au(100) in an ionic liquid, 1-butyl-3-methyl-imidazolium hexafluorophosphate.* Electrochem. Commun., 2011. **13**(3): p. 284-286.

[105] M. Drüschler, B. Huber, B. Roling, *On capacitive processes at the interface between 1-ethyl-3-methylimidazolium tris(pentafluoroethyl)trifluorophosphate and Au(111).* J. Phys. Chem. C, 2011. **115**(14): p. 6802-6808.

[106] M. Drüschler, B. Huber, S. Passerini, B. Roling, *Hysteresis effects in the potential-dependent double layer capacitance of room temperature ionic liquids at a polycrystalline platinum interface.* J. Phys. Chem. C, 2011. **114**(8): p. 3614-3617.

[107] M. Drüschler, N. Borisenko, J. Wallauer, C. Winter, B. Huber, F. Endres, B. Roling, *New insights into the interface between a single-crystalline metal electrode and an extremely pure ionic liquid: Slow interfacial processes and the influence of temperature on interfacial dynamics.* Phys. Chem. Chem. Phys., 2012. **14**(15): p. 5090-5099.

[108] R. Atkin, N. Borisenko, M. Drüschler, F. Endres, R. Hayes, B. Huber, B. Roling, *Structure and dynamics of the interfacial layer between ionic liquids and electrode materials.* J. Mol. Liq., 2014. **192**: p. 44-54.

[109] R. Atkin, N. Borisenko, M. Drüschler, S. Zein El Abedin, F. Endres, R. Hayes, B. Huber, B. Roling, *An in situ STM/AFM and impedance spectroscopy study of the extremely pure 1-butyl-1-methylpyrrolidinium tris(pentafluoroethyl)-trifluorophosphate/Au(111) interface: Potential dependent solvation layers and the herringbone reconstruction.* Phys. Chem. Chem. Phys., 2011. **13**(15): p. 6849-6857.

[110] T. Jänsch, J. Wallauer, B. Roling, *Influence of electrode roughness on double layer formation in ionic liquids.* J. Phys. Chem. C, 2015. **119**(9): p. 4620-4626.

[111] M. Gnahm, T. Pajkossy, D. M. Kolb, *The interface between Au(111) and an ionic liquid.* Electrochim. Acta, 2010. **55**(21): p. 6212-6217.

[112] A. A. Kornyshev, R. Qiao, *Three-dimensional double layers.* J. Phys. Chem. C, 2014. **118**(32): p. 18285-18290.

[113] C. Lian, D.-e. Jiang, H. Liu, J. Wu, *A generic model for electric double layers in porous electrodes.* J. Phys. Chem. C, 2016. **120**(16): p. 8704-8710.

[114] M. Z. Bazant, B. D. Storey, A. A. Kornyshev, *Double layer in ionic liquids: Overscreening versus crowding.* Phys. Rev. Lett., 2011. **106**(4): p. 046102.

[115] R. M. Lynden-Bell, A. I. Frolov, M. V. Fedorov, *Electrode screening by ionic liquids.* Phys. Chem. Chem. Phys., 2012. **14**(8): p. 2693-2701.

[116] Z. A. H. Goodwin, G. Feng, A. A. Kornyshev, *Mean-field theory of electrical double layer In ionic liquids with account of short-range correlations.* Electrochim. Acta, 2017. **225**: p. 190-197.

[117] A. C. Maggs, R. Podgornik, *General theory of asymmetric steric interactions in electrostatic double layers.* Soft Matter, 2016. **12**(4): p. 1219-1229.

[118] A. B. Yu, A. L. Kolesnikov, M. G. Kiselev, *A modified Poisson-Boltzmann theory: Effects of co-solvent polarizability.* EPL, 2015. **111**(2): p. 28002.

[119] R. Kjellander, *Decay behavior of screened electrostatic surface forces in ionic liquids: The vital role of non-local electrostatics.* Phys. Chem. Chem. Phys., 2016. **18**(28): p. 18985-19000.

[120] A. A. Kornyshev, N. B. Luque, W. Schmickler, *Differential capacitance of ionic liquid interface with graphite: the story of two double layers.* J. Solid State Electrochem., 2014. **18**(5): p. 1345-1349.

[121] C. Merlet, D. T. Limmer, M. Salanne, R. van Roij, P. A. Madden, D. Chandler, B. Rotenberg, *The electric double layer has a life of its own.* J. Phys. Chem. C, 2014. **118**(32): p. 18291-18298.

[122] C. Merlet, B. Rotenberg, P. A. Madden, M. Salanne, *Computer simulations of ionic liquids at electrochemical interfaces.* Phys. Chem. Chem. Phys., 2013. **15**(38): p. 15781-15792.

[123] Z. A. H. Goodwin, A. A. Kornyshev, *Underscreening, overscreening and double-layer capacitance.* Electrochem. Commun., 2017. **82**: p. 129-133.

[124] A. A. Lee, D. Vella, S. Perkin, A. Goriely, *Are room-temperature ionic liquids dilute electrolytes?* J. Phys. Chem. Lett., 2015. **6**(1): p. 159-163.

[125] T. Gao, J. Itliong, S. P. Kumar, Z. Hjorth, I. Nakamura, *Polarization of ionic liquid and polymer and its implications for polymerized ionic liquids: An overview towards a new theory and simulation.* J. Polym. Sci., 2021. **59**(21): p. 2434-2457.

[126] I. Nakamura, C. J. Shock, L. Eggart, T. Gao, *Theoretical aspects of ionic liquids for soft-matter sciences.* Isr. J. Chem., 2021. **59**(9): p. 813-823.

[127] H. Ers, M. Lembinen, M. MiÅ¡in, A. P. Seitsonen, M. V. Fedorov, V. B. Ivaništšev, *Graphene-ionic liquid interfacial potential drop from density functional theory-based molecular dynamics simulations.* J. Phys. Chem. C, 2020. **124**(36): p. 19548-19555.

[128] A. Levy, M. McEldrew, M. Z. Bazant, *Spin-glass charge ordering in ionic liquids.* Phys. Rev. Mater., 2019. **3**(5): p. 055606.

[129] J. P. de Souza, Z. A. H. Goodwin, M. McEldrew, A. A. Kornyshev, M. Z. Bazant, *Interfacial layering in the electric double layer of ionic liquids.* Phys. Rev. Lett., 2020. **125**(11): p. 116001.

[130] M. V. Fedorov, A. A. Kornyshev, *Towards understanding the structure and capacitance of electrical double layer in ionic liquids.* Electrochim. Acta, 2008. **53**(23): p. 6835-6840.

[131] M. V. Fedorov, N. Georgi, A. A. Kornyshev, *Double layer in ionic liquids: The nature of the camel shape of capacitance.* Electrochem. Commun., 2010. **12**(2): p. 296-299.

[132] S. Baldelli, *Surface structure at the ionic liquid-electrified metal interface.* Acc. Chem. Res., 2008. **41**(3): p. 421-431.

[133] Y. Jeon, J. Sung, W. Bu, D. Vaknin, Y. Ouchi, D. Kim, *Interfacial restructuring of ionic liquids determined by sum-frequency generation spectroscopy and X-ray reflectivity.* J. Phys. Chem. C, 2008. **112**(49): p. 19649-19654.

[134] C. S. Santos, S. Baldelli, *Alkyl chain interaction at the surface of room temperature ionic liquids: Systematic variation of alkyl chain length (R = C1-C4, C8) in both cation and anion of [RMIM][R-OSO_3] by sum frequency generation and surface tension.* J. Phys. Chem. B, 2009. **113**(4): p. 923-933.

[135] S. Watanabe, G. A. Pilkington, A. Oleshkevych, P. Pedraz, M. Radiom, R. Welbourn, S. Glavatskih, M. W. Rutland, *Interfacial structuring of non-halogenated imidazolium ionic liquids at charged surfaces: Effect of alkyl chain length.* Phys. Chem. Chem. Phys., 2020. **22**(16): p. 8450-8460.

[136] A. M. Smith, A. A. Lee, S. Perkin, *The electrostatic screening length in concentrated electrolytes increases with concentration.* J. Phys. Chem. Lett., 2016. **7**(12): p. 2157-2163.

[137] M. A. Gebbie, H. A. Dobbs, M. Valtiner, J. N. Israelachvili, *Long-range electrostatic screening in ionic liquids.* Proc. Natl. Acad. Sci., 2015. **112**(24): p. 7432-7437.

[138] S. Coles, A. M. Smith, M. V. Fedorov, F. Hausen, S. Perkin, *Interfacial structure and structural forces in mixtures of ionic liquid with a polar solvent.* Faraday Discuss., 2017. **206**: p. 427-442.

[139] S. Perkin, *Ionic liquids in confined geometries.* Phys. Chem. Chem. Phys., 2012. **14**(15): p. 5052-5062.

[140] M. Mezger, R. Roth, H. Schröder, P. Reichert, D. Pontoni, H. Reichert, *Solid-liquid interfaces of ionic liquid solutions - Interfacial layering and bulk correlations.* J. Chem. Phys., 2015. **142**(16): p. 164707.

[141] M. Mezger, B. M. Ocko, H. Reichert, M. Deutsch, *Surface layering and melting in an ionic liquid studied by resonant soft X-ray reflectivity.* Proc. Natl. Acad. Sci., 2013. **110**(10): p. 3733-3737.

[142] P. Reichert, K. S. Kjaer, T. Brandt van Driel, J. Mars, J. W. Ochsmann, D. Pontoni, M. Deutsch, M. M. Nielsen, M. Mezger, *Molecular scale structure and dynamics at an ionic liquid/electrode interface.* Faraday Discuss., 2017.

[143] Z. Brkljača, M. Klimczak, Z. Miličević, M. Weisser, N. Taccardi, P. Wasserscheid, D. M. Smith, A. Magerl, A.-S. Smith, *Complementary molecular dynamics and X-ray reflectivity study of an imidazolium-based ionic liquid at a neutral sapphire interface.* J. Phys. Chem. Lett., 2015. **6**(3): p. 549-555.

[144] A. Uysal, H. Zhou, G. Feng, S. S. Lee, S. Li, P. Fenter, P. T. Cummings, P. F. Fulvio, S. Dai, J. K. McDonough, Y. Gogotsi, *Structural origins of potential dependent hysteresis at the electrified graphene/ionic liquid interface.* J. Phys. Chem. C, 2014. **118**(1): p. 569-574.

[145] T. A. Petach, A. Mehta, R. Marks, B. Johnson, M. F. Toney, D. Goldhaber-Gordon, *Voltage-controlled interfacial layering in an ionic liquid on $SrTiO_3$.* ACS Nano, 2016. **10**(4): p. 4565-4569.

[146] M. Mezger, H. Schröder, H. Reichert, S. Schramm, J. S. Okasinski, S. Schöder, V. Honkimäki, M. Deutsch, B. M. Ocko, J. Ralston, M. Rohwerder, M. Stratmann, H. Dosch, *Molecular layering of fluorinated ionic liquids at a charged sapphire (0001) surface.* Science, 2008. **322**(5900): p. 424-428.

[147] M. Mezger, S. Schramm, H. Schroder, H. Reichert, M. Deutsch, E. J. De Souza, J. S. Okasinski, B. M. Ocko, V. Honkimaki, H. Dosch, *Layering of [BMIM]$^+$-based ionic liquids at a charged sapphire interface.* J. Chem. Phys., 2009. **131**(9): p. 094701-9.

[148] T. L. Greaves, D. F. Kennedy, S. T. Mudie, C. J. Drummond, *Diversity observed in the nanostructure of protic ionic liquids.* J. Phys. Chem. B, 2010. **114**(31): p. 10022-10031.

[149] B. Uhl, T. Cremer, M. Roos, F. Maier, H.-P. Steinrück, R. J. Behm, *At the ionic liquid|metal interface: Structure formation and temperature dependent behavior of an ionic liquid adlayer on Au(111).* Phys. Chem. Chem. Phys., 2013. **15**(40): p. 17295-17302.

[150] B. Uhl, F. Buchner, S. Gabler, M. Bozorgchenani, R. J. Behm, *Adsorption and reaction of sub-monolayer films of an ionic liquid on Cu(111).* Chem. Commun., 2014. **50**(62): p. 8601-8604.

[151] A. B. Biedron, E. L. Garfunkel, E. W. Castner, S. Rangan, *Ionic liquid ultrathin films at the surface of Cu(100) and Au(111).* J. Chem. Phys., 2017. **146**(5): p. 054704.

[152] F. Greco, S. Shin, F. J. Williams, B. S. J. Heller, F. Maier, H. P. Steinruck, *Potential screening at electrode/ionic liquid interfaces from in situ X-ray photoelectron spectroscopy.* ChemistryOpen, 2019. **8**(12): p. 1365-1368.

[153] Y. Lauw, M. D. Horne, T. Rodopoulos, V. Lockett, B. Akgun, W. A. Hamilton, A. R. J. Nelson, *Structure of [C_4mpyr][NTf_2] room-temperature ionic liquid at charged gold interfaces.* Langmuir, 2012. **28**(19): p. 7374-7381.

[154] Y. Lauw, T. Rodopoulos, M. Gross, N. A., R. Gardner, M. D. Horne, *Electrochemical cell for neutron reflectometry studies of the structure of ionic liquids at electrified interface.* Rev. Sci. Instrum., 2010. **81**(7): p. 074101.

[155] C. P. Cabry, L. D'Andrea, K. Shimizu, I. Grillo, P. Li, S. Rogers, D. W. Bruce, J. N. Canongia Lopes, J. M. Slattery, *Exploring the bulk-phase structure of ionic liquid mixtures using small-angle neutron scattering.* Faraday Discuss., 2018. **206**: p. 265-289.

[156] O. Russina, A. Triolo, *Ionic liquids and neutron scattering*. Experimental methods in the physical sciences. 2017. 213-278.

[157] R. Hayes, S. Imberti, G. G. Warr, R. Atkin, *Amphiphilicity determines nanostructure in protic ionic liquids.* Phys. Chem. Chem. Phys., 2011. **13**(8): p. 3237-3247.

[158] C. Hardacre, J. D. Holbrey, C. L. Mullan, T. G. A. Youngs, D. T. Bowron, *Small angle neutron scattering from 1-alkyl-3-methylimidazolium hexafluorophosphate ionic liquids ([$C_n$mim][PF_6], n = 4, 6, and 8).* J. Chem. Phys., 2010. **133**(7): p. 074510-7.

[159] N. Nishi, J. Uchiyashiki, Y. Ikeda, S. Katakura, T. Oda, M. Hino, N. L. Yamada, *Potential-dependent structure of the ionic layer at the electrode interface of an ionic liquid probed using neutron reflectometry.* J. Phys. Chem. C, 2019. **123**(14): p. 9223-9230.

[160] M. Meusel, M. Lexow, A. Gezmis, S. Schötz, M. Wagner, A. Bayer, F. Maier, H.-P. Steinrück, *Atomic force and scanning tunneling microscopy of ordered ionic liquid wetting layers from 110 K up to room temperature.* ACS Nano, 2020. **14**(7): p. 9000-9010.

[161] B. Uhl, H. H. Huang, D. Alwast, F. Buchner, R. J. Behm, *Interaction of ionic liquids with noble metal surfaces: Structure formation and stability of [OMIM][TFSA] and [EMIM][TFSA] on Au(111) and Ag(111).* Phys. Chem. Chem. Phys., 2015. **17**(37): p. 23816-23832.

[162] Z. Liu, T. Cui, T. Lu, M. Shapouri Ghazvini, F. Endres, *Anion effects on the solid/ionic liquid interface and the electrodeposition of zinc.* J. Phys. Chem. C, 2016. **120**(36): p. 20224-20231.

[163] H. Li, J. W. Ross, E. Frank, A. Rob, *Influence of alkyl chain length and anion species on ionic liquid structure at the graphite interface as a function of applied potential.* J. Phys. Condens. Matter., 2014. **26**(28): p. 284115.

[164] M. G. Li, L. Chen, Y. X. Zhong, Z. B. Chen, J. W. Yan, B. W. Mao, *The electrochemical interface of Ag(111) in 1-ethyl-3-methylimidazolium bis(trifluoromethylsulfonyl)imide ionic liquid - A combined in-situ scanning probe microscopy and impedance study.* Electrochim. Acta, 2016. **197**: p. 282-289.

[165] A. Sheehan, L. A. Jurado, S. N. Ramakrishna, A. Arcifa, A. Rossi, N. D. Spencer, R. M. Espinosa-Marzal, *Layering of ionic liquids on rough surfaces.* Nanoscale, 2016. **8**(7): p. 4094-4106.

[166] T. Carstens, R. Gustus, O. Höfft, N. Borisenko, F. Endres, H. Li, R. J. Wood, A. J. Page, R. Atkin, *Combined STM, AFM, and DFT study of the highly ordered pyrolytic graphite/1-octyl-3-methyl-imidazolium bis(trifluoromethylsulfonyl)imide interface.* J. Phys. Chem. C, 2014. **118**(20): p. 10833-10843.

[167] T. Carstens, A. Ispas, N. Borisenko, R. Atkin, A. Bund, F. Endres, *In situ scanning tunneling microscopy (STM), atomic force microscopy (AFM) and quartz crystal microbalance (EQCM) studies of the electrochemical deposition of tantalum in two different ionic liquids with the 1-butyl-1-methylpyrrolidinium cation.* Electrochimica Acta, 2016. **197**: p. 374-387.

[168] H. Li, M. W. Rutland, M. Watanabe, R. Atkin, *Boundary layer friction of solvate ionic liquids as a function of potential.* Faraday Discuss., 2017. **199**: p. 311-322.

[169] A. Elbourne, S. McDonald, K. Voïchovsky, F. Endres, G. G. Warr, R. Atkin, *Nanostructure of the ionic liquid-graphite Stern layer.* ACS Nano, 2015. **9**(7): p. 7608-7620.

[170] T. Cui, A. Lahiri, T. Carstens, N. Borisenko, G. Pulletikurthi, C. Kuhl, F. Endres, *Influence of water on the electrified ionic liquid/solid interface: A direct observation of the transition from a multilayered structure to a double-layer structure.* J. Phys. Chem. C, 2016. **120**(17): p. 9341-9349.

[171] R. Hayes, N. Borisenko, M. K. Tam, P. C. Howlett, F. Endres, R. Atkin, *Double layer structure of ionic liquids at the Au(111) electrode interface: An atomic force microscopy investigation.* J. Phys. Chem. C, 2011. **115**(14): p. 6855-6863.

[172] R. Hayes, G. G. Warr, R. Atkin, *At the interface: Solvation and designing ionic liquids.* Phys. Chem. Chem. Phys., 2010. **12**(8): p. 1709-1723.

[173] R. Atkin, S. Zein El Abedin, R. Hayes, L. H. S. Gasparotto, N. Borisenko, F. Endres, *AFM and STM studies on the surface interaction of [BMP]TFSA and [EMIm]TFSA ionic liquids with Au(111).* J. Phys. Chem. C, 2009. **113**(30): p. 13266-13272.

[174] R. Hayes, S. Zein El Abedin, R. Atkin, *Pronounced structure in confined aprotic room-temperature ionic liquids.* J. Phys. Chem. B, 2009. **113**(20): p. 7049-7052.

[175] H. Li, F. Endres, R. Atkin, *Effect of alkyl chain length and anion species on the interfacial nanostructure of ionic liquids at the Au(111)-ionic liquid interface as a function of potential.* Phys. Chem. Chem. Phys., 2013. **15**(35): p. 14624-14633.

[176] Y. Z. Su, J. W. Yan, M. G. Li, M. Zhang, B. W. Mao, *Electric double layer of Au(100)/imidazolium-based ionic liquids interface: Effect of cation size.* J. Phys. Chem. C, 2013. **117**(1): p. 205-212.

[177] M. Meusel, M. Lexow, A. Gezmis, A. Bayer, F. Maier, H.-P. Steinrück, *Growth of multilayers of ionic liquids on Au(111) investigated by atomic force microscopy in ultrahigh vacuum.* Langmuir, 2020. **36**(45): p. 13670-13681.

[178] A. V. Rudnev, M. R. Ehrenburg, E. B. Molodkina, A. Abdelrahman, M. Arenz, P. Broekmann, T. Jacob, *Structural changes of Au(111) single-crystal electrode surface in ionic liquids.* ChemElectroChem, 2020. **7**(2): p. 501-508.

[179] S. Liu, J. Peng, L. Chen, P. Sebastian, J. M. Feliu, J. W. Yan, B. W. Mao, *In-situ STM and AFM studies on electrochemical interfaces in imidazolium-based ionic liquids.* Electrochim. Acta, 2019. **309**: p. 11-17.

[180] M. R. Ehrenburg, E. B. Molodkina, P. Broekmann, A. V. Rudnev, *Underpotential deposition of silver on Au(111) from an air- and water-stable ionic liquid visualized by in-situ STM.* ChemElectroChem, 2019. **6**(4): p. 1149-1156.

[181] M. Meusel, A. Gezmis, S. Jaekel, M. Lexow, A. Bayer, F. Maier, H. P. Steinruck, *Time- and temperature-dependent growth behavior of ionic liquids on Au(111) studied by atomic force microscopy in ultrahigh vacuum.* J. Phys. Chem. C, 2021. **125**(37): p. 20439-20449.

[182] H. Ueda, K. Nishiyama, S. Yoshimoto, *Electrochemical behavior and specific adsorption of an iodide-based ionic liquid on Au(111).* Electrochemistry, 2018. **86**(5): p. 217-219.

[183] T. Pajkossy, C. Muller, T. Jacob, *The metal-ionic liquid interface as characterized by impedance spectroscopy and in situ scanning tunneling microscopy.* Phys. Chem. Chem. Phys., 2018. **20**(33): p. 21241-21250.

[184] H. Li, Y. X. Zhang, S. Jones, R. Segalman, G. G. Warr, R. Atkin, *Interfacial nanostructure and friction of a polymeric ionic liquid-ionic liquid mixture as a function of potential at Au(111) electrode interface.* J. Colloid Inerface Sci., 2022. **606**: p. 1170-1178.

[185] J. M. Black, M. Y. Zhu, P. F. Zhang, R. R. Unocic, D. Q. Guo, M. B. Okatan, S. Dai, P. T. Cummings, S. V. Kalinin, G. Feng, N. Balke, *Fundamental aspects of electric double layer force-distance measurements at liquid-solid interfaces using atomic force microscopy.* Sci. Rep., 2016. **6**: p. 12.

[186] V. Hoffmann, G. Pulletikurthi, T. Carstens, A. Lahiri, A. Borodin, M. Schammer, B. Horstmann, A. Latz, F. Endres, *Influence of a silver salt on the nanostructure of a Au(111)/ionic liquid interface: An atomic force microscopy study and theoretical concepts.* Phys. Chem. Chem. Phys., 2018. **20**(7): p. 4760-4771.

[187] A. Lahiri, G. Z. Li, M. Olschewski, F. Endres, *Influence of polar organic solvents in an ionic liquid containing lithium bis(fluorosulfonyl)amide: Effect on the cation-anion*

interaction, lithium ion battery performance, and solid electrolyte interphase. ACS Appl. Mater. Interfaces, 2016. **8**(49): p. 34143-34150.

[188] A. Lahiri, T. Carstens, R. Atkin, N. Borisenko, F. Endres, *In situ atomic force microscopic studies of the interfacial multilayer nanostructure of LiTFSI-[$Py_{1,4}$]TFSI on Au(111): Influence of Li^+ ion concentration on the Au(111)/IL interface.* J. Phys. Chem. C, 2015. **119**(29): p. 16734-16742.

[189] R. Hayes, D. Wakeham, R. Atkin, *Interfaces of ionic liquids (2)*, in *Ionic liquids UnCOILed: Critical expert overviews*, K. R. Seddon, N. Plechkova, Editors. 2013, John Wiley & Sons, Inc.: Hoboken, New Jersey. p. 51-86.

[190] F. Endres, N. Borisenko, S. Zein El Abedin, R. Hayes, R. Atkin, *The interface ionic liquid(s)/electrode(s): In situ STM and AFM measurements.* Faraday Discuss., 2012. **154**(0): p. 221-233.

[191] T. Carstens, R. Hayes, S. Zein El Abedin, B. Corr, G. B. Webber, N. Borisenko, R. Atkin, F. Endres, *In situ STM, AFM and DTS study of the interface 1-hexyl-3-methylimidazolium tris(pentafluoroethyl)trifluorophosphate/Au(111).* Electrochim. Acta, 2012. **82**(0): p. 48-59.

[192] J. Sweeney, F. Hausen, R. Hayes, G. B. Webber, F. Endres, M. W. Rutland, R. Bennewitz, R. Atkin, *Control of nanoscale friction on gold in an ionic liquid by a potential-dependent ionic lubricant layer.* Phys. Rev. Lett., 2012. **109**(15): p. 155502.

[193] A. Triolo, O. Russina, H.-J. Bleif, E. Di Cola, *Nanoscale segregation in room temperature ionic liquids.* J. Phys. Chem. B, 2007. **111**(18): p. 4641-4644.

[194] M. A. Gebbie, M. Valtiner, X. Banquy, E. T. Fox, W. A. Henderson, J. N. Israelachvili, *Ionic liquids behave as dilute electrolyte solutions.* Proc. Natl. Acad. Sci., 2013. **110**(24): p. 9674-9679.

[195] C. Hsiu-Wei, P. Stock, B. Moeremans, T. Baimpos, X. Banquy, F. U. Renner, M. Valtiner, *Characterizing the influence of water on charging and layering at electrified ionic-liquid/solid interfaces.* Adv. Mater. Interfaces, 2015. **2**(12): p. 1500159.

[196] R. M. Espinosa-Marzal, A. Arcifa, A. Rossi, N. D. Spencer, *Microslips to "avalanches" in confined, molecular layers of ionic liquids.* J. Phys. Chem. Lett., 2014. **5**(1): p. 179-184.

[197] X. Hu, C. Chen, S. Tang, W. Wang, J. Yan, B. Mao, *An in situ STM investigation of EMITFSI ionic liquid on Au(111) in the presence of lithium salt.* Sci. Bull., 2015. **60**(9): p. 877-883.

[198] Z. Liu, N. Borisenko, S. Zein El Abedin, F. Endres, *In situ STM study of zinc electrodeposition on Au(111) from the ionic liquid 1-ethyl-3-methylimidazolium trifluoromethylsulfonate.* J. Solid State Electrochem., 2014. **18**(9): p. 2581-2587.

[199] L. G. Lin, Y. Wang, J. W. Yan, Y. Z. Yuan, J. Xiang, B. W. Mao, *An in situ STM study on the long-range surface restructuring of Au(111) in a non-chloroaluminumated ionic liquid.* Electrochem. Commun., 2003. **5**(12): p. 995-999.

[200] G.-B. Pan, W. Freyland, *2D phase transition of PF_6 adlayers at the electrified ionic liquid/Au(111) interface.* Chem. Phys. Lett., 2006. **427**(1-3): p. 96-100.

[201] N. Borisenko, S. Zein El Abedin, F. Endres, *In situ STM investigation of gold reconstruction and of silicon electrodeposition on Au(111) in the room temperature*

ionic liquid 1-butyl-1-methylpyrrolidinium bis(trifluoromethylsulfonyl)imide. J. Phys. Chem. B, 2006. **110**(12): p. 6250-6256.

[202] Y.-Z. Su, J.-W. Yan, M.-G. Li, Z.-X. Xie, B.-W. Mao, Z.-Q. Tian, *Adsorption of solvent cations on Au(111) and Au(100) in alkylimidazolium-based ionic liquids - worm-like versus Micelle-like structures.* Z. Phys. Chem., 2012. **226**(9-10): p. 979-994.

[203] Y.-Z. Su, Y.-C. Fu, J.-W. Yan, Z.-B. Chen, B.-W. Mao, *Double layer of Au(100)/ionic liquid interface and its stability in imidazolium-based ionic liquids.* Angew. Chem. Int. Edit., 2009. **48**(28): p. 5148-5151.

[204] M. Gnahm, C. Muller, R. Repanszki, T. Pajkossy, D. M. Kolb, *The interface between Au(100) and 1-butyl-3-methyl-imidazolium-hexafluorophosphate.* Phys. Chem. Chem. Phys., 2011. **13**(24): p. 11627-11633.

[205] M. Gnahm, C. Berger, M. Arkhipova, H. Kunkel, T. Pajkossy, G. Maas, D. M. Kolb, *The interfaces of Au(111) and Au(100) in a hexaalkyl-substituted guanidinium ionic liquid: An electrochemical and in situ STM study.* Phys. Chem. Chem. Phys., 2012. **14**(30): p. 10647-10652.

[206] T.-H. Vu, Y. Fu, T. Wandlowski, *The electrochemical interface of Au(111) and Au(100) in HMIm-FAP ionic liquid.* J. Nanosci. Nanotechnol., 2016. **16**(8): p. 7942-7948.

[207] C. Müller, S. Vesztergom, T. Pajkossy, T. Jacob, *The interface between Au(100) and 1-butyl-3-methyl-imidazolium-bis(trifluoromethylsulfonyl)imide.* J. Electroanal. Chem., 2015. **737**: p. 218-225.

[208] C. Müller, K. Nemeth, S. Vesztergom, T. Pajkossy, T. Jacob, *The interface between HOPG and 1-butyl-3-methyl-imidazolium hexafluorophosphate.* Phys. Chem. Chem. Phys., 2016. **18**(2): p. 916-925.

[209] N. Borisenko, R. Atkin, A. Lahiri, S. Zein El Abedin, F. Endres, *Effect of dissolved LiCl on the ionic liquid/Au(111) interface: An in situ STM study.* J. Phys. Condens. Matter., 2014. **26**(28): p. 284111-9.

[210] F. Endres, S. Zein El Abedin, N. Borissenko, *Probing lithium and alumina impurities in air- and water stable ionic liquids by cyclic voltammetry and in situ scanning tunneling microscopy.* Z. Phys. Chem., 2006. **220**(10): p. 1377-1394.

[211] T. Waldmann, H.-H. Huang, H. E. Hoster, O. Höfft, F. Endres, R. J. Behm, *Imaging an ionic liquid adlayer by scanning tunneling microscopy at the solid / vacuum interface.* ChemPhysChem, 2011. **12**(14): p. 2565-2567.

[212] F. Buchner, K. Forster-Tonigold, B. Uhl, D. Alwast, N. Wagner, H. Farkhondeh, A. Groß, R. J. Behm, *Toward the microscopic identification of anions and cations at the ionic liquid|Ag(111) interface: A combined experimental and theoretical investigation.* ACS Nano, 2013. **7**(9): p. 7773-7784.

[213] B. Uhl, F. Buchner, D. Alwast, N. Wagner, R. J. Behm, *Adsorption of the ionic liquid [BMP][TFSA] on Au(111) and Ag(111): Substrate effects on the structure formation investigated by STM.* Beilstein J. Nanotechnol., 2013. **4**: p. 903-918.

[214] F. Buchner, M. Bozorgchenani, B. Uhl, H. Farkhondeh, J. Bansmann, R. J. Behm, *Reactive interaction of (sub-)monolayers and multi layers of the ionic liquid 1-butyl-1-methylpyrrolidinium bis(trifluoro-methylsulfonyl)imide with coadsorbed lithium on Cu(111).* J. Phys. Chem. C, 2015. **119**(29): p. 16649-16659.

[215] F. Buchner, K. Forster-Tonigold, M. Bozorgchenani, A. Gross, R. J. Behm, *Interaction of a self-assembled ionic liquid layer with graphite(0001): A combined experimental and theoretical study.* J. Phys. Chem. Lett., 2016. **7**(2): p. 226-233.

[216] A. Elbourne, K. Voitchovsky, G. G. Warr, R. Atkin, *Ion structure controls ionic liquid near-surface and interfacial nanostructure.* Chem. Sci., 2015. **6**(1): p. 527-536.

[217] J. J. Segura, A. Elbourne, E. J. Wanless, G. G. Warr, K. Voitchovsky, R. Atkin, *Adsorbed and near surface structure of ionic liquids at a solid interface.* Phys. Chem. Chem. Phys., 2013. **15**(9): p. 3320-3328.

[218] A. J. Page, A. Elbourne, R. Stefanovic, M. A. Addicoat, G. G. Warr, K. Voitchovsky, R. Atkin, *3-Dimensional atomic scale structure of the ionic liquid-graphite interface elucidated by AM-AFM and quantum chemical simulations.* Nanoscale, 2014. **6**(14): p. 8100-8106.

[219] S. McDonald, A. Elbourne, G. G. Warr, R. Atkin, *Metal ion adsorption at the ionic liquid-mica interface.* Nanoscale, 2016. **8**(2): p. 906-914.

[220] F. Endres, O. Höfft, N. Borisenko, L. H. Gasparotto, A. Prowald, R. Al-Salman, T. Carstens, R. Atkin, A. Bund, S. Zein El Abedin, *Do solvation layers of ionic liquids influence electrochemical reactions?* Phys. Chem. Chem. Phys., 2010. **12**(8): p. 1724-1732.

[221] S. Zein El Abedin, E. M. Moustafa, R. Hempelmann, H. Natter, F. Endres, *Electrodeposition of nano- and microcrystalline aluminium in three different air and water stable ionic liquids.* ChemPhysChem, 2006. **7**(7): p. 1535-1543.

[222] Z. Liu, S. Zein El Abedin, F. Endres, *Electrodeposition of zinc films from ionic liquids and ionic liquid/water mixtures.* Electrochim. Acta, 2013. **89**: p. 635-643.

[223] P. Giridhar, S. Zein El Abedin, F. Endres, *Electrodeposition of nanocrystalline aluminium, copper, and copper-aluminium alloys from 1-butyl-1-methylpyrrolidinium trifluoromethylsulfonate ionic liquid.* J. Solid State Electrochem., 2012. **16**(11): p. 3487-3497.

[224] Z. Liu, S. Z. El Abedin, F. Endres, *Electrochemical and spectroscopic study of Zn(ii) coordination and Zn electrodeposition in three ionic liquids with the trifluoromethylsulfonate anion, different imidazolium ions and their mixtures with water.* Phys. Chem. Chem. Phys., 2015. **17**(24): p. 15945-15952.

[225] G. Pulletikurthi, A. Lahiri, T. Carstens, N. Borisenko, S. Zein El Abedin, F. Endres, *Electrodeposition of silicon from three different ionic liquids: possible influence of the anion on the deposition process.* J. Solid State Electrochem., 2013. **17**(11): p. 2823-2832.

[226] P. Giridhar, A. M. Elbasiony, S. Zein El Abedin, F. Endres, *A Comparative Study on the Electrodeposition of Tin from Two Different Ionic Liquids: Influence of the Anion on the Morphology of the Tin Deposits.* ChemElectroChem, 2014. **1**(9): p. 1549-1556.

[227] R. Al-Salman, F. Endres, *Template-assisted electrodeposition of Si_xGe_{1-x} nanowires with varying length and composition from two different ionic liquids.* J. Mater. Chem., 2009. **19**(39): p. 7228-7231.

[228] A. Lahiri, N. Borisenko, M. Olschewski, R. Gustus, J. Zahlbach, F. Endres, *Electroless deposition of III-V semiconductor nanostructures from ionic liquids at room temperature.* Angew. Chem. Int. Edit., 2015. **54**(40): p. 11870-11874.

[229] N. Borisenko, A. Lahiri, G. Pulletikurthi, T. Cui, T. Carstens, J. Zahlbach, R. Atkin, F. Endres, *The Au(111)/IL interfacial nanostructure in the presence of precursors and its influence on the electrodeposition process.* Faraday Discuss., 2017. **206**(0): p. 459-473.

[230] N. Borisenko, S. Zein El Abedin, F. Endres, *An in situ STM and DTS study of the extremely pure [EMIM]FAP/Au(111) interface.* ChemPhysChem, 2012. **13**(7): p. 1736-1742.

[231] T. Carstens, A. Lahiri, N. Borisenko, F. Endres, *[$Py_{1,4}$]FSI-NaFSI-based ionic liquid electrolyte for sodium batteries: Na^+ solvation and interfacial nanostructure on Au(111).* J. Phys. Chem. C, 2016. **120**(27): p. 14736-14741.

[232] J. N. Israelachvili, *Intermolecular and surface forces* 2011, London: Elsevier.

[233] R. Hayes, N. Borisenko, B. Corr, G. B. Webber, F. Endres, R. Atkin, *Effect of dissolved LiCl on the ionic liquid-Au(111) electrical double layer structure.* Chem. Commun., 2012. **48**(82): p. 10246-10248.

[234] A. Borodin, N. Borisenko, F. Endres, *The apparent band gap of p-doped H-passivated Si(111) with a thin film of an ionic liquid on top.* J. Phys. Chem. C, 2018. **122**(10): p. 5481-5488.

[235] N. Borisenko, A. Lahiri, F. Endres, *Electrodeposition of semiconductors in ionic liquids*, in *Electrodeposition from ionic liquids. 2nd edition*, F. Endres, A. Abbott, D. R. MacFarlane, Editors. 2017, Wiley-VCH Verlag GmbH & Co. KGaA: Weinheim. p. 187-210.

[236] G. Pulletikurthi, N. Borisenko, F. Endres, *Electrodeposition of refractory metals from ionic liquids*, in *Electrodeposition from ionic liquids. 2nd edition*, F. Endres, A. Abbott, D. R. MacFarlane, Editors. 2017, Wiley-VCH Verlag GmbH & Co. KGaA: Weinheim. p. 104-119.

[237] A. Ispas, B. Adolphi, A. Bund, F. Endres, *On the electrodeposition of tantalum from three different ionic liquids with the bis(trifluoromethyl sulfonyl) amide anion.* Phys. Chem. Chem. Phys., 2010. **12**(8): p. 1793-1803.

[238] N. Borisenko, A. Ispas, E. Zschippang, Q. Liu, S. Zein El Abedin, A. Bund, F. Endres, *In situ STM and EQCM studies of tantalum electrodeposition from TaF_5 in the air- and water-stable ionic liquid 1-butyl-1-methylpyrrolidinium bis(trifluoromethylsulfonyl)amide.* Electrochim. Acta, 2009. **54**(5): p. 1519-1528.

[239] M. Castriota, T. Caruso, R. G. Agostino, E. Cazzanelli, W. A. Henderson, S. Passerini, *Raman investigation of the ionic liquid N-methyl-N-propylpyrrolidinium bis(trifluoromethanesulfonyl)imide and its mixture with $LiN(SO_2CF_3)_2$.* J. Phys. Chem. A, 2005. **109**(1): p. 92-96.

[240] J. X. Mao, K. Damodaran, *Spectroscopic and computational analysis of the molecular interactions in the ionic liquid $[Emim]^+[FAP]^-$.* Ionics, 2015. **21**(6): p. 1605-1613.

[241] A. M. Moschovi, S. Ntais, V. Dracopoulos, V. Nikolakis, *Vibrational spectroscopic study of the protic ionic liquid 1-H-3-methylimidazolium bis(trifluoromethanesulfonyl)imide.* Vib. Spectrosc., 2012. **63**: p. 350-359.

[242] I. V. Voroshylova, F. Teixeira, R. Costa, C. M. Pereira, M. N. D. S. Cordeiro, *Interactions in the ionic liquid [EMIM][FAP]: A coupled experimental and computational analysis.* Phys. Chem. Chem. Phys., 2016. **18**(4): p. 2617-2628.

[243] H. Moon, R. Tatara, T. Mandai, K. Ueno, K. Yoshida, N. Tachikawa, T. Yasuda, K. Dokko, M. Watanabe, *Mechanism of Li ion desolvation at the interface of graphite electrode and glyme-Li salt solvate ionic liquids.* J. Phys. Chem. C, 2014. **118**(35): p. 20246-20256.

[244] L. A. Woodward, A. A. Nord, *723. Raman spectrum of the tetrachlorogallate ion ($GaCl^{4-}$) in aqueous solution.* J. Chem. Soc., 1956(0): p. 3721-3722.

[245] I. R. Beattie, J. R. Horder, *Gas-phase Raman spectroscopy of the trihalides of aluminium, gallium, and indium. The Raman spectra of solid and liquid indium trichloride and tribromide.* J. Chem. Soc., A Inorg. Phys. Theor., 1969(0): p. 2655-2659.

[246] H.-G. Cho, *Solvation of $GaCl_3$ in deuterated acetonitrile studied by means of vibrational spectroscopy.* Spectrochim. Acta A, 2003. **59**(7): p. 1517-1528.

[247] K. Fujii, H. Hamano, H. Doi, X. Song, S. Tsuzuki, K. Hayamizu, S. Seki, Y. Kameda, K. Dokko, M. Watanabe, Y. Umebayashi, *Unusual Li^+ ion solvation structure in bis(fluorosulfonyl)amide based ionic liquid.* J. Phys. Chem. C, 2013. **117**(38): p. 19314-19324.

[248] C. P. Rhodes, R. Frech, *Local structures in crystalline and amorphous phases of diglyme-$LiCF_3SO_3$ and poly(ethylene oxide)-$LiCF_3SO_3$ systems: Implications for the mechanism of ionic transport.* Macromolecules, 2001. **34**(8): p. 2660-2666.

[249] L. D. Reed, A. Arteaga, E. J. Menke, *A combined experimental and computational study of an aluminum triflate/diglyme electrolyte.* J. Phys. Chem. B, 2015. **119**(39): p. 12677-12681.

[250] J. F. Sawyer, G. J. Schrobilgen, S. J. Sutherland, *Crystal structure, Raman, and multinuclear NMR study of fluoro[imidobis(sulfuryl fluoride)]xenon(II) ($FXeN(SO_2F)_2$), an example of xenon-nitrogen bonding.* Inorg. Chem., 1982. **21**(11): p. 4064-4072.

[251] D. H. Johnston, D. F. Shriver, *Vibrational study of the trifluoromethanesulfonate anion: Unambiguous assignment of the asymmetric stretching modes.* Inorg. Chem., 1993. **32**(6): p. 1045-1047.

[252] J. Lewis, J. R. Miller, R. L. Richards, A. Thompson, *1098. The infrared spectra of some addition compounds of aluminium and gallium trihalides.* J. Chem. Soc., 1965(0): p. 5850-5860.

[253] N. N. Greenwood, T. S. Srivastava, B. P. Straughan, *Far infrared spectra and structure of some complexes of the gallium trihalides.* J. Chem. Soc., A Inorg. Phys. Theor., 1966(0): p. 699-702.

[254] K. Fumino, A. Wulf, R. Ludwig, *The cation–anion interaction in ionic liquids probed by Far-Infrared spectroscopy.* Angew. Chem. Int. Edit., 2008. **47**(20): p. 3830-3834.

[255] J. Huang, A. F. Hollenkamp, *Thermal behavior of ionic liquids containing the FSI anion and the Li^+ cation.* J. Phys. Chem. C, 2010. **114**(49): p. 21840-21847.

[256] K. Fujii, S. Seki, S. Fukuda, R. Kanzaki, T. Takamuku, Y. Umebayashi, S.-i. Ishiguro, *Anion conformation of low-viscosity room-temperature ionic liquid 1-ethyl-3-methylimidazolium bis(fluorosulfonyl) Imide.* J. Phys. Chem. B, 2007. **111**(44): p. 12829-12833.

[257] K. Fujii, S. Seki, S. Fukuda, T. Takamuku, S. Kohara, Y. Kameda, Y. Umebayashi, S.-i. Ishiguro, *Liquid structure and conformation of a low-viscosity ionic liquid,*

N-methyl-N-propyl-pyrrolidinium bis(fluorosulfonyl) imide studied by high-energy X-ray scattering. J. Mol. Liq., 2008. **143**(1): p. 64-69.

[258] Y. Umebayashi, T. Mitsugi, S. Fukuda, T. Fujimori, K. Fujii, R. Kanzaki, M. Takeuchi, S.-I. Ishiguro, *Lithium ion solvation in room-temperature ionic liquids involving bis(trifluoromethanesulfonyl) imide anion studied by Raman spectroscopy and DFT calculations.* J. Phys. Chem. B, 2007. **111**(45): p. 13028-13032.

10 Symbols and Abbreviations

10.1 List of Symbols

Roman Symbols

Symbol	Meaning	Usual Units
D_{ip}	ion pair diameter	nm
$D_t(E_F)$	LDOS of the tip at the Fermi level	none
E	(a) potential of an electrode versus a reference (b) energy	V eV
E_F	Fermi level	eV
E_t	energy of state ψ_t	eV
E_s	energy of state ψ_s	eV
e	electronic charge	C
F	force	nN
$f(E)$	Fermi function	none
h	Planck constant ($6.626 \cdot 10^{-34}$ J·s)	J·s
$\hbar$	reduced Planck constant ($h = \hbar / 2\pi$)	J·s
I_t	tunneling current	nA
i_t	tunneling current	nA
k	(a) $k = (2mE)^{1/2}\hbar^{-1}$ (b) inverse matrix of wave function in vacuum (c) spring constant	none none $nN \cdot nm^{-1}$
k_B	Boltzmann constant ($8.617 \cdot 10^{-5}$ eV·K^{-1})	eV·K^{-1}
L	width of an energy barrier	Nm
M	molecular weight	g·mol^{-1}
M_{ts}	tunneling matrix element	none
N_A	Avogadro constant ($6.022 \cdot 10^{23}$ mol^{-1})	mol^{-1}
m	mass of a particle	g
r	distance between the centers of two particles	nm
$\vec{r}_0$	position of a center of a tip curvature	none
T	(a) transmission probability (b) absolute temperature	none K
t	time	s
U	potential energy of a particle	eV
U_{bias}	tunneling voltage (bias)	V
U_{out}	output voltage	V

Symbol	Meaning	Usual Units
U(x)	potential energy of a particle at distance *x*	eV
V	(a) tunneling voltage (bias) (b) potential energy	V eV
x	distance	nm
z	distance between a tip and a sample surface in STM	nm

Greek Symbols

Symbol	Meaning	Usual Units
α	deflection sensitivity	none
δ	Dirac delta function	none
ε	(a) $\varepsilon = E / U$ (b) well depth	none eV
δ_c	cantilever deflection	nm
δ_s	sample deformation	nm
ρ	density of IL	g·cm^3
$\rho(E)$	DOS	none
$\rho(\vec{r}_0;E_F)$	DOS of a sample at Fermi level under the center of a tip curvature	none
$\rho_s(\vec{r}_0;E)$	DOS of a sample at position $\vec{r}_0$	none
$\rho_t(\vec{r}_0;E-eV)$	DOS of a tip at position $\vec{r}_0$	none
ϕ	arithmetic mean of work functions of a tip and of a sample	eV
ϕ_s	work function of a sample	eV
ϕ_t	work function of a tip	eV
ψ	wave function	none
ψ_s	wave function of a sample	none
ψ_t	wave function of a tip	none
$\psi(x)$	wave function at point *x*	none

10.2 List of Abbreviations

Standard Abbreviations

Abbreviation	Meaning
2D	Two-Dimensional
3D	Three-Dimensional
AES	Auger Electron Spectroscopy (AES)
AFM	Atomic Force Microscopy
AM-AFM	Amplitude-Modulated Atomic Force Microscopy
BSK	Bazant-Storey-Kornyshev
CE	Counter Electrode
CV	Cyclic Voltammetry
DFT	Density Functional Theory
DOS	Density of States
EDL	Electrical Double Layer
EIS	Electrochemical Impedance Spectroscopy
EQCM	Electrochemical Quartz Crystal Microbalance
Fc/Fc^+	Ferrocene/Ferrocinium
FFT	Fast Fourier Transformation
GCS	Gouy-Chapman-Stern
HOPG	Highly Ordered Pyrolytic Graphite
IFFT	Inversed Fast Fourier Transformation
IL	Ionic Liquid
ILs	Ionic Liquids
IR	Infrared
LDOS	Local Density of States
OCP	Open Circuit Potential
OPA	Operation Amplifier
OPD	Overpotential Deposition
PCTFE	Polychlorotrifluoroethylene
PILs	Polyionic Ionic Liquids
PTFE	Polytetrafluoroethylene
pztc	Potential of Zero Total Charge
RE	Reference Electrode
RT	Room Temperature
RTILs	Room Temperature Ionic Liquids
SEM	Scanning Electron Microscopy
SFA	Surface Force Apparatus
SFM	Scanning Force Microscopy

Abbreviation	Meaning
SPM	Scanning Probe Microscopy
STM	Scanning Tunneling Microscopy
STS	Scanning Tunneling Spectroscopy
TSILs	Task-Specific Ionic Liquids
UHV	Ultrahigh Vacuum
UPD	Underpotential Deposition
UPS	Ultraviolet Photoelectron Spectroscopy
WE	Working Electrode
WKB	Wentzel-Kramers-Brillouin
XPS	X-Ray Photoelectron Spectroscopy
XRD	X-Ray Diffraction

Some Abbreviations for Ionic liquids, their Cations and Anions

Abbreviation	Meaning
$[BF_4]^-$	tetrafluoroborate
$[BMIm]^+$	1-butyl-3-methylimidazolium
$[BMIm]BF_4$	1-butyl-3-methylimidazolium tetrafluoroborate
[BMIm]Cl	1-butyl-3-methylimidazolium chloride
[BMIm]I	1-butyl-3-methylimidazolium iodide
$[BMIm]PF_6$	1-butyl-3-methylimidazolium hexafluorophoshate
[BMIm]TFSA	1-butyl-3-methylimidazolium bis(trifluoromethylsulfonyl)amide
BPCl	1-butylpyridinium chloride
DMEAF	dimethylethylammonium formate
EAF	ethylammonium formate
EAN	ethylammonium nitrate
$[EMIm]^+$	1-ethyl-3-methylimidazolium
$[EMIm]BF_4$	1-ethyl-3-methylimidazolium tetrafluoroborate
[EMIm]Br	1-ethyl-3-methylimidazolium bromide
[EMIm]Cl	1-ethyl-3-methylimidazolium chloride
[EMIm]DCA	1-ethyl-3-methylimidazolium dicyanamide
[EMIm]OAc	1-ethyl-3-methylimidazolium acetate
[EMIm]OMs	1-ethyl-3-methylimidazolium methylsulfonate
$[EMIm]PF_6$	1-ethyl-3-methylimidazolium hexafluorophosphate
[EMIm]TfO	1-ethyl-3-methylimidazolium trifluoromethylsulfonate
[EMIm]TFSA	1-ethyl-3-methylimidazolium bis(trifluoromethylsulfonyl)amide
$[EMMIm]^+$	1-ethyl-2,3-dimethylimidazolium
[EMMIm]TfO	1-ethyl-2,3-dimethylimidazolium trifluoromethylsulfonate

Abbreviation	Meaning
[EMMIm]TFSA	1-ethyl-2,3-dimethylimidazolium bis(trifluoromethylsulfonyl)amide
EPCl	1-ethylpyridinium chloride
EtAN	ethanolammonium nitrate
$[FAP]^-$	tris(pentafluoroethyl)trifluorophosphate
$[HMIm]^+$	1-hexyl-3-methylimidazolium
[HMIm]Cl	1-hexyl-3-methylimidazolium chloride
[HMIm]FAP	1-hexyl-3-methylimidazolium tris(pentafluoroethyl)trifluorophosphate
[HMIm]TFSA	1-hexyl-3-methylimidazolium bis(trifluoroethylsulfonyl)amide
$[MIm]^+$	1-methylimidazolium
[Mim]TfO	1-methylimidazolium trifluoromethylsulfonate
[MMIm]TFSA	1,3-dimethylimidazolium bis(trifluoroethylsulfonyl)amide
$[OAc]^-$	acetate
$[OMIm]^+$	1-octyl-3-methylimidazolium
$[OMs]^-$	methylsulfonate
[OMIm]TFSA	1-octyl-3-methylimidazolium bis(trifluoromethylsulfonyl)amide
PAN	propylammoniumnitrate
$[PF_6]^-$	hexafluorophosphate
$[PMIm]^+$	1-propyl-3-methylimidazolium
[PMPi]TFSA	N-propyl-N-methylpiperidinium bis(trifluoromethylsulfonyl)amide
$[Py_{1,4}]^+$	1-butyl-1-methylpyrrolidinium
$[Py_{1,4}]$DCA	1-butyl-1-methylpyrrolidinium dicyanamide
$[Py_{1,4}]$FSA	1-butyl-1-methylpyrrolidinium bis(fluorosufonyl)amide
$[Py_{1,4}]$FAP	1-butyl-1-methylpyrrolidinium tris(pentafluoroethyl)trifluorophosphate
$[Py_{1,4}]$TfO	1-butyl-1-methyl pyrrolidinium trifluoromethylsulfonate
$[Py_{1,4}]$TFSA	1-butyl-1-methylpyrrolidinium bis(trifluoromethylsulfonyl)amide
$[SbF_6]^-$	hexafluoroantimonate
$[TfO]^-$	trifluoromethanesulfonate
$[TFSA]^-$	bis(trifluoromethylsulfonyl)amide

11 Publications in the Framework of this Thesis

- R. Atkin, N. Borisenko, M. Drüschler, S. Zein El Abedin, F. Endres, R. Hayes, B. Huber, B. Roling, *„An in situ STM/AFM and impedance spectroscopy study of the extremely pure 1-butyl-1-methylpyrrolidinium tris(pentafluoroethyl)-trifluorophosphate/Au(111) interface: potential dependent solvation layers and the herringbone reconstruction*", Phys. Chem. Chem. Phys. 13(15) (2011) 6849-6857.
- N. Borisenko, S. Zein El Abedin, F. Endres, *„An in situ STM and DTS study of the extremely pure [EMIM]FAP/Au(111) interface*", ChemPhysChem, 13(7) (2012) 1736-1742.
- T. Carstens, R. Hayes, S. Zein El Abedin, B. Corr, G. B. Webber, N. Borisenko, R. Atkin, F. Endres, *„In situ STM, AFM and DTS study of the interface 1-hexyl-3-methylimidazolium tris(pentafluoroethyl)trifluorophosphate*", Electrochim. Acta 82(0) (2012) 48-59.
- R. Atkin, S. Zein El Abedin, R. Hayes, L. H. S Gasparotto, N. Borisenko, F. Endres, *„AFM and STM studies on the surface interaction of [BMP]TFSA and [EMIm]TFSA ionic liquids with Au(111)*", J. Phys. Chem. C, 113(30) (2009) 13266-13272.
- R. Hayes, N. Borisenko, M. K. Tam, P. C. Howlett, F. Endres, R. Atkin, *„Double layer structure of ionic liquids at the Au(111) electrode interface: an atomic force microscopy investigation*", J. Phys. Chem. C, 115(14) (2011) 6855-6863.
- T. Carstens, R. Gustus, O. Höfft, N. Borisenko, F. Endres, H. Li, R. J. Roos, A. J. Page, R. Atkin, *„Combined STM, AFM and DFT study of highly ordered pyrolytic graphite / 1-octyl-3-methylimidazolium bis(trifluoromethylsulfonyl)imide interface*", J. Phys. Chem. C 118(20) (2014) 10833-10843.
- N. Borisenko, R. Atkin, A. Lahiri, S. Zein El Abedin, F. Endres, *„Effect of dissolved LiCl on the ionic liquid/Au(111) interface: an in situ STM study*", 26(28) (2014) 284111-9.
- T. Carstens, A. Ispas, N. Borisenko, R. Atkin, A. Bund, F. Endres, *„In situ scanning tunneling microscopy (STM), atomic force microscopy (AFM) and quartz crystal microbalance (EQCM) studies of the electrochemical deposition of tantalum in two different ionic liquids with the 1-butyl-1-methylpyrrolidinium cation*", Electrochim. Acta, 197 (2016) 374-387.
- G. Pulletikurthi, A. Lahiri, T. Carstens, N. Borisenko, S. Zein El Abedin, F. Endres, *„Electrodeposition of silicon in three different ionic liquids: possible influence of the anion on the deposition process*", J. Solid State Electrochem., 17(11) (2013) 2823-2832.
- T. Carstens, A. Lahiri, N. Borisenko, F. Endres, *„[$Py_{1,4}$]FSI-NaFSI-based ionic liquid electrolyte for sodium batteries: Na^+ solvation and interfacial nanostructure on Au(111)*", J. Phys. Chem. C 120(27) (2016) 14736-14741.

- A. Lahiri, T. Carstens, R. Atkin, N. Borisenko, F. Endres, „*In situ atomic force microscopic studies of the interfacial multilayer nanostructure of LiTFSI-[$Py_{1,4}$]TFSI on Au(111): influence of Li^+ ion concentration on the Au(111)/IL interface*“, J. Phys. Chem. C 119(29) (2015) 16734-16742.
- T. Cui, A. Lahiri, T. Carstens, N. Borisenko, G. Pulletikurthi, C. Kuhl, F. Endres, „*Influence of water on the electrified ionic liquid/solid interface: a direct observation of the transition from a multilayered structure to a double-layer structure*“, 120(17) (2016) 9341-9349.
- V. Hoffmann, A. Lahiri, N. Borisenko, T. Carstens, G. Pulletikurthi, A. Borodin, R. Atkin, F. Endres, „*Nanostructure of the H-terminated p-Si(111)/ionic liquid interface and the effect of added lithium salt*“, Phys. Chem. Chem. Phys. 19(1) (2017) 54-58.
- N. Borisenko, A. Lahiri, G. Pulletikurthi, T. Cui, T. Carstens, J. Zahlbach, R. Atkin, F. Endres, „*The Au(111)/IL interfacial nanostructure in the presence of precursors and its influence on the electrodeposition process*“, Faraday Discuss. 206 (2017) 459-473.